eXPRESS Polymer Letters Vol.2, No.5 (2008) 312
Available online at www.expresspolymlett.com
DOI: 10.3144/expresspolymlett.2008.37

Editorial corner – a personal view

Water-mediated dispersion of 'nanofillers' in thermoplastics: Is it the right way?

J. Karger-Kocsis[*]

Institute for Composite Materials, University of Kaiserslautern, Erwin Schrödinger Str. 58, D-67663 Kaiserslautern, Germany

The extensive R&D work devoted to nanocomposites already resulted in new grades and products. Nevertheless, still great efforts are undertaken to improve the dispersion of 'old' and novel 'nanofillers' (layered silicates, carbon nanotubes /CNT/ and platelets). Though their interfacial modification is very helpful (and in some cases even a 'must') to achieve the desired dispersion, this is associated with some disadvantages. The type of the modification should be adjusted to the related polymer, which is usually rather costly. When preformed nanoparticles, like silica, TiO_2, CNT are incorporated, aspects of work health should be considered. This is necessary as the health hazards of long term exposure the human organism to such nanoparticles are not yet known. An elegant way to overcome the above problems is the dosage the nanoparticles in aqueous slurry, dispersion. CNTs can be exfoliated in aqueous media using suitable surfactants. Pristine clays are water swellable as their cations between the galleries become 'hydrated'. Several nanofillers, like synthetic boemite aluminas, are water dispersible. When introducing the corresponding slurry in the polymer melt during extrusion, nanocomposites can be produced. By suitable dosage of the 'nanofiller-source' slurry, screw configuration with venting possibilities (to evaporate the water carrier) and selecting the right polymers (less prone to hygrothermal degradation), nanocomposites with improved property profile can be achieved in a cost-efficient way. The fast evaporation of water ('blow-up' process) should support the fine dispersion of the fillers. There is a further promising option with this water-mediated technique. The toughness of the nanocomposites is usually lower than that of the matrix (note that this claim contradicts several reports, but likely this is the rule than the exception!). This is the reason why nanofillers are often used together with impact modifiers. It is noteworthy that the particle size of polymeric tougheners is in submicron range. But this is exactly the mean particle size of polymer latices, the dispersing medium of which is water. So, why not to produce nanomodified and toughened polymer systems at the same time, online in a suitable extruder?

The target morphology is a separate, fine and homogeneous dispersion of both latex and filler particles. There are many interesting possibilities when following this concept – however, you have to take care of the related patent literature. Good luck for your research!

Prof. Dr.-Ing. Dr. h.c. József Karger-Kocsis
Editor-in-chief

---

[*] Corresponding author, e-mail: karger@ivw.uni-kl.de

eXPRESS Polymer Letters Vol.2, No.5 (2008) 313–329
Available online at www.expresspolymlett.com
DOI: 10.3144/expresspolymlett.2008.38

Determination of χ from liquid-liquid phase data in ternary polymer systems (solvent/polymer/polymer) with hydrogen bonding

J. E. Figueruelo[1], *R. García-Lopera*[1*], *I. S. Monzó*[1], *C. Abad*[2], *A. Campos*[1]

[1]ICMUV, Departament de Química Física, Universitat de Valencia, 46100 Burjassot, Valencia, Spain
[2]Departament de Bioquímica i Biología Molecular, Universitat de Valencia, 46100 Burjassot, Valencia, Spain

Received 19 December 2007; accepted in revised form 23 February 2008

Abstract. Two different models accounting for the dependences of χ and *g* interaction parameters on both temperature and composition have been applied to different ternary polymer systems (TPS) solvent(1)/polymer(2)/polymer(3). The analyzed TPS have consisted on ten different polymer mixtures in chloroform as common solvent that can specifically interact via hydrogen bond. Experimental ternary phase diagrams determined by liquid chromatography were taken from literature. The application of the two models to the experimental data have served to obtain χ_{ij} and g_{ij} interaction parameters for all the binary *ij* (*ij* = 12, 13, 23) interactions established between the three components of the system, with simplified mathematical procedures. The results have shown a fair agreement between the calculated and the literature values, at least when the model containing an empirical entropy correction is used. Moreover, the evaluated interaction parameters follow the expected behaviour as the content of the H-donor polymer in the mixture is raised and are also in good accordance with experimental viscometric data.

Keywords: *modeling and simulation, interaction parameters, ternary polymer systems, hydrogen-bonding, rigid lattice theory*

---

1. Introduction

An increasing interest in solving complex systems, such as polyblends [1], nanoparticles, composites or ternary polymer systems (TPS) formed by a mixture of three polymers, through the thermodynamic analysis of phase diagrams is clearly evidenced. For example, the curing of an epoxy in the presence of thermoplastics and additives is usually followed by the evolution of their phase diagrams as the curing process goes on. The classical procedure consists on writing the Gibbs free energy function of mixture and obtaining the corresponding chemical potentials, Δμ, in each phase. Generally, the equations obtained for this kind of systems show a great complexity, and, in consequence, the values of the χ interaction parameters are usually unknown or rarely known with any certainty. To circumvent this drawback, different approximations have to be introduced in order to simplify the mathematical solution.

It is now generally accepted that in order to obtain quantitative agreement between Flory-Huggins theory and experimental observations for most polymer systems, χ interaction parameter dependence on both temperature and composition must be considered [2–4]. Sometimes the *g* interaction parameter (mathematically related to χ) can be expressed as a more complex function than 1/*T* [5]. Other *g*(*T*, composition) functions can be theoretically derived in the framework of the rigid lattice model, as Staverman [6] and Koningsveld and Kleitjens [7], among others, have demonstrated. Nowadays it is

---

[*]Corresponding author, e-mail: rosa.garcia@uv.es

accepted that the dependence of g on concentration mainly arises from the disparities in size and shape of the solvent molecules and the polymer segments. According to Staverman [6], it is possible to write the functionality of g as Equation (1):

$$g = \frac{D(T)}{1 - c\phi_2} \tag{1}$$

where c is a constant determined from Bondi studies [8–10] and $D(T)$ accounts for the temperature dependence in the form of Equation (2):

$$D(T) = a + \frac{b}{T} \tag{2}$$

On the other hand, $\chi \rightarrow g$, just when the volume fraction of component 2 $\phi_2 \rightarrow 1$, or at infinite dilution of solvent, which are the conditions fulfilled by the inverse gas chromatography technique [5], although, it is also used (Equation (3)) when analyzing the thermodynamics of the phase separation during polymerization of a thermoset system into a thermoplastic matrix [11, 12].

$$\chi = \frac{D(T)}{1 - c\phi_2} \tag{3}$$

Occasionally, and in order to adjust the experimental results, the interaction function, dependent on both temperature and composition, can be written [5, 13–15] as Equation (4):

$$g = \alpha + \frac{D(T)}{1 - \phi_2} \tag{4}$$

where α is an empirical entropy correction [5] given by Equation (5):

$$\alpha = \alpha_S + \frac{\alpha_H}{T} \tag{5}$$

Obviously, this new g value yields a different expression for χ, (Equation (6)) [15]:

$$\chi = \alpha + \frac{D(1 - c)}{(1 - c\phi_2)^2} \tag{6}$$

Moreover, an even more complex function to express the χ temperature and concentration dependence has been found (Equation (7)) [16]:

$$\chi(T, \phi_2) = (1 + c_1\phi_2 + c_2\phi_2^2)(D + d \ln T) \tag{7}$$

where c_i ($i = 1, 2$), D and d being adjustable parameters.

Usually, the use of any of the above expressions simplifies the χ evaluation, although unfortunately, the calculated values cannot be experimentally checked, especially in complex systems. Fortunately, there are more traditional and simple systems with well-known values of the interaction parameters that can be used to judge the validity of the approximations used in the more complex and actual systems. In this regard, in recent papers, dealing with compatibility between polystyrene copolymers and other polymers in solution via hydrogen bonding [17–19], the phase diagrams of the ternary polymer systems (TPS) have been obtained from experimental liquid chromatography data [20–22]. The achievement of χ values from liquid-liquid phase data has been considered a reliable method [16] and consists in solving the equations obtained by equating the chemical potentials in both phases in equilibrium, for all the components. To mathematically solve the equations, two of the most often used models for $\chi(T, \phi_2)$ have been applied. The validity of the theoretical results has been judged in the light of the experimental ones, measured by viscometry and liquid chromatography [18–20]. Moreover, the adequacy and reliability of the diverse χ models has also been tested from a basic thermodynamic viewpoint.

2. Theory

2.1. Chemical potentials and interaction parameters

In ternary solvent(1)/polymer(2)/polymer(3) systems with polydisperse polymers, the Gibbs free energy change upon mixing n_i mols of component i ($i = 1, 2, 3$) is given by Equation (8):

$$\frac{\Delta G^M}{RT} = n_1 \ln \phi_1 + \sum_{n=1,m_2}^{m_2} n_{2,x_n} \ln \phi_{2,x_n} + \sum_{n=1,m_3}^{m_3} n_{3,x_n} \ln \phi_{3,x_n} + n_1\phi_2 g_{12} + n_1\phi_3 g_{13} \tag{8}$$

whereas for monodisperse polymers (or with low polydispersity index) is given by Equation (9):

$$\frac{\Delta G^M}{RT} = n_1 \ln\phi_1 + n_2 \ln\phi_2 + n_3 \ln\phi_3 + n_1\phi_2 g_{12} + n_1\phi_3 g_{13} + \bar{x}_2 n_2 \phi_3 g_{23} \tag{9}$$

and the chemical potentials deduced from Equation (9) are then given by Equations (10) and (11):

$$\begin{aligned}\frac{\Delta\mu_1}{RT} = \frac{1}{RT}\left(\frac{\partial \Delta G^M}{\partial n_1}\right)_{n_2,n_3,p,T} &= \ln\phi_1 + \left(1-\frac{V_1}{V_2}\right)\phi_2 + \left(1-\frac{V_1}{V_3}\right)\phi_3 + \left[g_{12} - \frac{\phi_1\phi_2}{1-\phi_1}\frac{\mathrm{d}g_{12}}{\mathrm{d}\phi_2}\right]\phi_2(1-\phi_1) + \\ &\left[g_{13} - \frac{\phi_1\phi_3}{1-\phi_1}\frac{\mathrm{d}g_{13}}{\mathrm{d}\phi_3}\right]\phi_3(1-\phi_1) - \left[g_{23} + \phi_3\frac{\mathrm{d}g_{23}}{\mathrm{d}\phi_3}\right]\phi_2\phi_3\frac{V_1}{V_2} = \\ &\ln\phi_1 + \left(1-\frac{V_1}{V_2}\right)\phi_2 + \left(1-\frac{V_1}{V_3}\right)\phi_3 + \chi_{12}\phi_2(1-\phi_1) + \chi_{13}\phi_3(1-\phi_1) - \varepsilon_{23}\phi_2\phi_3\frac{V_1}{V_2}\end{aligned} \tag{10}$$

$$\begin{aligned}\frac{\Delta\mu_2}{RT} = \frac{1}{RT}\left(\frac{\partial \Delta G^M}{\partial n_2}\right)_{n_1,n_3,p,T} &= \ln\phi_2 + \left(1-\frac{V_2}{V_1}\right)\phi_1 + \left(1-\frac{V_2}{V_3}\right)\phi_3 + \left[g_{12} + \phi_2\frac{\mathrm{d}g_{12}}{\mathrm{d}\phi_2}\right]\phi_1(1-\phi_2)\frac{V_2}{V_1} - \\ &\left[g_{13} + \phi_3\frac{\mathrm{d}g_{13}}{\mathrm{d}\phi_3}\right]\phi_1\phi_3\frac{V_2}{V_1} + \left[g_{23} - \frac{\phi_2\phi_3}{1-\phi_2}\frac{\mathrm{d}g_{23}}{\mathrm{d}\phi_3}\right]\phi_3(1-\phi_2)\frac{V_2}{V_1} = \\ &\ln\phi_2 + \left(1-\frac{V_2}{V_1}\right)\phi_1 + \left(1-\frac{V_2}{V_3}\right)\phi_3 + \varepsilon_{12}\phi_1(1-\phi_2)\frac{V_2}{V_1} - \varepsilon_{13}\phi_1\phi_3\frac{V_2}{V_1} + \chi_{23}\phi_3(1-\phi_2)\frac{V_2}{V_1}\end{aligned} \tag{11}$$

and by Equation (12):

$$\begin{aligned}\frac{\Delta\mu_3}{RT} = \frac{1}{RT}\left(\frac{\partial \Delta G^M}{\partial n_3}\right)_{n_1,n_2,p,T} &= \ln\phi_3 + \left(1-\frac{V_3}{V_1}\right)\phi_1 + \left(1-\frac{V_3}{V_2}\right)\phi_2 - \left[g_{12} + \phi_2\frac{\mathrm{d}g_{12}}{\mathrm{d}\phi_2}\right]\phi_1\phi_2\frac{V_3}{V_1} + \\ &\left[g_{13} + \phi_3\frac{\mathrm{d}g_{13}}{\mathrm{d}\phi_3}\right]\phi_1(1-\phi_3)\frac{V_3}{V_1} + \left[g_{23} + \phi_3\frac{\mathrm{d}g_{23}}{\mathrm{d}\phi_3}\right]\phi_2(1-\phi_3)\frac{V_3}{V_1} = \\ &\ln\phi_3 + \left(1-\frac{V_3}{V_1}\right)\phi_1 + \left(1-\frac{V_3}{V_2}\right)\phi_2 - \varepsilon_{12}\phi_1\phi_2\frac{V_3}{V_1} + \varepsilon_{13}\phi_1(1-\phi_3)\frac{V_3}{V_1} + \varepsilon_{23}\phi_2(1-\phi_3)\frac{V_3}{V_1}\end{aligned} \tag{12}$$

where n_i, V_i and $\Delta\mu_i$ (i = 1, 2, 3) are mol numbers, molar volumes and chemical potentials, respectively. In Equations (10)–(12) the residual contributions to $\Delta\mu_i$ (the terms containing g_{12}, g_{13} and g_{23}) are ternary volume fractions ϕ_i (i = 1, 2, 3) functions representative of binary interaction parameters. Generally, two types of ternary functions can be considered, those of the form given in Equation (13):

$$\left[g_{ij} - \frac{\phi_i\phi_j}{1-\phi_i}\frac{\mathrm{d}g_{ij}}{\mathrm{d}\phi_j}\right] \tag{13}$$

where ij represents the 1-2, 1-3 and 2-3 interactions, which are also called χ_{ij} because when they are transformed into binary functions (concretely, χ_{13}^{binary} is deduced from $\chi_{13}^{ternary}$ by making $\phi_2 = 0$), the classical Flory's interaction parameters are obtained, which are defined in $\Delta\mu_i^{binary}$ by Equation (14) [15]:

$$\chi_{ij} = g_{ij} - \phi_i\frac{\mathrm{d}g_{ij}}{\mathrm{d}\phi_j} = g_{ij} + \phi_i\frac{\mathrm{d}g_{ij}}{\mathrm{d}\phi_i} \tag{14}$$

The other functions types adopt the following functionality shown by Equation (15):

$$g_{ij}+\phi_j\frac{\mathrm{d}g_{ij}}{\mathrm{d}\phi_j} \tag{15}$$

also named ε_{ij}, because when they are transformed into binary functions, the parameters defining $\Delta\mu_i^{binary}$ are obtained by Equation (16) [15, 23]:

$$\varepsilon_{ij}=g_{ij}+\phi_j\frac{\mathrm{d}g_{ij}}{\mathrm{d}\phi_j}=g_{ij}-\phi_j\frac{\mathrm{d}g_{ij}}{\mathrm{d}\phi_i} \tag{16}$$

The interconversion between χ_{ij} and ε_{ij} for binary polymer systems (BPS) is achieved at constant temperature [24] through different dependences on component j concentration, χ_{13}^{binary} expressed as volume fraction ϕ_j by Equations (17)–(20):

$$\chi_{ij}=\chi_{ij}^{(0)}+\chi_{ij}^{(1)}\phi_j+\ldots=\sum_{n=0}^{m}\chi^{(n)}\phi_j^n \tag{17}$$

$$\chi_{ij}=g_{ij}-\phi_i\frac{\mathrm{d}g_{ij}}{\mathrm{d}\phi_j}=g_{ij}-(1-\phi j)\frac{\mathrm{d}g_{ij}}{\mathrm{d}\phi_j} \tag{18}$$

$$\chi_{ij}=-d[(1-\phi_j)g_{ij}] \tag{19}$$

$$g_{ij}=\frac{1}{1-\phi_j}\int_{\phi_j}^{1}\chi_{ij}\mathrm{d}\phi_j \tag{20}$$

Finally, the substitution of Equation (20) into Equation (17) yields Equation (21):

$$g_{ij}=\left(\chi_{ij}^{(0)}+\frac{\chi_{ij}^{(1)}}{2}+\ldots\right)+\left(\frac{\chi_{ij}^{(1)}}{2}+\frac{\chi_{ij}^{(2)}}{3}\right)\phi_j+\ldots= \sum_{n=0}^{m}\frac{\chi^{(n)}}{n+1}\frac{1-\phi_j^{(n+1)}}{1-\phi_j} \tag{21}$$

which allows to evaluate g_{ij} parameters from experimental χ_{ij} values.

2.2. Models for interaction parameters dependences on concentration and temperature in BPS

2.2.1. Model a1

In the literature is possible to find g_{ij} values as a function of temperature and composition according to Equation (22) [5, 15]:

$$g_{ij}=\alpha_{ij}+\frac{D_{ij}}{1-c_{ij}\phi_j} \tag{22}$$

where α_{ij} and c_{ij} are constants for a given system and temperature interval, and $D_{ij}(T)$ (Equation (2)), being a and b parameters with entropic and enthalpic character, respectively [4]. According to Equation (18), the corresponding χ_{ij} values are given by Equation (23):

$$\chi_{ij}=\alpha_{ij}+\frac{D_{ij}(1-c_{ij})}{(1-c_{ij}\phi_j)^2} \tag{23}$$

and according to Equation (16) the corresponding ε_{ij} should be as given by Equation (24):

$$\varepsilon_{ij}=\alpha_{ij}+\frac{D_{ij}}{(1-c_{ij}\phi_j)^2} \tag{24}$$

There are other models describing the g dependences with temperature and composition for binary polymer systems. In general it is accepted that the main reason for the g dependence on concentration arises from the disparity in size and shape between the solvent molecules and the polymer segments. Therefore, and according to Staverman [6], the g function can be written as given by Equation (25):

$$g_{ij}=\frac{D_{ij}}{1-c_{ij}\phi_j} \tag{25}$$

with D_{ij} and c_{ij} as previously defined. However, when this set of equations is applied to the experimental results, is necessary to introduce a new fitting empirical parameter, α_{ij}. At high ϕ_j values, calculated and measured binodals, spinodals and χ_{ij} vs. ϕ_j curves show that the empirical α_{ij} parameter depends on temperature (Equation (26)):

$$\alpha_{ij}=m+nT \tag{26}$$

where the parameter n may assume any sign and the relation can only describe the behaviour within a rather limited range of temperatures. As a consequence, it is arrived again at the Equation (22) with α_{ij} dependence with T.

2.2.2. Model a2

Other models allow to express the g_{ij} interaction parameters in BPS by using a less number of fitting parameters, according to Equation (27):

$$g_{ij} = \frac{D_{ij}}{c_{ij}(1-\phi_j)}\ln(1-c_{ij}\phi_j) \tag{27}$$

with D_{ij} and c_{ij} as defined in Equation (22). Now, the χ_{ij} values attained are given by Equation (28):

$$\chi_{ij} = \frac{D_{ij}}{1-c_{ij}\phi_j} \tag{28}$$

This expression has been recently used to thermodynamically analyze the phase separation occurring during the polymerization of a thermoset epoxy system into a thermoplastic matrix [11, 12, 25]. According to this model and taking into account Equation (27) the following ε_{ij} value is obtained as shown by Equation (29):

$$\varepsilon_{ij} = \frac{D_{ij}}{c_{ij}}\ln(1-c_{ij}\phi_j)\frac{\phi_i+\phi_j}{\phi_i^2} - \frac{\phi_j}{\phi_i}\frac{D_{ij}}{1-c_{ij}\phi_j} \tag{29}$$

as well as by Equation (30):

$$\phi_i^2\varepsilon_{ij} = \frac{D_{ij}}{c_{ij}}\ln(1-c_{ij}\phi_j) - \phi_i\phi_j\frac{D_{ij}}{1-c_{ij}\phi_j} = \int_{\phi_j}^{1}\chi_{ij}\mathrm{d}\phi_j - \phi_i\phi_j\chi_{ij} \tag{30}$$

which relates ε_{ij} and χ_{ij} in binary polymeric systems [11, 12, 25].

2.3. Models for interaction parameters dependences on concentration and temperature in TPS

The g_{ij} values derived with the different models for BPS have no reasons to change when ternary solvent/polymer/polymer systems are considered. In fact, in the Gibbs free energy of mixing, g_{ij} represents the energy interchanged by one contact *i-j* (1-2, 1-3 and 2-3) independently of the presence of a third component (see Equation (8)). To prove this fact, next the corresponding expressions for the 1-2 interaction, as an example, will be derived.

2.3.1. Model b1

First of all and recalling the **a1** model, the following expressions shown by Equations (31)–(34) hold in BPS:

$$g_{12} = \alpha_{12} + \frac{D_{12}}{1-c_{12}\phi_2} \tag{31}$$

$$\frac{\mathrm{d}g_{12}}{\mathrm{d}\phi_2} = \frac{c_{12}D_{12}}{(1-c_{12}\phi_2)^2} \tag{32}$$

$$\chi_{12} = g_{12} - \phi_1\frac{\mathrm{d}g_{12}}{\mathrm{d}\phi_2} = \alpha_{12} + \frac{D_{12}(1-c_{12})}{(1-c_{12}\phi_2)^2} \tag{33}$$

$$\varepsilon_{12} = g_{12} + \phi_2\frac{\mathrm{d}g_{12}}{\mathrm{d}\phi_2} = \alpha_{12} + \frac{D_{12}}{(1-c_{12}\phi_2)^2} \tag{34}$$

whereas for a TPS and recalling Equations (13), (31) and (32), Equation (33) yields Equation (35):

$$\chi_{12} = g_{12} - \frac{\phi_1\phi_2}{1-\phi_1}\frac{\mathrm{d}g_{12}}{\mathrm{d}\phi_2} \tag{35}$$

or Equation (36):

$$\chi_{12} = \alpha_{12} + \frac{D_{12}(1-\phi_1-c_{12}\phi_2)}{(1-\phi_1)(1-c_{12}\phi_2)^2} \tag{36}$$

On the other hand, from Equations (16), (31) and (32) Equation (37) can be obtained:

$$\varepsilon_{12} = g_{12} + \phi_2\frac{dg_{12}}{d\phi_2} = \alpha_{12} + \frac{D_{12}}{(1-c_{12}\phi_2)^2} \tag{37}$$

which is the same expression as Equation (34) since ε is identical both in BPS and in TPS, although by using their respective binary and ternary volume fractions, ϕ, in the corresponding calculations.

In TPS with two phases (α and β) present in equilibrium the following conditions, given by Equation (38) hold:

$$\begin{aligned}\Delta\mu_1^\alpha &= \Delta\mu_1^\beta\\ \Delta\mu_2^\alpha &= \Delta\mu_2^\beta\\ \Delta\mu_3^\alpha &= \Delta\mu_3^\beta\end{aligned} \tag{38}$$

that applied to the present model leads to Equations (39)–(41):

$$\ln\phi_1^\alpha+\left(1-\frac{V_1}{V_2}\right)\phi_2^\alpha+\left(1-\frac{V_1}{V_3}\right)\phi_3^\alpha+\left[\alpha_{12}+\frac{D_{12}(1-\phi_1^\alpha-c_{12}\phi_2^\alpha)}{(1-\phi_1^\alpha)(1-c_{12}\phi_2^\alpha)^2}\right]\phi_2^\alpha(1-\phi_1^\alpha)+$$
$$\left[\alpha_{13}+\frac{D_{13}(1-\phi_1^\alpha-c_{13}\phi_3^\alpha)}{(1-\phi_1^\alpha)(1-c_{13}\phi_3^\alpha)^2}\right]\phi_3^\alpha(1-\phi_1^\alpha)-\left[\alpha_{23}+\frac{D_{23}}{(1-c_{23}\phi_3^\alpha)^2}\right]\frac{V_1}{V_2}\phi_2^\alpha\phi_3^\alpha=$$
$$\ln\phi_1^\beta+\left(1-\frac{V_1}{V_2}\right)\phi_2^\beta+\left(1-\frac{V_1}{V_3}\right)\phi_3^\beta+\left[\alpha_{12}+\frac{D_{12}(1-\phi_1^\beta-c_{12}\phi_2^\beta)}{(1-\phi_1^\alpha)(1-c_{12}\phi_2^\beta)^2}\right]\phi_2^\beta(1-\phi_1^\beta)+$$
$$\left[\alpha_{13}+\frac{D_{13}(1-\phi_1^\beta-c_{13}\phi_3^\beta)}{(1-\phi_1^\beta)(1-c_{13}\phi_3^\beta)^2}\right]\phi_3^\beta(1-\phi_1^\beta)-\left[\alpha_{23}+\frac{D_{23}}{(1-c_{23}\phi_3^\beta)^2}\right]\frac{V_1}{V_2}\phi_2^\beta\phi_3^\beta \tag{39}$$

$$\ln\phi_2^\alpha+\left(1-\frac{V_2}{V_1}\right)\phi_1^\alpha+\left(1-\frac{V_2}{V_3}\right)\phi_3^\alpha+\left[\alpha_{12}+\frac{D_{12}}{(1-c_{12}\phi_2^\alpha)^2}\right]\phi_1^\alpha(1-\phi_2^\alpha)\frac{V_2}{V_1}-$$
$$\left[\alpha_{13}+\frac{D_{13}}{(1-c_{13}\phi_3^\alpha)^2}\right]\phi_1^\alpha\phi_3^\alpha\frac{V_2}{V_1}+\left[\alpha_{23}+\frac{D_{23}(1-\phi_2^\alpha-c_{23}\phi_3^\alpha)}{(1-\phi_2^\alpha)(1-c_{23}\phi_3^\alpha)^2}\right]\phi_3^\alpha(1-\phi_2^\alpha)\frac{V_2}{V_1}=$$
$$\ln\phi_2^\beta+\left(1-\frac{V_2}{V_1}\right)\phi_1^\beta+\left(1-\frac{V_2}{V_3}\right)\phi_3^\beta+\left[\alpha_{12}+\frac{D_{12}}{(1-c_{12}\phi_2^\beta)^2}\right]\phi_1^\beta(1-\phi_2^\beta)\frac{V_2}{V_1}-$$
$$\left[\alpha_{13}+\frac{D_{13}}{(1-c_{13}\phi_3^\beta)^2}\right]\phi_1^\beta\phi_3^\beta\frac{V_2}{V_1}+\left[\alpha_{23}+\frac{D_{23}(1-\phi_2^\beta-c_{23}\phi_3^\beta)}{(1-\phi_2^\beta)(1-c_{23}\phi_3^\beta)^2}\right]\phi_3^\beta(1-\phi_2^\beta)\frac{V_2}{V_1} \tag{40}$$

$$\ln\phi_3^\alpha+\left(1-\frac{V_3}{V_1}\right)\phi_1^\alpha+\left(1-\frac{V_3}{V_2}\right)\phi_2^\alpha-\left[\alpha_{12}+\frac{D_{12}}{(1-c_{12}\phi_2^\alpha)^2}\right]\phi_1^\alpha\phi_2^\alpha\frac{V_3}{V_1}+$$
$$\left[\alpha_{13}+\frac{D_{13}}{(1-c_{13}\phi_3^\alpha)^2}\right]\phi_1^\alpha(1-\phi_3^\alpha)\frac{V_3}{V_1}+\left[\alpha_{23}+\frac{D_{23}}{(1-c_{23}\phi_3^\alpha)^2}\right]\phi_2^\alpha(1-\phi_3^\alpha)\frac{V_3}{V_1}=$$
$$\ln\phi_3^\beta+\left(1-\frac{V_3}{V_1}\right)\phi_1^\beta+\left(1-\frac{V_3}{V_2}\right)\phi_2^\beta-\left[\alpha_{12}+\frac{D_{12}}{(1-c_{12}\phi_2^\beta)^2}\right]\phi_1^\beta\phi_2^\beta\frac{V_3}{V_1}+$$
$$\left[\alpha_{13}+\frac{D_{13}}{(1-c_{13}\phi_3^\beta)^2}\right]\phi_1^\beta(1-\phi_3^\beta)\frac{V_3}{V_1}+\left[\alpha_{23}+\frac{D_{23}}{(1-c_{23}\phi_3^\beta)^2}\right]\phi_2^\beta(1-\phi_3^\beta)\frac{V_3}{V_1} \tag{41}$$

The terms in brackets are the corresponding χ_{ij} and ε_{ij} values (ij = 12, 13, 23) in phases α or β, according to the **b1** model, that is, taking into account Equations (36) and (37).

2.3.2 Model b2

Similarly and according to the **a2** model, in PBS the generic Equations (27)–(29) should read for the 1-2 interaction as shown by Equations (42)–(44):

$$g_{12}=\frac{D_{12}}{c_{12}(1-\phi_2)}\ln(1-c_{12}\phi_2) \tag{42}$$ R1

$$\chi_{12}=\frac{D_{12}}{1-c_{12}\phi_2} \tag{43}$$ R2

$$\varepsilon_{12}=\frac{D_{12}\ln(1-\phi_2)}{c_{12}}\frac{\phi_1\phi_2}{\phi_1^2}-\frac{\phi_2}{\phi_1}\frac{D_{12}}{1-c_{12}\phi_2} \tag{44}$$ R3

whereas for a TPS yields Equation (45):

$$\chi_{12} = g_{12} - \frac{\phi_1\phi_2}{1-\phi_1}\frac{dg_{12}}{d\phi_2} = \frac{D_{12}}{c_{12}}\frac{\ln(1-\phi_2)}{1-\phi_2}\left\{1-\frac{\phi_1\phi_2}{(1-\phi_1)(1-\phi_2)}\right\}+\frac{D_{12}}{1-c_{12}\phi_2}\frac{\phi_1\phi_2}{(1-\phi_1)(1-\phi_2)} \tag{45}$$

and Equation (46):

$$\varepsilon_{12} = g_{12} + \phi_2\frac{dg_{12}}{d\phi_2} = \frac{D_{12}}{c_{12}}\frac{\ln(1-c_{12}\phi_2)}{(1-\phi_2)^2} - \frac{\phi_2 D_{12}}{(1-\phi_2)(1-c_{12}\phi_2)} \tag{46}$$

It is easy to prove that Equation (45) transforms into Equation (43) for BPS when $\phi_3 = 0$ and $\phi_1\phi_2/[(1-\phi_1)(1-\phi_2)] = 1$; and Equation (46) into Equation (29) if $\phi_3 = 0$.

Finally, the substitution of χ_{12} and ε_{12} values derived with the **b2** model into Equations (10)–(12) when equilibrium condition holds (Equation (38)), yields for each component of the TPS Equations (47) and (48):

$$\begin{aligned}
&\ln\phi_1^\alpha + \left(1-\frac{V_1}{V_2}\right)\phi_2^\alpha + \left(1-\frac{V_1}{V_3}\right)\phi_3^\alpha + \\
&\left[\frac{D_{12}}{c_{12}} + \frac{\ln(1-\phi_2^\alpha)}{1-\phi_2^\alpha}\left\{1-\frac{\phi_1^\alpha\phi_2^\alpha}{(1-\phi_1^\alpha)(1-\phi_2^\alpha)}\right\} + \frac{\phi_1^\alpha\phi_2^\alpha}{(1-\phi_1^\alpha)(1-\phi_2^\alpha)}\frac{D_{12}}{1-c_{12}\phi_2^\alpha}\right]\phi_2^\alpha(1-\phi_1^\alpha) + \\
&\left[\frac{D_{13}}{c_{13}} + \frac{\ln(1-\phi_3^\alpha)}{1-\phi_3^\alpha}\left\{1-\frac{\phi_1^\alpha\phi_3^\alpha}{(1-\phi_1^\alpha)(1-\phi_3^\alpha)}\right\} + \frac{\phi_1^\alpha\phi_3^\alpha}{(1-\phi_1^\alpha)(1-\phi_3^\alpha)}\frac{D_{13}}{1-c_{13}\phi_3^\alpha}\right]\phi_3^\alpha(1-\phi_3^\alpha) - \\
&D_{13}\left[\frac{\ln(1-c_{23}\phi_3^\alpha)}{c_{23}(1-\phi_3^\alpha)^2} - \frac{\phi_3^\alpha}{(1-\phi_3^\alpha)(1-c_{23}\phi_3^\alpha)}\right]\frac{V_1}{V_2}\phi_2^\alpha\phi_3^\alpha = \\
&\ln\phi_1^\beta + \left(1-\frac{V_1}{V_2}\right)\phi_2^\beta + \left(1-\frac{V_1}{V_3}\right)\phi_3^\beta + \\
&\left[\frac{D_{12}}{c_{12}} + \frac{\ln(1-\phi_2^\beta)}{1-\phi_2^\beta}\left\{1-\frac{\phi_1^\beta\phi_2^\beta}{(1-\phi_1^\beta)(1-\phi_2^\beta)}\right\} + \frac{\phi_1^\beta\phi_2^\beta}{(1-\phi_1^\beta)(1-\phi_2^\beta)}\frac{D_{12}}{1-c_{12}\phi_2^\beta}\right]\phi_2^\beta(1-\phi_1^\beta) + \\
&\left[\frac{D_{13}}{c_{13}} + \frac{\ln(1-\phi_3^\beta)}{1-\phi_3^\beta}\left\{1-\frac{\phi_1^\beta\phi_3^\beta}{(1-\phi_1^\beta)(1-\phi_3^\beta)}\right\} + \frac{\phi_1^\beta\phi_3^\beta}{(1-\phi_1^\beta)(1-\phi_3^\beta)}\frac{D_{13}}{1-c_{13}\phi_3^\beta}\right]\phi_3^\beta(1-\phi_3^\beta) - \\
&D_{23}\left[\frac{\ln(1-c_{23}\phi_3^\beta)}{c_{23}(1-\phi_3^\beta)^2} - \frac{\phi_3^\beta}{(1-\phi_3^\beta)(1-c_{23}\phi_3^\alpha)}\right]\frac{V_1}{V_2}\phi_2^\beta\phi_3^\beta
\end{aligned} \tag{47}$$

$$\begin{aligned}
&\ln\phi_2^\alpha + \left(1-\frac{V_2}{V_1}\right)\phi_1^\alpha + \left(1-\frac{V_2}{V_3}\right)\phi_3^\alpha + \\
&D_{12}\left[\frac{\ln(1-c_{12}\phi_2^\alpha)}{c_{12}(1-\phi_2^\alpha)^2} - \frac{\phi_2^\alpha}{(1-\phi_2^\alpha)(1-c_{12}\phi_2^\alpha)}\right]\phi_1^\alpha(1-\phi_2^\alpha)\frac{V_2}{V_1} - D_{13}\left[\frac{\ln(1-c_{13}\phi_3^\alpha)}{c_{13}(1-\phi_3^\alpha)^2} - \frac{\phi_3^\alpha}{(1-\phi_3^\alpha)(1-c_{13}\phi_3^\alpha)}\right]\phi_1^\alpha\phi_3^\alpha\frac{V_2}{V_1} + \\
&\left[\frac{D_{23}}{c_{23}}\frac{\ln(1-\phi_3^\alpha)}{1-\phi_3^\alpha}\left\{1-\frac{\phi_2^\alpha\phi_3^\alpha}{(1-\phi_2^\alpha)(1-\phi_3^\alpha)}\right\} + \frac{\phi_2^\alpha\phi_3^\alpha D_{23}}{(1-\phi_2^\alpha)(1-\phi_3^\alpha)(1-c_{13}\phi_3^\alpha)}\right]\phi_3^\alpha(1-\phi_2^\alpha)\frac{V_2}{V_1} = \\
&\ln\phi_2^\beta + \left(1-\frac{V_2}{V_1}\right)\phi_1^\beta + \left(1-\frac{V_2}{V_3}\right)\phi_3^\beta + \\
&D_{12}\left[\frac{\ln(1-c_{12}\phi_2^\beta)}{c_{12}(1-\phi_2^\beta)^2} - \frac{\phi_2^\beta}{(1-\phi_2^\beta)(1-c_{12}\phi_2^\beta)}\right]\phi_1^\beta(1-\phi_2^\beta)\frac{V_2}{V_1} - D_{13}\left[\frac{\ln(1-c_{13}\phi_3^\beta)}{c_{13}(1-\phi_3^\beta)^2} - \frac{\phi_3^\beta}{(1-\phi_3^\beta)(1-c_{13}\phi_3^\beta)}\right]\phi_1^\beta\phi_3^\beta\frac{V_2}{V_1} + \\
&\left[\frac{D_{23}}{c_{23}}\frac{\ln(1-\phi_3^\beta)}{1-\phi_3^\beta}\left\{1-\frac{\phi_2^\beta\phi_3^\beta}{(1-\phi_2^\beta)(1-\phi_3^\beta)}\right\} + \frac{\phi_2^\beta\phi_3^\beta D_{23}}{(1-\phi_2^\beta)(1-\phi_3^\beta)(1-c_{13}\phi_3^\beta)}\right]\phi_3^\beta(1-\phi_2^\beta)\frac{V_2}{V_1}
\end{aligned} \tag{48}$$

and Equation (49):

$$\begin{aligned}
&\ln\phi_3^\alpha + \left(1-\frac{V_3}{V_1}\right)\phi_1^\alpha + \left(1-\frac{V_3}{V_2}\right)\phi_2^\alpha - D_{12}\left[\frac{\ln(1-c_{12}\phi_2^\alpha)}{c_{12}(1-\phi_2^\alpha)^2} - \frac{\phi_2^\alpha}{(1-\phi_2^\alpha)(1-c_{12}\phi_2^\alpha)}\right]\phi_1^\alpha\phi_2^\alpha\frac{V_3}{V_1} + \\
&D_{13}\left[\frac{\ln(1-c_{13}\phi_3^\alpha)}{c_{13}(1-\phi_3^\alpha)^2} - \frac{\phi_3^\alpha}{(1-\phi_3^\alpha)(1-c_{13}\phi_3^\alpha)}\right]\phi_1^\alpha(1-\phi_3^\alpha)\frac{V_3}{V_1} + D_{23}\left[\frac{\ln(1-c_{23}\phi_3^\alpha)}{c_{23}(1-\phi_3^\alpha)^2} - \frac{\phi_3^\alpha}{(1-\phi_3^\alpha)(1-c_{23}\phi_3^\alpha}\right]\phi_2^\alpha(1-\phi_3^\alpha)\frac{V_3}{V_1} = \\
&\ln\phi_3^\beta + \left(1-\frac{V_3}{V_1}\right)\phi_1^\beta + \left(1-\frac{V_3}{V_2}\right)\phi_2^\beta - D_{12}\left[\frac{\ln(1-c_{12}\phi_2^\beta)}{c_{12}(1-\phi_2^\beta)^2} - \frac{\phi_2^\beta}{(1-\phi_2^\beta)(1-c_{12}\phi_2^\beta)}\right]\phi_1^\beta\phi_2^\beta\frac{V_3}{V_1} + \\
&D_{13}\left[\frac{\ln(1-c_{13}\phi_3^\beta)}{c_{13}(1-\phi_3^\beta)^2} - \frac{\phi_3^\beta}{(1-\phi_3^\beta)(1-c_{13}\phi_3^\beta)}\right]\phi_1^\beta(1-\phi_3^\beta)\frac{V_3}{V_1} + D_{23}\left[\frac{\ln(1-c_{23}\phi_3^\beta)}{c_{23}(1-\phi_3^\beta)^2} - \frac{\phi_3^\beta}{(1-\phi_3^\beta)(1-c_{23}\phi_3^\beta}\right]\phi_2^\beta(1-\phi_3^\beta)\frac{V_3}{V_1}
\end{aligned} \tag{49}$$

Again, the terms in brackets correspond to the χ_{ij} and ε_{ij} (ij = 12, 13, 23) interaction parameters in phases α or β derived with **b2** model.

It is interesting to note that both **b1** (Equation (39) or (40)) and **b2** (Equation (47) or (48)) models lead to the following expressions shown by Equations (50) and (51) when $\phi_3 = 0$ and $\phi_1 + \phi_2 = 1$, that is, in binary conditions:

$$\ln\phi_1^\alpha + \left(1-\frac{V_1}{V_2}\right)\phi_2^\alpha + \chi_{12}^\alpha(\phi_1^\alpha)^2 = \ln\phi_1^\beta + \left(1-\frac{V_1}{V_2}\right)\phi_2^\beta + \chi_{12}^\beta(\phi_1^\beta)^2 \tag{50}$$

$$\ln\phi_2^\alpha + \left(1-\frac{V_2}{V_1}\right)\phi_1^\alpha + \varepsilon_{12}^\alpha(\phi_1^\alpha)^2\frac{V_2}{V_1} = \ln\phi_2^\beta + \left(1-\frac{V_2}{V_1}\right)\phi_1^\beta + \varepsilon_{12}^\beta(\phi_1^\beta)^2\frac{V_2}{V_1} \tag{51}$$

that are those obtained for BPS [23, 25], evidencing the reliability of the models in spite of the mathematical complexity.

The advantage of using $\chi(T, \phi)$ and $\varepsilon(T, \phi)$ from models is the important reduction of the number of unknowns when mathematically solving the Equations (10)–(12). Once equilibrium compositions of each component in both phases are known (ϕ_i^α and ϕ_i^β), the system of equations has 12 unknowns to determine, namely: g_{ij}^α, g_{ij}^β, $(\mathrm{d}g_{ij}/\mathrm{d}\phi_j)^2$, ($ij$ = 12, 13, 23). However, if model **b1** is applied, in Equations (39)–(41) remain only 9 unknowns: α_{ij}, D_{ij} and c_{ij} (ij = 12, 13, 23). The reduction is more drastic if model **b2** is applied, since only 6 unknowns remain in the Equations (47)–(49): D_{ij} and c_{ij} (ij = 12, 13, 23). In order to solve such systems, an additional number of equations must be generated, 6 in the case of **b1** model and 3 in the **b2** one, as it will be explained in the following.

3. Results and discussion

First of all, let us describe the TPS for which the calculations have been focused. They are ten polymer(2)/polymer(3) mixtures in $CHCl_3$ as solvent (component(1)), namely: polystyrene (PS)/poly (vinyl pyridine) (PVPy), poly(styrene-co-methacrylic acid) (PSMAA-3)/PVPy, PSMAA-6/PVPy, PSMAA-7/PVPy, poly(styrene-co-vinyl phenol) (PSVPh-2)/PVPy, PSVPh-4/PVPy, PSVPh-7/PVPy, PS/poly(vinyl pyrrolidone) (PVP), PSMAA-3/PVP and PSVPh-2/PVP; where the number following MMA or VPh indicates the percentage (% in weight) of comonomer in the corresponding copoly-

Table 1. Experimental compositions in equilibrium, ϕ_i^γ (i = 1, 2; $\gamma = \alpha, \beta$), from the binodal curve and randomly generated, u_i^γ and v_i^γ through **b1** model (Equations (39)–(41)), for different ternary solvent(1)/polymer(2)/polymer(3) systems

ϕ_1^α	ϕ_2^α	ϕ_1^β	ϕ_2^β	u_1^α	u_2^α	u_1^β	u_2^β	v_1^α	v_2^α	v_1^β	v_2^β
$CHCl_3$/PS/PVPy											
0.9607	0.0297	0.9753	0.0042	0.9630	0.0298	0.9733	0.0042	0.9606	0.0297	0.9708	0.0042
0.9678	0.0194	0.9761	0.0074	0.9701	0.0194	0.9741	0.0074	0.9677	0.0194	0.9716	0.0074
0.9559	0.0378	0.9781	0.0013	0.9582	0.0379	0.9761	0.0013	0.9558	0.0378	0.9736	0.0013
$CHCl_3$/PSMMA-3/PVPy											
0.7993	0.1745	0.9523	0.0072	0.8012	0.1749	0.9503	0.0072	0.7992	0.1745	0.9479	0.0072
0.8552	0.1182	0.96	0.0096	0.8573	0.1185	0.9580	0.0096	0.8551	0.1182	0.9556	0.0096
0.9290	0.0486	0.9578	0.0181	0.9312	0.0487	0.9558	0.0181	0.9289	0.0486	0.9534	0.0180
$CHCl_3$/PSMMA-6/PVPy											
0.7917	0.1734	0.9112	0.0204	0.7936	0.1738	0.9093	0.0204	0.7916	0.1734	0.9070	0.0203
0.8240	0.1409	0.9078	0.0317	0.8260	0.1412	0.9059	0.0316	0.8239	0.1409	0.9036	0.0316
0.8803	0.0723	0.8982	0.0482	0.8824	0.0725	0.8963	0.0481	0.8802	0.0723	0.8941	0.0480
$CHCl_3$/PSMMA-7/PVPy											
0.7670	0.2087	0.9047	0.0097	0.7668	0.2092	0.9028	0.0097	0.7669	0.2087	0.9006	0.0097
0.8680	0.0925	0.8995	0.0371	0.8701	0.0927	0.8976	0.0370	0.8679	0.0925	0.8954	0.0369
0.9541	0.0241	0.9644	0.0134	0.9564	0.0242	0.9624	0.0134	0.9540	0.0241	0.9600	0.0133
$CHCl_3$/PSVPh-2/PVPy											
0.9009	0.0843	0.9643	0.008	0.9031	0.0845	0.9623	0.0080	0.9008	0.0843	0.9599	0.0080
0.9369	0.0463	0.9656	0.0109	0.9392	0.0464	0.9636	0.0109	0.9368	0.0463	0.9618	0.0109
0.9541	0.0241	0.9644	0.0134	0.9564	0.0242	0.9624	0.0134	0.9540	0.0241	0.9600	0.0133
$CHCl_3$/PSVPh-4/PVPy											
0.8833	0.0814	0.9443	0.0056	0.8854	0.0816	0.9423	0.0559	0.8832	0.0814	0.9400	0.0056
0.9238	0.0445	0.9442	0.0161	0.9260	0.0446	0.9422	0.0161	0.9237	0.0445	0.9399	0.0160
$CHCl_3$/PSVPh-7/PVPy											
0.9211	0.0646	0.9671	0.0051	0.9233	0.0648	0.9651	0.0051	0.9210	0.0646	0.9627	0.0051
0.9397	0.0446	0.9629	0.0138	0.9420	0.0447	0.9609	0.0138	0.9396	0.0446	0.9585	0.0137
$CHCl_3$/PS/PVP											
0.9212	0.0675	0.9511	0.0155	0.9234	0.0677	0.9491	0.0155	0.9211	0.0675	0.9467	0.0154
0.9349	0.0498	0.9522	0.0189	0.9372	0.0499	0.9502	0.0189	0.9348	0.0498	0.9478	0.0188
$CHCl_3$/PSMMA-3/PVP											
0.8277	0.0891	0.8990	0.0024	0.8297	0.0893	0.8971	0.0024	0.8276	0.0891	0.8949	0.0024
0.8741	0.0467	0.8904	0.0208	0.8735	0.0468	0.8885	0.0208	0.8713	0.0467	0.8863	0.0207
$CHCl_3$/PSVPh-2/PVP											
0.8370	0.0927	0.9016	0.0067	0.8390	0.0929	0.8997	0.0067	0.8369	0.0927	0.8975	0.0067
0.8781	0.0447	0.8985	0.0169	0.8802	0.0448	0.8966	0.0169	0.8780	0.0447	0.8944	0.0168

mers. The supplier, characterization and physicochemical properties of all the chemicals used have been recently described, as well as the experimental ternary phase diagrams determined by liquid chromatography with SEC columns [17]. These diagrams have served to obtain all the phase compositions for each component through the tie-lines joining the two phases in equilibrium at the binodal or cloud-point isotherm as explained elsewhere [17, 20–22].

Next, following the methods and procedure described in the Theory section, the volume fractions ϕ_i^γ ($i = 1, 2, 3$; $\gamma = \alpha, \beta$) have been determined for all the phases equilibria of the above TPS and are compiled in Table 1. As mentioned above, Equations (39)–(41) generated through the model **b1** contain 9 unknowns: α_{ij}, D_{ij} and c_{ij} ($ij = 12, 13, 23$) and in order to solve the system, 6 additional equations should be written. These additional equations are analogous in form to Equations (39)–(41) but with new compositions randomly generated, that differ from the original ones by a quantity no larger than ±0.5%. To do this, the original compositions in phase α (ϕ_i^α) are multiplied by the function (1+0.005 Random) [26] and those in phase β (ϕ_i^β) by (1–0.005 Random). Therefore, a new set of compositions, namely u_i^γ ($i = 1, 2, 3$; $\gamma = \alpha, \beta$) are obtained. The third set, ν_i^γ ($i = 1, 2, 3$; $\gamma = \alpha, \beta$), is generated by multiplying the original compositions by the function (1–0.005 Random). Summarizing, the 9 equations are: the (39)–(41) ones formed with ϕ_i^γ, 3 with u_i^γ (compositions very close to ϕ_i^γ and with unknowns concentration dependent assumed to remain invariants) and 3 more with ν_i^γ (also very close to ϕ_i^γ with unknowns also invariant). It must be remarked that u_i^γ and ν_i^γ are randomly generated,

Table 2. Interaction parameters evaluated from Equations (39)–(41) for different ternary polymer systems

ϕ_1^α	χ_{12}^α	χ_{12}^β	χ_{13}^α	χ_{13}^β	χ_{23}^α	χ_{23}^β	ε_{23}^α	ε_{23}^β	g_{12}^α	g_{12}^β	g_{13}^α	g_{13}^β	g_{23}^α	g_{23}^β
$CHCl_3$/PS/PVPy														
0.9607	0.5319	0.5870	0.5533	0.5418	0.1204	0.1559	0.1526	0.2150	0.5020	0.5045	0.5607	0.5612	0.1551	0.2153
0.9678	0.5760	0.5560	0.5350	0.5810	0.0043	0.0035	0.0003	0.0005	0.5760	0.5770	0.4530	0.4520	0.0003	0.0005
0.9559	0.5545	0.5000	0.5322	0.5667	0.0870	0.0930	0.0887	0.1086	0.5540	0.5550	0.5260	0.5250	0.0900	0.1022
0.9597	0.4965	0.4737	0.5350	0.5470	0.0162	0.1395	0.0480	0.4340	0.4630	0.4670	0.5640	0.5650	0.0490	0.4407
0.9645	0.5570	0.6400	0.4650	0.5801	0.0120	0.0120	0.0120	0.0120	0.6440	0.6420	0.4020	0.3980	0.0120	0.0120
$CHCl_3$/PSMMA-3/PVPy														
0.7993	0.6500	0.6910	0.2240	0.6330	0.0130	0.0130	0.0110	0.0120	1.1200	0.7520	0.1310	0.1160	0.0110	0.0120
0.8552	0.6390	0.6530	0.4970	0.5220	–0.0830	–0.0740	–0.0430	–0.0335	1.0805	0.7665	0.0970	0.0920	–0.0440	–0.0341
0.9290	0.7120	0.6690	0.3560	0.5340	–0.0410	–0.0420	–0.0510	–0.0520	0.9090	0.6910	0.1380	0.9534	–0.0520	–0.0530
$CHCl_3$/PSMMA-6/PVPy														
0.7917	0.6630	0.8430	0.2860	0.4950	0.0810	0.0530	0.0520	0.0044	1.0610	0.9230	0.2320	0.2060	0.0520	0.0041
0.8240	0.5740	0.5730	0.5800	0.6110	–0.0780	–0.0670	–0.0630	–0.0330	0.5720	0.5720	0.5650	–0.5610	–0.0640	–0.0340
0.8803	0.6800	0.6980	0.5670	0.6400	–0.0041	–0.0041	–0.0045	–0.0047	0.8113	0.8010	0.2670	0.2600	–0.0074	–0.0048
$CHCl_3$/PSMMA-7/PVPy														
0.7670	0.6800	0.6890	0.4310	0.4370	–0.1280	–0.1720	–0.1440	–0.2140	0.7000	0.6910	0.4500	0.4500	–0.1500	–0.2230
0.8680	0.5650	0.6540	0.5820	0.6010	–0.0390	–0.0310	–0.0270	–0.0002	0.5700	0.5700	0.5260	0.4220	–0.0280	–0.0002
$CHCl_3$/PSVPh-2/PVPy														
0.9009	0.5410	0.5700	0.7751	0.7722	0.1160	0.0221	–0.0680	–0.0690	0.4901	0.5003	0.8242	0.8244	–0.0690	–0.0690
0.9369	0.6010	0.6692	0.4041	0.5253	–0.0191	–0.0173	–0.0142	–0.0086	0.7392	0.7261	0.3111	0.3074	–0.0140	–0.0087
0.9541	0.6441	0.6683	0.4490	0.4970	–0.0044	–0.0043	–0.0022	–0.0022	0.7480	0.7440	0.2960	0.2931	–0.0022	–0.0021
CHCl3/PSVPh-4/PVPy														
0.9238	0.7550	0.7582	0.5140	0.5981	–0.1280	–0.2318	–0.5170	–0.6800	0.7620	0.7611	0.5932	0.5881	–0.5260	–0.6911
CHCl3/PSVPh-7/PVPy														
0.9211	0.5820	0.5670	0.5050	0.5402	–0.2291	–0.2493	–0.2603	–0.2653	0.5590	0.5622	0.4651	0.4643	–0.2641	–0.2702
0.9397	0.5840	0.6192	0.4571	0.5403	–0.0370	–0.0391	–0.0392	–0.0423	0.6661	0.6592	0.3772	0.3743	–0.0402	–0.0420
CHCl3/PS/PVP														
0.9212	0.5921	0.6961	0.5903	0.5900	0.3391	0.2762	0.2991	0.1830	0.7862	0.7623	0.5881	0.5882	0.3042	0.1850
0.9349	0.6470	0.6581	0.5542	0.5271	0.3072	0.3051	0.3011	0.2912	0.6760	0.6742	0.5703	0.5724	0.3052	0.2851
CHCl3/PSMMA-3/PVP														
0.8277	0.7001	0.6362	0.4741	0.5603	–0.1771	–0.1652	–0.1461	–0.0290	0.6342	0.6333	0.3920	0.3853	–0.1481	–0.0291
0.8714	0.7382	0.7753	0.4480	0.4751	–0.0007	–0.0003	0.0027	0.0033	0.8461	0.8311	0.3250	0.3233	0.0028	0.0033
CHCl3/PSVPh-2/PVP														
0.8370	0.7270	0.7510	0.3490	0.3951	–0.0172	–0.0101	0.0015	0.0152	0.9370	0.8752	0.3060	0.3021	0.0015	0.0154
0.8781	0.7641	0.7893	0.4622	0.4971	–0.0072	–0.0076	–0.0103	–0.0107	0.8261	0.8172	0.2953	0.2931	–0.0103	–0.0108

therefore their equations should not be lineal combinations of those formed with ϕ_i^γ. Both composition sets, u_i^γ and ν_i^γ, have been also included in Table 1. Note that the values corresponding to component 3 have been omitted given by Equation (52):

$$\sum_{i=1}^{3}\phi_i = \sum_{i=1}^{3}u_i = \sum_{i=1}^{3}\nu_i \tag{52}$$

Once solved the 9 equations system, the α_{ij}, D_{ij} and c_{ij} (ij = 12, 13, 23) values are obtained being then possible to evaluate the 14 interaction parameters for each compositions set. In Table 2 are gathered the obtained results with **b1** model for all the studied systems.

Let us now discuss the values of the interaction parameters, starting by those determined with the model **b1** (listed in Table 2). The analysis will be done on the χ_{ij}^γ (ij = 12, 13, 23; $\gamma = \alpha, \beta$) and ε_{ij}^α values since they are better known than the g_{ij}^γ parameters [24, 27–29]. In Figure 1, the dependence of the binary χ_{12}^α and χ_{12}^β parameters with the binary compositions $\phi_2^\beta = \phi_2/(1-\phi_3)$ is plotted for the system CHCl3/PS/PVPy, as an example. For the sake of comparison, Figure 1 also shows some χ_{12} values of CHCl3/PS from the literature [30]. The observed behaviour is the typical trend for good solvents and it seems that no disagreement takes place between experimental and theoretical values, neither with the values $\chi_{12}^0 = 0.51, 0.53$ [24] or with $g_{12}^0 = 0.543, 0.720$ [24], where the superscript 0 means infinite dilution. Similar χ_{13}^α and χ_{13}^β values (Table 2) are found at any composition (a narrow composition range), just slightly larger than those found in the literature: $\chi_{13} = 0.35, 0.44$ [24]. Regarding the χ_{23} and ε_{23} values, they appear always lower than experimental, as expected [14, 19].

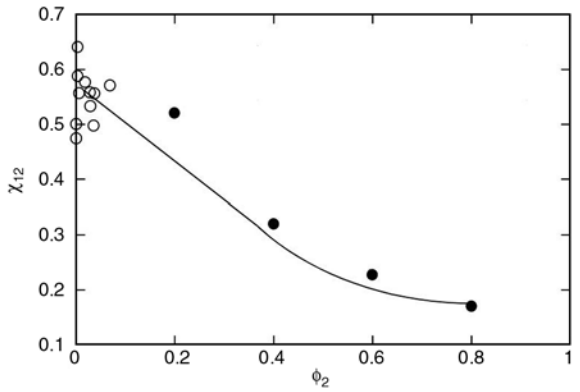

Figure 1. Dependence with composition of χ_{12} interaction parameters evaluated in this paper (o) and literature ones (•) [30], for the CHCl3(1)/PS(2) system

The χ_{ij}^γ and ε_{ij}^γ values for the systems CHCl3/PSMAA-x/PVPy with three different MAA contents are also gathered in Table 2, showing similar behaviours to those above discussed with pure PS as component 2 but with some differences which deserve to be commented. Since no appreciable changes in the values of χ_{12}^α, χ_{12}^β, χ_{13}^α,… at the diverse compositions have been found, it should be more illustrative to use mean values for the parameters; which are listed in Table 3. As seen, χ_{12}^α and χ_{12}^β values smoothly increase with the MAA content in the copolymer, in agreement with the behaviour followed by their intrinsic viscosities, $[\eta_2]$ [17], shown in Figure 2a. The χ_{13}^α and χ_{13}^β values

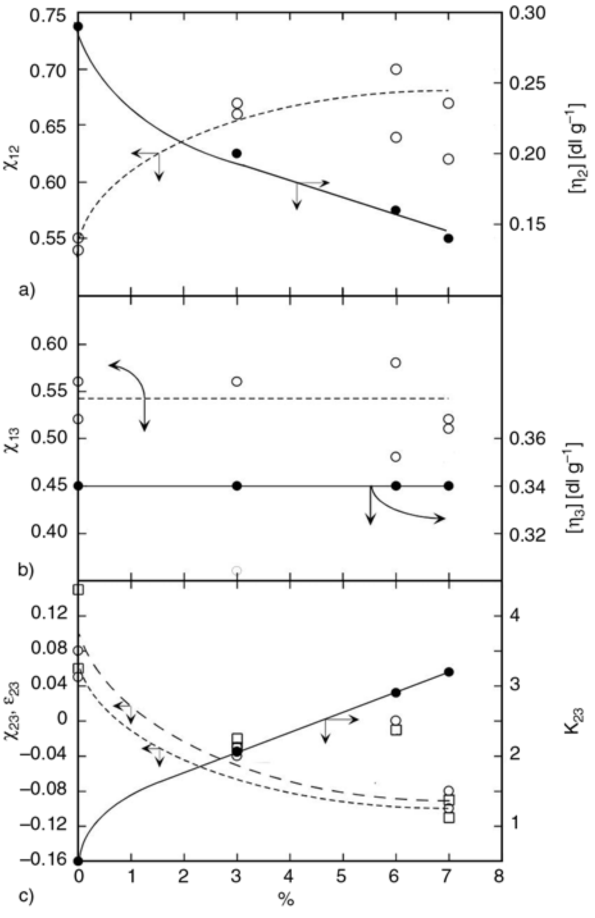

Figure 2. Variation with MAA content (in %) of different magnitudes for the CHCl3(1)/PSMAA-x(2)/PVPy(3) systems: (a) mean interaction parameters $\overline{\chi}_{12}$ from Table 3 (o, ----) and $[\eta_2]$ (•, —); (b) mean interaction parameters $\overline{\chi}_{13}$ from Table 3 (o, ----) and $[\eta_3]$ (•, —); and (c) $\overline{\chi}_{23}$ (o, ----), ε_{23} (□, —) and K_{23} viscometric parameter (•, —) from [17]

practically do not change with MAA content and are smaller than the χ_{12} ones, probably due to the weak hydrogen bonds that can be established between $CHCl_3$ and PVPy because of the slight acid character of $CHCl_3$ [31]. Dependences with MAA content of χ_{13}^{α}, χ_{13}^{β} and $[\eta_3]$ are shown in Figure 2b. As it can be seen, χ_{13} values range between 0.48 and 0.58 and $[\eta_3]$ values do not change with component 2 nature, which seems to indicate that this component has no influence on the 1-3 interactions. Finally, in Figure 2c strong χ_{23} or ε_{23} dependences on copolymer PSMAA composition are observed. The calculated values even reach negative figures, typical of stable blends [14, 27], as the MAA content is raised, probably due to hydrogen bond specific interactions between MAA (H-donor) and PVPy (H-acceptor). Moreover, for these systems, the χ_{23} values can be evaluated through $\chi_{23} = \chi_{PS-PVPy}\phi_{PS}+\chi_{MAA-PVPy}\phi_{MAA}$ with ϕ_{PS} and ϕ_{MAA} standing for the respective volume fractions of PS and MAA in the copolymer [32]. As $\chi_{PS-PVPy}$ displays positive values and decreases with rising MAA content in the copolymer, the term $\chi_{PS-PVPy}\phi_{PS}$ will also decrease. On the other hand, $\chi_{MAA-PVPy}$ will have negative values, decreasing with rising MMA content as it does the term $\chi_{MAA-PVPy}\phi_{MAA}$. Since both terms work in the same direction, the χ_{23} values will decrease with rising MAA content in the copolymer, as seen in Figure 2c and in Table 3. The parallel increase of the K_{23} viscometric parameter [17], also plotted in Figure 2c, confirms the increasing stability of the polymer mixtures as the MMA content goes up. Finally, ε_{23} values in these systems are small and positive in agreement with recently published ones [19].

Table 3 also gathers values of the interaction parameters calculated for $CHCl_3$/PSVPh-y/PVPy systems at three different VPh contents. χ_{12}^{α} and χ_{12}^{β} values smoothly increase with the VPh content, except for the PSVPh-7 where they slightly decrease. In any case, the increase in χ_{12} is in agreement with the decreasing $[\eta_2]$, as shown in Figure 3a. Figure 3b depicts the χ_{13}^{α} and χ_{13}^{β} dependences with VPh content and shows that χ_{13} values remain practically constant (between 0.48 and 0.60), as in the preceding analyzed systems. Again, it seems that the component 2 nature plays scarce if any influence on 1-3 interactions. Finally, Figure 3c shows the χ_{23} or ε_{23} dependences on copolymer composition. As can be seen, decreasing χ_{23} or ε_{23} and increasing K_{23} values when rising the VPh content are the normal behaviours. However, the viscosity values and the ternary phase diagram (figure 2 in ref. [17]) were anomalous in the system $CHCl_3$/PSVPh-7/PVPy, in which a diminution of stability (stable zones outside the binodal) accounts probably due to self-associations competing with inter-associations. The anomalous K_{23} decrease in the PSVPh-7 is also reflected in χ_{23} or ε_{23} values here calculated, as corroborated in Figure 3c.

Similar results have been attained for systems including the H-acceptor PVP as component 3, namely: $CHCl_3$/PS/PVP, $CHCl_3$/PSMAA-3/PVP and $CHCl_3$/PSVPh-2/PVP, as it can be seen in Table 3. The χ_{12}^{α} and χ_{12}^{β} and values slightly increase when rising the H-donor comonomer content in both copolymers, in correspondence with the expected decrease of $[\eta_2]$ [17], as shown in Figure 4. Similar evolutions with MMA or VPh content to the previously discussed systems are also followed by the χ_{12}^{α}, χ_{23}^{α}, $\varepsilon_{12}{}^{\alpha}$, $\varepsilon_{23}^{\alpha}$, parameters. These magnitudes decrease up to small negative values with increasing H-donor comonomer content, whereas the K_{23} viscometric parameters increase, as also seen in Figure 4. As a summary, the results in Table 2, obtained through the **b1**

Table 3. Interaction parameters mean values from Table 2 data

System	$\overline{\chi}_{12}^{\alpha}$	$\overline{\chi}_{12}^{\beta}$	$\overline{\chi}_{13}^{\alpha}$	$\overline{\chi}_{13}^{\beta}$	$\overline{\chi}_{23}^{\alpha}$	$\overline{\chi}_{23}^{\beta}$	$\overline{\varepsilon}_{23}^{\alpha}$	$\overline{\varepsilon}_{23}^{\beta}$
$CHCl_3$/PS/PVPy	0.54	0.55	0.52	0.56	0.05	0.08	0.06	0.15
$CHCl_3$/PSMMA-3/PVPy	0.66	0.67	0.36	0.56	–0.04	–0.03	–0.03	–0.02
$CHCl_3$/PSMMA-6/PVPy	0.64	0.70	0.48	0.58	0.00	0.00	–0.01	–0.01
$CHCl_3$/PSMMA-7/PVPy	0.62	0.67	0.51	0.52	–0.08	–0.10	–0.09	–0.11
$CHCl_3$/PSVPh-2/PVPy	0.60	0.62	0.54	0.60	0.03	0.00	–0.03	–0.03
$CHCl_3$/PSVPh-4/PVPy	0.76	0.76	0.51	0.60	–0.13	–0.23	–0.52	–0.68
$CHCl_3$/PSVPh-7/PVPy	0.58	0.59	0.48	0.54	–0.14	–0.14	–0.15	–0.15
$CHCl_3$/PS/PVP	0.62	0.68	0.57	0.56	0.32	0.29	0.30	0.24
$CHCl_3$/PSMMA-3/PVP	0.72	0.71	0.46	0.52	–0.09	–0.08	–0.07	–0.01
$CHCl_3$/PSVPh-2/PVP	0.74	0.77	0.41	0.45	–0.01	–0.01	0.00	0.07

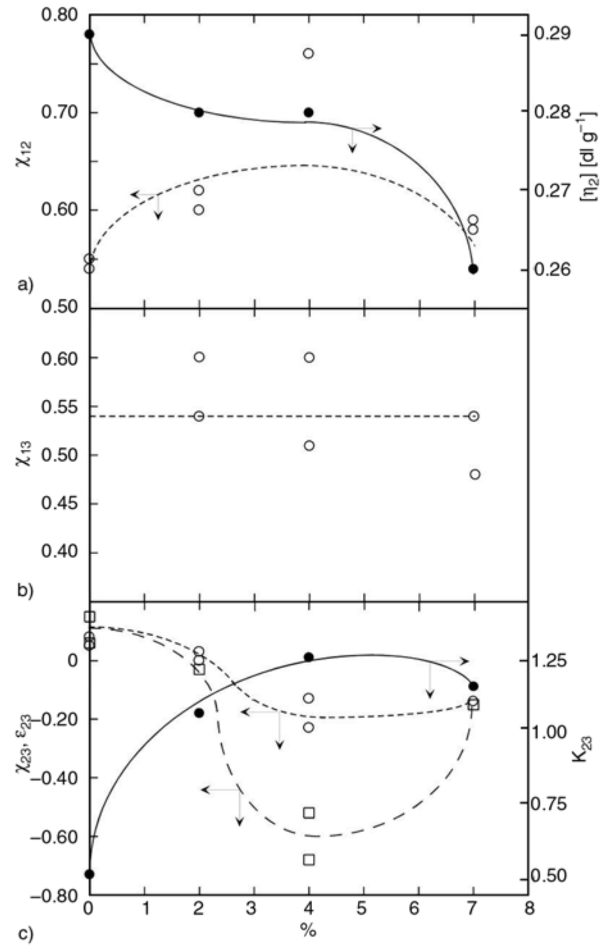

Figure 3. Variation with MAA content (in %) of different magnitudes for the $CHCl_3(1)$/PSVPh-y(2)/PVPy(3) systems: (a) mean interaction parameters $\overline{\chi}_{12}$ from Table 3 and $[\eta_2]$; (b) mean interaction parameters $\overline{\chi}_{13}$ from Table 3; and (c) $\overline{\chi}_{23}$, ε_{23} and K_{23} viscometric parameter from [17]. Symbols as in Figure 2

model (Equations (39)–(41)) seem to be satisfactory and even values as $g_{13} = 0.46_3$ for the $CHCl_3$/PVPy system [24] or $g_{12} = 0.54_3$, 0.72_0 for the $CHCl_3$/PS system [24] are fairly reflected in the corresponding data of Table 2. In conclusion, it can be quoted that the **b1** approach is a good enough procedure to describe and calculate the interaction parameters.

On the other hand, the molar volumes, V_i, necessary to apply the **b2** model (Equations (47)–(49)) were deduced from data on specific volumes and molar masses of the components and were previously reported [17]. The application of model **b2** leads to 6 unknowns (D_{ij} and c_{ij} with ij = 12, 13, 23) and therefore, 6 equations are necessary to deduce them: 3 of them are generated with the original compositions ϕ_i^γ and the other three by applying

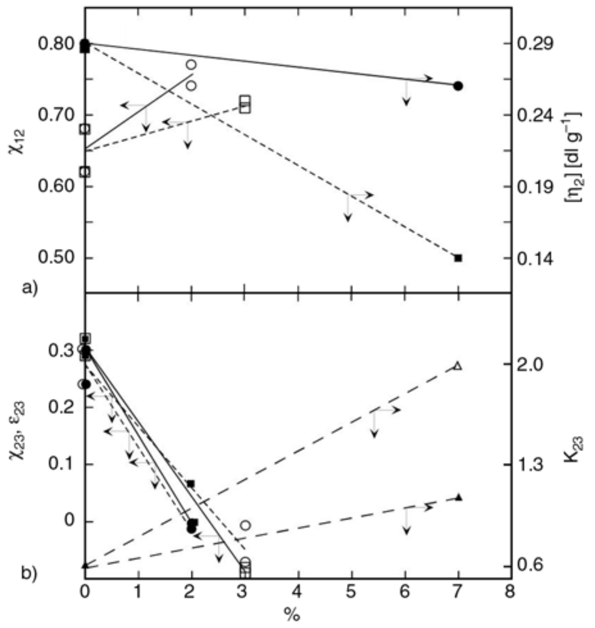

Figure 4. (a) Variation with component 2 nature and composition of χ_{12} interaction parameters for $CHCl_3(1)$/PSMAA-x(2)/PVP(3) (□, ----) and $CHCl_3(1)$/PSVPh-y(2)/ PVP(3) systems (○, ----), as well as $[\eta_2]$ intrinsic viscosities from [17] for $CHCl_3(1)$/PSMAA-x(2)/PVP(3) (■, ----) and $CHCl_3(1)$/PSVPh-y(2)/PVP(3) systems (•, —); (b) Variation with component 2 composition and nature of χ_{23} (squares, —) and ε_{23} (circles, ----) interaction parameters and K_{23} viscometric parameters from [17] (triangles, ----) for $CHCl_3(1)$/PSMAA-x(2)/PVP(3) (empty symbols) and $CHCl_3(1)$/PSVPh-y(2)/PVP(3) (filled symbols) systems

randomly generated compositions u_i^γ. In Table 4 are gathered ϕ_1^α (the remaining ϕ_i^γ values have been already given in Table 1) and u_i^γ values. Once solved the 6 equations system, it is possible to obtain the 14 interaction parameters for each composition set of any system, which are compiled in Table 5. As before, mean values of χ_{12}^γ, χ_{13}^γ, χ_{23}^γ, and ε_{23}^γ, ($\gamma = \alpha$, β) have been gathered in Table 6. For the system $CHCl_3$/PS/PVPy the χ_{12}^α mean values seem to be acceptable, but the χ_{12}^β ones are extremely low and incomprehensible. Similar behaviours follow the χ_{13}^α and χ_{13}^β values, that is, very low values becoming strongly negative as the H-donor comonomer content raises. The χ_{13} small positive values for the systems $CHCl_3$/PVPy or $CHCl_3$/PVP are not supported by literature results, and the strongly negative ones neither can be explained by the weakly H-donor character of $CHCl_3$ [31]. The obtained values seem to be the

Table 4. Experimental compositions in equilibrium, ϕ_1^α, from the binodal curve and randomly generated, u_i^γ (i = 1, 2, 3; $\gamma = \alpha, \beta$), through **b2** model (Equations (47)–(49)) for different ternary polymer systems

ϕ_1^α	u_1^α	u_2^α	u_3^α	u_1^β	u_2^β	u_3^β
$CHCl_3$/PS/PVPy						
0.9607	0.9611	0.0297	0.0092	0.9720	0.0042	0.0238
0.9678	0.9682	0.0194	0.0124	0.9728	0.0074	0.0198
0.9559	0.9563	0.0378	0.0059	0.9748	0.0013	0.0239
$CHCl_3$/PSMMA-3/PVPy						
0.7993	0.7996	0.1746	0.0258	0.9491	0.0072	0.0437
0.8552	0.8556	0.1182	0.0262	0.9568	0.0096	0.0337
0.9290	0.9294	0.0486	0.0220	0.9546	0.0180	0.0274
$CHCl_3$/PSMMA-6/PVPy						
0.7917	0.7920	0.1735	0.0345	0.9081	0.0203	0.0716
0.8240	0.8243	0.1410	0.0347	0.9047	0.0316	0.0637
0.8803	0.8807	0.0723	0.0470	0.8952	0.0480	0.0568
$CHCl_3$/PSMMA-7/PVPy						
0.7670	0.7673	0.2088	0.0239	0.9016	0.0097	0.0887
0.868	0.8684	0.0925	0.0391	0.8965	0.0370	0.0666
$CHCl_3$/PSVPh-2/PVPy						
0.9009	0.9013	0.0843	0.0144	0.9610	0.0080	0.0310
0.9369	0.9373	0.0463	0.0164	0.9623	0.0109	0.0268
0.9541	0.9545	0.0241	0.0214	0.9611	0.0134	0.0255
$CHCl_3$/PSVPh-4/PVPy						
0.8833	0.8837	0.0814	0.0349	0.9411	0.0558	0.0533
0.9238	0.9242	0.0445	0.0313	0.9410	0.0160	0.0429
$CHCl_3$/PSVPh-7/PVPy						
0.9211	0.9215	0.0646	0.0139	0.9638	0.0051	0.0311
0.9397	0.9410	0.0446	0.0153	0.9596	0.0138	0.0266
$CHCl_3$/PS/PVP						
0.9212	0.9216	0.0675	0.0109	0.9479	0.0154	0.0367
0.9349	0.9353	0.0498	0.0149	0.9490	0.0188	0.0322
$CHCl_3$/PSMMA-3/PVP						
0.8277	0.8280	0.0891	0.0828	0.8960	0.0024	0.1016
0.8741	0.8718	0.0467	0.0815	0.8874	0.0207	0.0919
$CHCl_3$/PSVPh-2/PVP						
0.8370	0.8373	0.0927	0.0699	0.8986	0.0067	0.0948
0.8781	0.8785	0.0447	0.0768	0.8955	0.0168	0.0877

most appropriate, since these magnitudes use to display small positive [19] or negative [14, 26] values in blends. However, as seen before and as expected, they do not become more negative with increasing the H-donor content of copolymer neither follow the expected viscometric behaviour [17]. As a summary, obtained results from **b2** model (Equations (47)–(49)) are unsatisfactory, in sharp contrast with those determined with the **b1** model (Equations (39)–(41)). Probably, the main reason for these results is the fact that the α parameter is used in the **b1** model but ignored in the **b2** approach. As a conclusion, the obtained interaction parameters through the **b1** approach are considerably better than those coming from **b2** approach, in spite of the need of an additional fitting parameter in the former, an aspect long supported for binary solvent/polymer systems [33].

4. Conclusions

Two theoretical approaches to calculate χ_{ij} or ε_{ij} and g_{ij} interaction parameters in ternary polymer systems with specific interactions have been proposed. The validity of both models has been checked and assessed by comparison between the calculated values and those experimentally obtained through ternary phase diagrams. In general, the values calculated with model **b1** (Equations (39)–(41)) show a fair agreement with the experimental ones found in the literature. Moreover, in the systems where the component 2 is a

Table 5. Interaction parameters evaluated from Equations (47)–(49) for different ternary polymer systems

ϕ_1^α	χ_{12}^α	χ_{12}^β	χ_{13}^α	χ_{13}^β	χ_{23}^α	χ_{23}^β	ε_{23}^α	ε_{23}^β	g_{12}^α	g_{12}^β	g_{13}^α	g_{13}^β	g_{23}^α	g_{23}^β
$CHCl_3$/PS/PVPy														
0.9607	0.5066	0.0727	0.1146	0.3439	0.0247	0.0249	0.0022	0.0035	0.0160	0.0018	0.0050	0.0101	0.6549	1.1110
0.9678	0.4405	0.2228	–0.0466	–0.0637	0.0452	0.0056	0.0006	0.0008	0.0141	0.0053	0.0489	0.0504	0.1614	0.2074
0.9559	0.4485	–0.0297	0.0291	0.0834	0.0211	0.0254	0.0015	0.0037	0.0209	0.0070	0.0021	0.0040	0.4158	1.0347
$CHCl_3$/PSMMA-3/PVPy														
0.7993	0.5489	0.0623	–0.4608	–2.3319	–0.0419	–0.0282	0.0005	0.0007	0.1124	0.0032	0.8730	0.9370	0.1301	0.1944
0.8552	0.5388	0.0889	–0.2358	–0.9588	0.1793	0.2316	0.0007	0.0008	0.0665	0.0037	1.1279	1.1377	0.1712	0.1970
0.9290	0.4674	0.1402	–0.1137	–0.1975	–0.0402	–0.0408	0.0003	0.0003	0.0207	0.0054	0.2416	0.2426	0.0750	0.0810
$CHCl_3$/PSMMA-6/PVPy														
0.7917	0.5747	0.1232	–0.0364	–0.1013	0.1183	0.2574	0.0001	0.0002	0.1410	0.0127	0.2740	0.2904	0.0289	0.0592
0.8240	0.5888	0.0755	–0.1061	–0.2283	0.2525	0.4653	0.0002	0.0003	0.0592	0.0071	0.6076	0.6366	0.0450	0.0795
0.8803	0.2396	0.0053	–0.5110	–0.6165	–0.0978	–0.0971	0.0019	0.0022	0.0015	0.0003	1.0170	1.0323	0.5283	0.5881
$CHCl_3$/PSMMA-7/PVPy														
0.7670	0.5175	0.0680	–0.0431	–0.1317	0.0307	0.1838	0.0003	0.0011	0.1346	0.0051	0.3673	0.4094	0.0630	0.2482
0.8680	0.3650	0.0359	–0.3033	–1.2969	0.0549	0.0626	0.0033	0.0101	0.1650	0.0032	0.0342	0.0741	0.6810	1.5535
$CHCl_3$/PSVPh-2/PVPy														
0.9009	0.4118	0.0591	–0.1178	–0.3544	0.1823	0.3546	0.0001	0.0002	0.0324	0.0021	0.3460	0.3590	0.0390	0.0746
0.9369	0.3796	0.0249	–0.1983	–0.3770	0.1993	0.2840	0.0001	0.0002	0.0074	0.0008	0.3552	0.3621	0.0526	0.0741
0.9541	0.1806	0.0182	–0.1404	–0.1830	0.1018	0.1023	0.0003	0.0003	0.0017	0.0005	0.1773	0.1774	0.1267	0.1240
$CHCl_3$/PSVPh-4/PVPy														
0.8833	0.4600	–0.0683	–0.5441	–1.9430	–0.0001	–0.0001	0.0000	0.0000	0.0524	0.0034	0.0670	0.1006	0.0176	0.0181
0.9238	0.4175	0.0056	–0.3700	–0.5203	–0.0053	–0.0014	0.0005	0.0008	0.0025	0.0003	0.5899	0.6017	0.1280	0.1967
$CHCl_3$/PSVPh-7/PVPy														
0.9211	0.5636	0.1174	–0.0030	–0.0076	0.0039	0.0064	0.0000	0.0000	0.0410	0.0030	0.0076	0.0079	0.0109	0.0210
0.9397	0.5512	0.2829	–0.0206	–0.0346	0.0225	0.0338	0.0000	0.0000	0.0342	0.0103	0.0384	0.0392	0.0004	0.0006
$CHCl_3$/PS/PVP														
0.9212	0.4279	0.0270	0.0201	0.1283	0.0527	0.0647	0.0022	0.0045	0.0117	0.0012	0.0016	0.0055	0.6125	1.3915
0.9349	0.3065	0.0748	–0.0421	–0.0592	0.0234	0.0246	0.0013	0.0019	0.0123	0.0032	0.0782	0.0811	0.3676	0.5789
$CHCl_3$/PSMMA-3/PVP														
0.8277	0.4470	0.0055	–0.8054	–1.5043	–0.0680	–0.0633	0.0008	0.0009	0.0451	0.0006	0.8576	0.9010	0.2037	0.2388
0.8714	0.2230	0.0042	–0.2872	–0.3460	–0.0414	–0.0415	0.0006	0.0006	0.0026	0.0004	0.7975	0.8069	0.1536	0.1655
$CHCl_3$/PSVPh-2/PVP														
0.8370	0.4245	0.0515	–0.0503	–0.0911	0.1362	0.1861	0.0000	0.0001	0.0496	0.0033	0.2941	0.3037	0.0126	0.0168
0.8781	0.2576	0.0033	–0.6400	–0.7908	0.2147	0.2542	0.0013	0.0014	0.0026	0.0003	0.9441	0.9600	0.4402	0.4900

Table 6. Interaction parameters mean values from Table 5 data

System	$\bar{\chi}_{12}^\alpha$	$\bar{\chi}_{12}^\beta$	$\bar{\chi}_{13}^\alpha$	$\bar{\chi}_{13}^\beta$	$\bar{\chi}_{23}^\alpha$	$\bar{\chi}_{23}^\beta$	$\bar{\varepsilon}_{23}^\alpha$	$\bar{\varepsilon}_{23}^\beta$
$CHCl_3$/PS/PVPy	0.47	0.11	0.03	0.12	0.03	0.04	0.00	0.00
$CHCl_3$/PSMMA-3/PVPy	0.52	0.10	–0.27	–1,16	0.03	0.05	0.00	0.00
$CHCl_3$/PSMMA-6/PVPy	0.47	0.07	–0.22	–0.32	0.09	0.21	0.00	0.00
$CHCl_3$/PSMMA-7/PVPy	0.44	0.05	–0.17	–0.71	0.04	0.12	0.00	0.01
$CHCl_3$/PSVPh-2/PVPy	0.32	0.03	–0.15	–0.30	0.16	0.25	0.00	0.00
$CHCl_3$/PSVPh-4/PVPy	0.44	0.04	–0.46	–1.23	0.00	0.00	0.00	0.00
$CHCl_3$/PSVPh-7/PVPy	0.56	0.20	–0.01	–0.02	0.01	0.02	0.00	0.00
$CHCl_3$/PS/PVP	0.37	0.05	–0.01	0.03	0.04	0.04	0.00	0.00
$CHCl_3$/PSMMA-3/PVP	0.34	0.01	–0.55	–0.93	–0.05	–0.05	0.00	0.01
$CHCl_3$/PSVPh-2/PVP	0.34	0.03	–0.35	–0.44	0.18	0.22	0.00	0.00

copolymer, the χ_{13} values practically do not change with the copolymer content (MMA or VPh) denoting that the chemical nature of this component has no influence on the 1-3 interactions. On the contrary, strong χ_{23} or ε_{23} dependences on copolymer composition are observed. The calculated values even reach negative figures, typical of stable blends, as the comonomer content is raised, probably due to hydrogen bond specific interactions between the H-donor (PSMAA or PSVPh) and the H-acceptor (PVPy or PVP), in correspondence with the experimental viscometric data. However, the obtained results from **b2** model (Equations (47)–(49)) are quite unsatisfactory, in sharp contrast with those determined with the **b1** model, most probably due to the fact that the later model contains an empirical entropy correction (α parameter) that is ignored in the other approach. Therefore, as a main conclusion, it can be quoted that the **b1** approach is a good enough mathematical procedure to describe and calculate interaction parameters, at least for the TPS here compared and for all the phase compositions assayed.

Acknowledgements

The authors acknowledge financial support from Ministerio de Educación y Ciencia, Spain, through the Project: MAT2006-03997.

References

[1] Bouslah N., Amrani F.: Miscibility and specific interactions in blends of poly[(styrene)-co-(cinnamic acid)] with poly(methyl methacrylate) and modified poly(methyl methacrylate). Express Polymer Letter, **1**, 44–50 (2007).

[2] Barton A. F. M.: Handbook of solubility parameters and other cohesion parameters. CRC Press, Boca Raton (1983).

[3] Barton A. F. M.: Handbook of polymer-liquid interaction parameters and solubility parameters. CRC Press, Boca Raton (1990).

[4] Kamide K.: Thermodynamics of polymer solutions: Phase equilibria and critical phenomena. Elsevier, Amsterdam (1990).

[5] Uriarte C., Fernandez-Berridi M. J., Elorza J. M., Iruin J. J., Kleintjens L.: Determination of the interaction parameter *g* by inverse gas chromatography: An additional experimental test of the classic lattice model. Polymer, **30**, 1493–1497 (1989).

[6] Staverman A. J.: Cohesive energy of liquid mixtures I. Recueil des Travaux Chimiques, **56**, 885–890 (1937).

[7] Koningsveld R., Kleintjens L. A.: Liquid-liquid phase separation in multicomponent polymer systems. X. Concentration dependence of the pair-interaction parameter in the system cyclohexane-polystyrene. Macromolecules, **4**, 637–641 (1971).

[8] Bondi A.: Van der Waals volumes and radii. Journal of Physical Chemistry, **68**, 441–451 (1964).

[9] Bae Y. C., Shim J. J., Soane D. S., Prausnitz J. M.: Representation of vapor-liquid and liquid-liquid equilibria for binary systems containing polymers: Applicability of an extended Flory-Huggins equation. Journal of Applied Polymer Science, **47**, 1193–1206 (1993).

[10] Bae Y. C., Lambert S. M., Soane D. S., Prausnitz J. M.: Cloud-point curves of polymer solutions from thermooptical measurements. Macromolecules, **24**, 4403–4407 (1991).

[11] Rico M., Ramirez C., Montero B., Diez J., Lopez J.: Phase diagram for a system of polydisperse components consisting of the precursor of an epoxy/diamine thermoset and a thermoplastic: Analysis based on a lattice theory model. Macromolecular Theory and Simulations, **15**, 487–496 (2006).

[12] Riccardi C. C., Borrajo J., Meynie L., Fenouillot F., Pascault J-P.: Thermodynamic analysis of the phase separation during the polymerization of a thermoset system into a thermoplastic matrix. Part II. Prediction of the phase composition and the volume fraction of the dispersed phase. Journal of Polymer Science, Part B: Polymer Physics, **42**, 1361–1368 (2004).

[13] Schreiber H. P., Patterson D., Tewari Y. B., Guillet J. E.: Application of gas-liquid chromatography to the thermodynamics of polymer solutions. Macromolecules, 4, 356–359 (1971).

[14] Uriarte C., Iruin J. J., Fernandez-Berridi M. J., Elorza J. M.: Chromatographic studies of a poly(vinyl methyl ether)/phenoxy resin blend near the lower critical solution temperature. Polymer, **30**, 1155–1159 (1989).

[15] Schuld N., Wolf B. A.: Polymer-solvent interaction parameters. in 'Polymer Handbook' (eds.: Brandrup J., Immergut E. H., Grulke E. A.), Wiley-Interscience, New York, 247–264 (1999).

[16] Mumby S. J., Sher R.: Determination of χ from liquid-liquid phase data and the computation of phase diagrams for quasi-binary polymer solutions and blends. Macromolecules, **27**, 689–694 (1994).

[17] Torrens F., Soria V., Codoñer A., Abad C., Campos A.: Compatibility between polystyrene copolymers and polymers in solution via hydrogen bonding. European Polymer Journal, **42**, 2807–2823 (2006).

[18] Soria V., Figueruelo J. E., Gómez C. M., Abad C., Campos A.: Ternary polymer solutions with hydrogen bonds. 1. Theory. Macromolecular Theory and Simulations, **16**, 53–61 (2007).

[19] Figueruelo J. E., Monzó I. S., Gómez C. M., Soria V., Abad C., Campos A.: Ternary polymer solutions with hydrogen bonds. 2. Prediction of Phase Diagrams. Macromolecular Theory and Simulations, **16**, 62–76 (2007).

[20] Gómez C. M., Verdejo E., Figueruelo J. E., Campos A., Soria V.: On the thermodynamic treatment of poly(vinylidene fluoride)/polystyrene blend under liquid-liquid phase separation conditions. Polymer, **36**, 1487–1498 (1995).

[21] Campos A., Gómez C. M., García R., Figueruelo J. E., Soria V.: Extension of the Flory-Huggins theory to study incompatible polymer blends in solution from phase separation data. Polymer, **37**, 3361–3372 (1996).

[22] Gómez C. M., Figueruelo J. E., Campos A.: Evaluation of thermodynamic parameters for blends of polyether sulfone and poly(methyl methacrylate) or polystyrene in dimethylformamide. Polymer, **39**, 4023–4032 (1998).

[23] Gómez C. M., Porcar I., Monzo I. S., Abad C., Campos A.: Modelling the influence of nanoparticles in the phase behaviour of an epoxy/polystyrene mixture. European Polymer Journal, **43**, 360–373 (2007).

[24] Campos A., Gavara R., Tejero R., Gomez C., Celda B.: A Flory-Huggins thermodynamic approach for predicting sorption equilibrium in ternary polymer systems. Journal of Polymer Science, Part B: Polymer Physics, **27**, 1569–1597 (1989).

[25] Torrens F., Monzó I. S., Gómez C. M., Abad C., Campos A.: Study and comparison of interaction parameter and phase behaviour of epoxy/polystyrene and epoxies copolymer polystyrene-b-polymethylmethacrylate blends. Polymer Composites (in press) DOI: 10.1002/pc.20518 (2008).

[26] Wolfram S.: The mathematica book. Wolfram Media, Champaign (2003).

[27] Prolongo M. G., Masegosa R. M., Horta A.: Polymer-polymer interaction parameter in the presence of a solvent. Macromolecules, **22**, 4346–4351 (1989).

[28] Masegosa R. M., Prolongo M. G., Horta A.: The *g* interaction parameter of polymer-solvent systems. Macromolecules, **19**, 1478–1486 (1986).

[29] Figueruelo J. E., Celda B., Campos A.: Predictability of properties in ternary solvent (1)/solvent(2)/polymer(3) systems from interaction parameters of the binary systems. 1. General considerations and evaluation of preferential solvation coefficients. Macromolecules, **18**, 2504–2511 (1985).

[30] Brandrup J., Immergut E. H., Grulke E. A.: Polymer Handbook, Wiley Interscience, New York (1999).

[31] Marcus Y.: The properties of solvents. John Wiley and Sons, New York (1998).

[32] Champetier G., Monnerie L.: Introduction a la chimie macromoleculaire. Masson and Cie, Paris (1969).

[33] Walsh D. J., Higgins J. S., Maconnachie A.: Polymer blends and mixtures. NATO ASI Series E: Applied Science (1985).

eXPRESS Polymer Letters Vol.2, No.5 (2008) 330–338
Available online at www.expresspolymlett.com
DOI: 10.3144/expresspolymlett.2008.39

Synthesis and characterization of novel water-soluble polyamide based on spermine and aspartic acid as a potential gene delivery vehicle

B. M. Viola[1,4], T. E. Abraham[1], D. S. Arathi[2], E. Sreekumar[2], M. R. Pillai[2], T. J. Thomas[3], C. K. S. Pillai[1,4]*

[1]Chemical Sciences & Technology Division, Regional Research Laboratory, Council of Scientific and Industrial Research, Thiruvananthapuram-695 019, India
[2]Rajiv Gandhi Centre for Biotechnology, Thiruvananthapuram-695 014, India
[3]Department of Medicine, University of Medicine and Dentistry, Robert Wood Johnson Medical School, NJ 08903, USA
[4]Sree Chitra Thirunal Institute for Medical Sciences & Technology, BMT Wing, Poojappura, Thiruvananthapuram-695 012, India

Received 4 January 2008; accepted in revised form 20 March 2008

Abstract. We developed a novel and convenient method for the synthesis of a potentially safe non-viral gene delivery vehicle based on the cationic block copolymer of spermine and aspartic acid (ASSP) and coupled it with polyethylene glycol (PEG). The copolymer ASSP was prepared by direct polycondensation in the ionic liquid, butylmethylimidazolium hexafluorophosphate, using triphenyl phosphite as the condensing agent under mild reaction conditions. The highly hydrophobic ASSP was transformed into a water soluble hydrophilic micelle by coupling ASSP with polyethylene glycol (PEG) using the same ionic liquid and 1,1-carbonyl diimidazole as the condensing agent without harsh conditions. The polycationic ASSP-PEG was then used to condense calf thymus and plasmid deoxyribonuclceic acids (DNAs) in Tris-HCl buffer (pH 7.4) to get a series of block ionomer complexes with various charge ratios. The physicochemical properties of the copolymer micelle and the DNA polyplexes were studied using fourier transform-infrared (FTIR), nuclear magnetic resonance (NMR) and circular dichroism (CD) spectroscopy, matrix assisted laser desorption/ionization-time of flight mass spectrometry (MALDI-TOF MS), differential scanning calorimetry (DSC), transmission electron microscopy (TEM) and particle size measurements. It was observed that the DNA was condensed to compact particles by its interaction with the copolymer. Since DNA condensation to nano/micrometer sized particles is essential for gene delivery, our results indicate a potential use of the copolymer for gene delivery applications.

***Keywords:** nanomaterials, gene delivery vector, water-soluble polyamide, DNA polyplexes, synthesis*

---

1. Introduction

The basic concept of gene therapy involves the treatment of human diseases by transferring genetic material to specific cell types in order to correct or supplement defective genes responsible for disease development [1]. Progress in the clinical development of this approach has been hampered by the inefficient transport of plasmid DNA/oligonucleotides through the cell membrane. Therefore, the success of gene therapy is largely dependent on the development of efficient gene delivery vehicles. There are two types of carriers used in experimental gene therapy protocols, viral and non-viral vectors, both of which present specific advantages and disadvantages [2]. The search for non-viral vectors began when viral vectors met with serious draw-

---

[*]Corresponding author, e-mail: ckspillai@yahoo.com

backs such as high risk of mutagenicity, immunogenicity, low production yield, and limited ability to carry long gene sequences [3]. Several approaches have been tested in order to circumvent problems associated with each type of non-viral gene delivery vehicles [4, 5]. The use of polymeric materials as delivery vehicles has been well established and widely used to improve therapeutic potential of peptides, proteins, small molecules and oligonucleotides [6–19].

The cationic molecules which are currently under development as gene delivery vehicles are organic cations, including cationic lipids, polyamine-based polymers, chitosan based polymers, dendrimers, and polyethyleneimine (PEI) [1, 3, 4, 7–10, 13, 16, 20–24]. The spontaneous formation of polyplexes by the interaction of negatively charged phosphate groups of DNA/oligonucleotides and positively charged polymers under physiological salt conditions and the successful transport of these polyplexes to cells has been demonstrated [25–33]. Several investigators have reported encouraging results on spermine and its chemical analogues DNA condensing agents for gene therapy applications [34–38]. Since DNA molecules condensed with low-molecular weight cations are susceptible to aggregation under physiological conditions [39], advanced polymeric gene delivery systems employ macromolecules, with high cationic charge density, that can protect the DNA from degradation [40]. So, this has necessitated attempts towards modification of spermine with a view to developing high molecular weight copolymers [40–43].

Jere *et al.* have reported synthesis of a poly(β-amino ester) of spermine and poly(ethylene glycol) (PEG), which showed higher degree of safety and transfection efficiency in comparison to polyethyleneimine, when studied in 293T human kidney carcinoma cells [40]. On the other hand, Vinogradov *et al.* [41] reported that poly(ethylene glycol)-spermine complexes are less stable in the presence of low molecular weight electrolytes compared to the PEG-PEI complexes. Domb and coworkers [42, 43] showed that dextran grafted spermine improved cell transfection compared to the unmodified one. Kanatani *et al.* [44] showed that pullulan-spermine-mediated transfection of plasmid DNA resulted in greatly reduced cytotoxicity and a 10-fold increase in the level of gene expression when compared to lipofectamine 2000, a commercially available cationic lipid. A copolymer of spermine with amino acids such as aspartic acid and glutamic acid might present a number of advantages, including biocompatibility and biodegradability. The loss of charge density on copolymerization might be compensated by the presence of the additional amino group which could be protected during polymerization. Coupling the copolymer with hydrophilic compounds, such as PEG, might reduce non-specific interaction of the copolymer with blood components as well as make it water soluble. The goal of the present work was to synthesize and characterize a novel cationic polymer based on the naturally occurring polyamine, spermine and aspartic acid, using an ionic liquid and triphenyl phosphite as solvent and condensing agent, respectively. Since ionic liquids have negligible vapor pressure, they are attractive agents for use as 'green' reaction media and can potentially replace conventional organic solvents in synthesis and other applications.

2. Experimental

2.1. Materials

Plasmid DNA, spermine, methyl imidazole HPF6 and chlorobutane (Sigma Aldrich) N-tert-butyloxycarbonyl (Boc)-L-aspartic acid, triphenyl phosphate, 1,1-carbonyl diimidazole, polyethylene glycol metyl ether (MW = 2000) (Aldrich) were used as received. Calf thymus DNA (molecular weight = $6\cdot10^6$) was obtained from Worthington Biochemical Corporation, USA. Plasmid pEGFP (3.4 kilo base pair length), which has the early promoter of CMV and enhanced green fluorescence protein (EGFP) gene was obtained from Clontech.

2.2. Preparation of ionic liquids

The ionic liquid butylmethylimidazolium hexafluorophosphate were synthesized according to the literature [45].

2.3. Copolymerization of Boc-Aspartic acid and spermine (Boc-ASSP)

Boc-ASSP was prepared by stirring N-Boc-L-aspartic acid (0.001 mol), spermine 4HCl (0.001 mol), and 3.2 g of ionic liquid at room temperature for 10 min, and 0.52 ml (0.00225 mol) of triphenyl phosphite was added. The temperature was gradually elevated to 100°C under an inert gas atmosphere, the reaction mixture was held at this temperature, and stirring for 2.5 h. Boc-ASSP was isolated by precipitation in excess methanol. Polymer was thoroughly washed with methanol and dried in vacuum at 70°C.

2.4. Deprotection of N-BOC fron BOC-ASSP

Manual removal of the N-terminal Boc group can be accomplished by placing the resin in a RB flask and washing with 50% [v/v] trifluoroacetic acid (TFA)/dichloromethane (DCM) for 15 min at room temperature with constant stirring. After 15 min, the mixture was extracted with ethyl acetate and washed with sodium bicarbonate solution and then with saturated sodium chloride solution. The product was the precipitated with methanol.

2.5. Synthesis of PEG–ASPSP

A 1 mmole portion of polyethylene glycol methyl ether (MW = 2000) was dissolved in 5 ml of ionic liquid and reacted with 1 mmole of 1,1-carbonyl diimidazole at 20°C for 3 hours. This reaction modifies the terminal hydroxyl group of polyethylene glycol methyl ether. The reaction system was then supplemented with 1mmole of ASSP and the mixture incubated at 20°C for 16 hours. The product was then precipitated in DCM and the ionic liquid is recovered by evaporating the DCM.

2.6. Characterization of ASSP-PEG

NMR spectra of the compound were recorded using 300-MHz Brucker NMR spectrophotometer in D_2O. Infrared spectra of the polymers were recorded using an IR prestige-21 FT-IR Shimadzu spectrophotometer in the range of 4000–400 cm^{-1}. The thermal stability of the polymers was determined using DTG-60 Shimadzu thermo- gravimetric analyzer at a heating rate of 10°C/min in nitrogen. The thermal transitions of the polymers were determined using a Perkin-Elmer DSC-7 differential scanning calorimeter under nitrogen purge. The samples were heated at a rate of 10°C/min. The MALDI TOF MS were run using a Micro mass TofSpec 2E instrument using a nitrogen 337 nm laser (4 ns pulse). At least 40–50 shots are summed up. The matrix used is 2,5-dihydroxy benzoic acid dissolved in water. The sample ASSP is dissolved in water and the matrix spotted in MALDI target and allowed to dry before introducing into the mass spectrometer. The solution of the polymer ASSP and ASSP-PEG in water was prepared in a concentration of 1 mg/1 ml and the primary amine content was determined according to the procedure described elsewhere [45].

2.7. DNA-ASPSP-PEG complex formation

A solution of the polymer ASPSP-PEG in Tris-HCl buffer (pH 7.4) was prepared at a concentration of 1 µg/µl. Calf thymus and Plasmid DNA solutions were also prepared in the same buffer in at a concentration of ~1 µg/µl. A series of block ionomer complexes (BIC) at various charge ratios were prepared by mixing ASPSP-PEG solution with a DNA solution. The mixture was mixed by vortexing for 2–3 min and incubated for 30 min. at room temperature for completing the complex formation. It was noted that during complex preparation, the volume of DNA was kept constant and volume of polymer solution was adjusted for the theoretical charge ratio. The dispersive stability of the complexes was evaluated by turbidity measurement at 500 nm using UV-Vis spectrophotometer (PerkinElmer-Lamda-35).

2.8. Particle size measurement

The polyplexes were prepared at increasing weight ratios from 1:0.25 to 1:1.5 (DNA/Polymer) in Tris-HCl buffer. Ten microgram plasmid DNA was used and the final volume was set to 2 ml with H_2O. A helium–neon lamp was used as the light source (10 mW) on a Malvern Zetasizer 3000HAs system (Malvern Instruments Ltd, Worcestershire, U.K.). Values were obtained 3 cycles per 10 time measurements.

2.9. Circular Dichroism (CD)

For CD measurement, the chitoplex solutions with weight ratio from 1:0.25 to 1:1.5 (DNA/Polymer) were prepared using ASSP-PEG in terms of the method described above. CD spectra were collected with a 1 cm path length cuvette using J-810 spectropolarimeter in a range of wavelengths of 350–

200 nm at 25°C. The spectra were corrected by subtracting the background of sodium acetate/ acetic acid buffer

2.10. Transmission electron microscopy (TEM)

Transmission electron microscope (TEM) images were recorded using a Hitachi H-600 instrument at 75 kV. For TEM measurements a drop of the polyplex solution in the weight ratio of 1:1 (10 µg in 1 ml of trisbuffer) were deposited directly of Formvar coated copper grid.

3. Results and discussion

The present study was aimed to design and evaluate a novel, potentially safe non-viral gene delivery vector based on the cationic copolymer of spermine and aspartic acid using butylmethylimidazolium hexafluorophosphate ionic liquid as the medium [45]. Vygodskii *et al.* [46] have shown that 1,3-dialkylimidazolium based ionic liquids (IL) are suitable reaction and activating media for the synthesis of high molecular weight polymers, including polyamides. Low temperature solution polycondensation of diamines and diacid chlorides was used for preparing polyamides. The polyamide synthesis was carried out using Boc-aspartic acid and spermine under mild conditions. N-Boc protection was removed by washing the polymer with 50% [v/v] TFA/DCM. As the copolymer (ASSP) was found to be highly hydrophobic and insoluble in many of the organic solvents, it was coupled with PEG, using the same ionic liquid as solvent and 1,1-carbonyl diimidazole as condensing agent (see Figure 1), to make it hydrophilic and water soluble. A commercial PEG polymer with one end capped by a methoxy group was used for this purpose. The polymers thus obtained (BASSP, ASSP and ASSP-PEG) were structurally characterized by means of FTIR spectroscopy (Figure 2). The vanishing of the peak at 645 cm^{-1} and enhanced visibility of the peaks of primary amino group at 3440 cm^{-1} indicate the effective removal of Boc group from BASSP. The strong peaks at 843 cm^{-1} may be due to the N–H deformation vibrations of aliphatic primary amines. The peak at 1596 cm^{-1} is due to the asymmetric NH_3^+ deformation vibration. In addition, the weakening of the carbonyl peaks at 1726 and 1661 cm^{-1} might be due to the coupling of PEG at the acid groups the polymer other than amino group. Therefore, the amino groups are free for undergoing electrostatic interaction between the negatively charged phosphate groups of DNA [47]. We next determined the thermal characteristics of the copolymers using thermogravimetric analysis (TGA) and differential scanning calorimetry (DSC). It can be seen from Table 1 that the polymer ASSP has the lowest thermal stability due possibly to the presence of the chain terminal groups (–COOH and $-NH_2$) in comparison to that of BASS having the thermally stable Boc protecting group. In contrast, ASSP-PEG has stable chain terminal groups ($-OCH_3$) leading to a higher thermal stability. Therefore, the observed differences in the

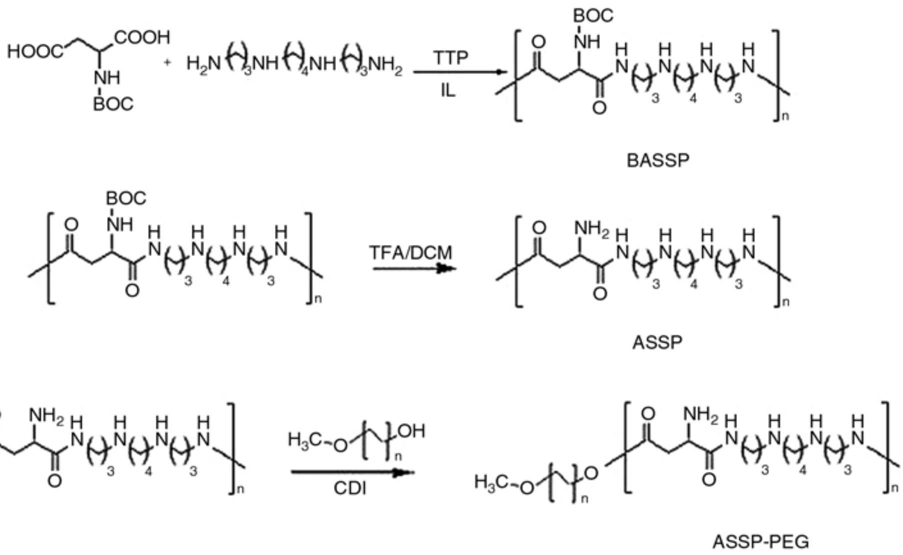

Figure 1. The chemical structure of polymers BASSP, ASSP, ASSP-PEG

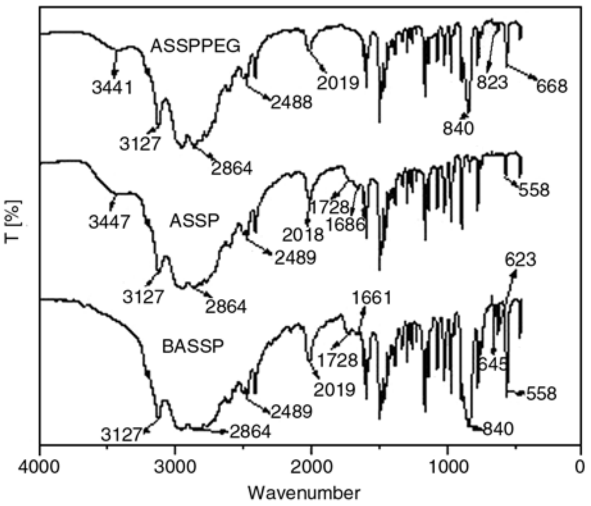

Figure 2. FTIR of polymers

Table-1. TGA and DSC results of the polymers

Polymer	10% wt loss T [°C]	T_g [°C]	ΔH [J/g]
BASSP	276	157	21
ASSP	234	179	21
ASSP-PEG	276	175	21

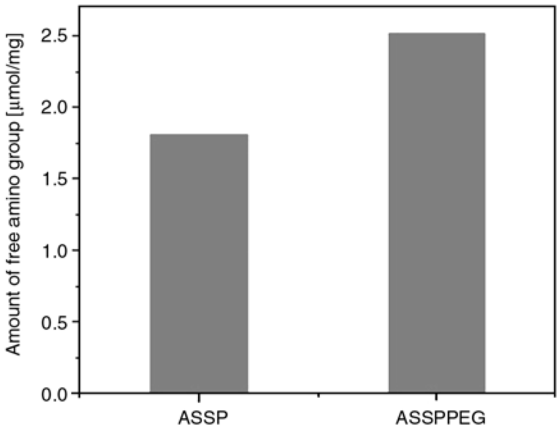

Figure 3. Number of primary amino group in µmol/mg

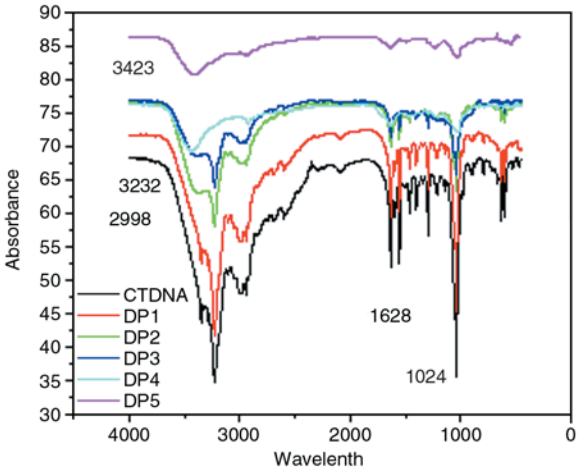

Figure 4. FTIR spectra of ASSP-PEG/CTDNA complexes

thermal stabilities of the synthesized polymer are consistent with their structures. The glass transition temperature and heat of transition of these polymers were determined from DSC data. Table 1 shows that ASSP-PEG exhibited a T_g value between those of ASSP and BASSP.

ASSP-PEG was soluble in water at a concentration of 1 µg/1 µl and the primary amine content was determined using TNBS (Trinitro benzene sulphonic acid) method (Table 2, Figure 3). It was observed that the number of primary amino group of ASSP-PEG was higher than that of ASSP. It may be due to the higher solubility of the polymer in aqueous medium after PEGylation [48]. This result further confirms that the PEG is coupled to the acid end group of the polymer, and not to the amino group. The molecular weight of the polymer was above 10 kDa as obtained from measurements by MALDI TOF MS.

A successful gene carrier is one which can effectively condense negatively charged DNA into nanosized particles [1, 2, 5–7, 47]. The condensation behaviors were studied by using IR spectroscopy, CD spectra, turbidity measurements, particle size analyzer and TEM. The IR spectrum the complex of the copolymer with calf thymus DNA (Figure 4) reveals that as the concentration of polymer increases the intensity of peaks at 1024 cm^{-1} due to P–O–H stretching vibration goes on decreasing and at the charge ratio of P/N = 1.5, the peaks are almost vanished. Similar observation was also found in the case of N–H stretching vibrations of purines and pyrimidines also. It indicates that as the concentration of polymer increases, there are no more negative centers on DNA.

The effect of the condensation of the copolymer with DNA on the secondary structures of DNA was evaluated by CD measurement. It can be seen from Figure 5 that the pure DNA appears in a typical

Table 2. Amount of primary amino group of the polymers

Polymer	Absorbance at 410 nm	Corresponding conc. of spermine	Corresponding no. of moles of spermine	No. of 1° NH_3 group/µl
ASSP	0.1098	91.27	$2.62\cdot10^{-7}$	$1.805\cdot10^{15}$
ASSP-PEG	0.1271	111.59	$3.20\cdot10^{-7}$	$2.510\cdot10^{15}$

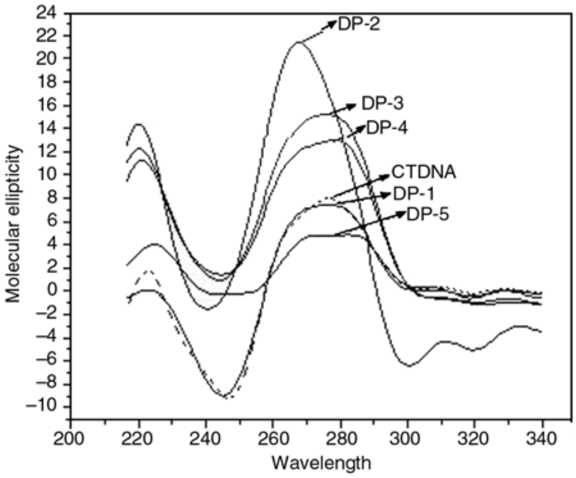

Figure 5. CD spectra of ASSP-PEG/CTDNA complexes

B conformation with approximately equal positive (275 nm) and negative (245 nm) components centered on 258 nm. While plain spermine copolymer does not show any characteristic pattern, its complexes with DNA show changes in the intensity of peaks indicating electrostatic interaction with the negatively charged phosphate groups of DNA [49], but the 'Cotton effect' remains nearly unchanged, demonstrating that DNA remains in B conformation upon complexing with ASSP-PEG polymer.

The dispersive stability of ASSP-PEG polymer –DNA complex was measured using turbidity measurements in which the increase in turbidity indicates self-aggregation. Figure 6 shows that at P/N = 0.5 the turbidity was found to be the least and on increasing the charge ratio of the polymer, turbidity goes on increasing. And at the ratio 1:2 turbidity is found to be decreased without precipitation indicating enhanced stability.

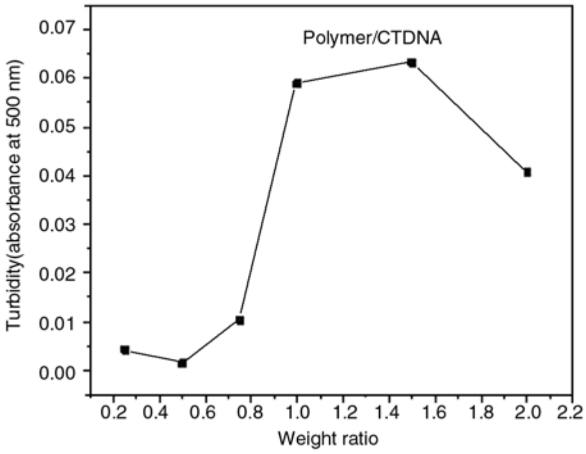

Figure 6. Turbidity curve of CTDNA/ASSP-PEG complexes

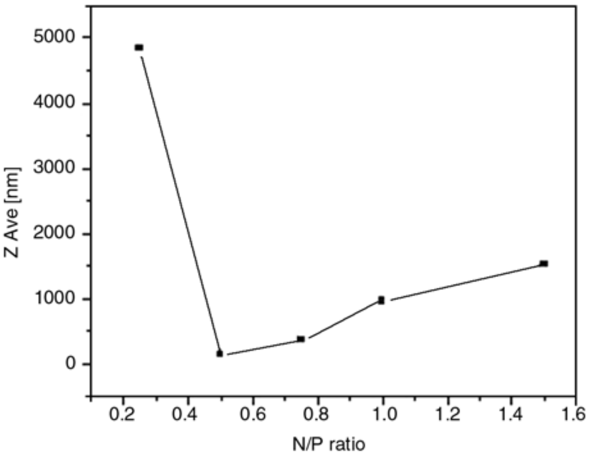

Figure 7. Polyplex sizes as CTDNA/ASSP-PEG complexes

The formation of the nanoparticles was confirmed by measurement of particle size and TEM. The polyplexes were prepared at increasing weight ratios from 1:0.25 to 1:1.5 (DNA/Polymer) in Tris-HCl buffer. Figure 7 shows that the formation of the complex is inversely related to the charge ratio. As the charge ratio increases, the size decrease sharply and becomes a minimum value of 142.5 nm at charge ratio of 0.75 (P/N = 0.75). The charge density and the copolymer structure have remarkable effects on the DNA condensation and size of the nanoparticles that are formed [5].

Figure 8 exhibits TEM the images of the particles of plasmid DNA in the charge ratio of P/N = 1. Toroid like structure with a core-shell arrangement indicates the formation of the DNA-chitosan nanoparticle. The particle size value observed in the TEM micrographs was in the same magnitude as observed by the particle size analyzer. Thus, our

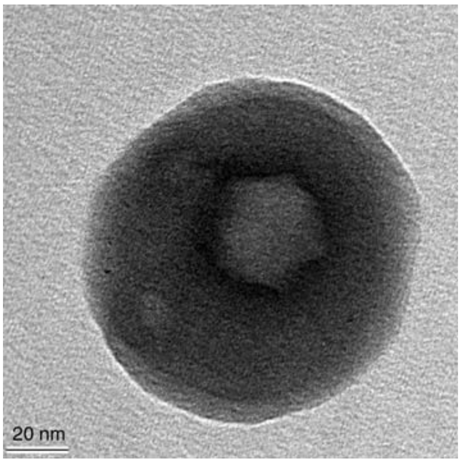

Figure 8. Electron microscope image of PLDNA/ASSP-PEG

data indicate that the copolymer ASSP-PEG condenses with DNA to form nanoparticles in the size range reported for safe transfection. The feasibility in gene transfection by spermine conjugates and derivatives has been established by a number of researchers [40–44, 50, 51]. The copolymerization of spermine with aspartic acid followed by coupling with PEG might be expected to substantially improve the low transfection efficiency of spermine [6]. This strategy also reduces cytotoxicity associated high cationic charge of spermine moieties [5]. The incorporation of PEG in gene vectors in various creative capacities is a widely used strategy for improving the polyplex solubility and reduce polyplex aggregation and prolong the circulation time [2, 5, 7, 12, 28, 48]. Both spermine and aspartic acid, being natural materials are biodegradable and its copolymer with an aliphatic amide bonding is expected to be also biodegradable [50].

4. Conclusions

A novel and convenient method for the synthesis of a potentially safe non-viral gene delivery vehicle based on the cationic block copolymer of spermine and aspartic acid (ASSP) coupled with polyethylene glycol (PEG) was developed. The polycationic ASSP-PEG was found to condense with calf thymus and plasmid deoxyribonuclceic acids (DNAs) in Tris-HCl buffer (pH 7.4) to give a series of block ionomer complexes with various charge ratios. Since DNA condensation to nano/micrometer sized particles are essential for gene delivery, our results indicate a potential use of the copolymer in gene delivery applications.

Acknowledgements

The present study was supported by grants from Department of Science and Technology, Government of India. Research in the Thomas laboratory was supported by a grant from the National Institutes of Health through the National Cancer Institute (CA080163). Thanks are also due to Dr. V. S. Prasad, NIIST, Thiruvananthapuram for the measurement of TEM.

References

[1] Eliyahu H., Barenholz Y., Domb A.: Polymers for DNA delivery. Molecules, **10**, 34–64 (2005).

[2] Jeong J. H., Kim S. W., Park T. G.: Molecular design of functional polymers for gene therapy. Progress in Polymer Science, **32**, 1239–1274 (2007).

[3] Heath W. H., Senyurt A. F., Layman J., Long T. E.: Charged polymers via controlled radical polymerization and their applications for gene delivery. Macromolecular Chemistry and Physics, **208**, 1243–1249 (2007).

[4] Heath F., Haria P., Alexander C.: Varying polymer architecture to deliver drugs. American Association of Pharmaceutical Scientists Journal, **9**, E235–E240 (2007).

[5] Wong S. Y., Pelet J. M., Putnam P.: Polymer systems for gene delivery- Past, present, and future. Progress in Polymer Science, **32**, 799–837 (2007).

[6] Vijayanathan V., Thomas T., Thomas T. J.: DNA nanoparticles and development of DNA delivery vehicles for gene therapy. Biochemistry, **41**, 14086–14094 (2002).

[7] Santhakumaran L. M., Chen A., Pillai C. K. S., Thomas T., He H., Thomas T. J.: Nanotechnology nonviral gene delivery. in 'Nanofabrication Towards Biomedical Applications' (eds.: Kumar C. S. S. R., Hormes J., Leuschner C.) Wiley-VCH, Weinheim 253–287 (2005).

[8] Twaites B., de las Heras Alarcón C., Alexander C.: Synthetic polymers as drugs and therapeutics. Journal of Materials Chemistry, **15**, 441–455 (2005).

[9] Patil S. D., Rhodes D. G., Burgess D. J.: DNA based therapeutics and DNA delivery systems: A comprehensive review. American Association of Pharmaceutical Scientists Journal, **7**, E61–E77 (2005).

[10] Friedmann T., Rossi J.: Gene transfer: Delivery and expression of DNA and RNA, A laboratory manual. Cold Spring Harbor Laboratory Press, Woodbury (2007).

[11] Pasut G., Veronese F. M.: Polymer-drug conjugation, recent achievements and general strategies. Progress in Polymer Science, **32**, 933–961 (2007).

[12] Kommareddy S., Sandip M. S., Tiwari B., Amiji M. M.: Long-circulating polymeric nanovectors for tumor-selective gene delivery. Technology in Cancer Research and Treatment, **4**, 615–625 (2005).

[13] Pack D. W., Hoffman A. S., Pun S., Stayton P. S.: Design and development of polymers for gene delivery. Nature Reviews, Drug Discovery, **4**, 581–593 (2005).

[14] Conwell C. C., Huang L.: Recent advances in nonviral gene delivery. Advances in Genetics, **53**, 1–18 (2005).

[15] De Laporte L., Cruz Rea J., Shea L. D.: Design of modular non-viral gene therapy vectors. Biomaterials, **27**, 947–954 (2006).

[16] Putnam D.: Polymers for gene delivery across length scales. Nature Materials, **5**, 439–451 (2006).

[17] Filipcsei G.: Smart polymers for biomedical application and environmental protection. Express Polymer Letters, **2**, 77 (2008).

[18] Oh K. T., Yin H., Lee E. S., Bae Y. H.: Polymeric nanovehicles for anticancer drugs with triggering release mechanisms. Journal of Materials Chemistry, **17**, 3987–4001 (2007).

[19] Glover D. J., Lipps H. J., Jans D. A.: Towards safe, non-viral therapeutic gene expression in humans. Nature Reviews, Genetics, **6**, 299–310 (2006).

[20] Kim T-H., Jiang H-L., Jere D., Park I-K., Cho M-H., Nah J-W., Choi Y-J., Akaike T., Cho C-S.: Chemical modification of chitosan as a gene carrier in vitro and in vivo. Progress in Polymer Science, **32**, 726–753 (2007).

[21] Lee K. Y.: Chitosan and its derivatives for gene delivery. Macromolecular Research, **15**, 195–201 (2007).

[22] Kasyanenko N., Afanasieva D., Dribinsky B., Mukhin D., Nazarova O., Panarin E.: DNA interaction with synthetic polymers in solution. Structural Chemistry, **8**, 519–525 (2007).

[23] Jiang X., Dai H., Leong K. W., Goh S-H., Mao H-Q., Yang Y-Y.: Chitosan-g-PEG/DNA complexes deliver gene to the rat liver via intrabiliary and intraportal infusions. Journal of Gene Medicine, **8**, 477–487 (2006).

[24] Wu C., Hao J., Deng X., Liu Y. L.: A novel potential cationic polymeric gene vector containing hydroxy groups and all grades of amino groups. Journal of Applied Polymer Science, **105**, 1533–1542 (2007).

[25] Kataoka K., Togawa H., Harada A., Yasugi K., Matsumoto T., Katayose S.: Spontaneous formation of polyion complex micelles with narrow distribution from antisense oligonucleotide and cationic block copolymer in physiological saline. Macromolecules, **29**, 8556–8557 (1996).

[26] Bronich T. K., Nguen H. K., Eisenberg A., Kabanov A. V.: Recognition of DNA topology in reactions between plasmid DNA and cationic copolymers. Journal of American Chemical Society, **122**, 8339–8343 (2000).

[27] Cohen Stuart M. A., Besseling N. A. M., Fokkink R. G.: Formation of micelles with complex coacervate cores. Langmuir, **14**, 6846–6849 (1998).

[28] Harada A., Kataoka K.: Formation of polyion complex micelles in an aqueous milieu from a pair of oppositely-charged block copolymers with poly(ethylene glycol) segments. Macromolecules, **28**, 5294–5299 (1995).

[29] Gohy J-F., Varshney S. K., Jérôme R.: Morphology of water-soluble interpolyelectrolyte complexes formed by poly(2-vinylpyridinium)-block-poly(ethylene oxide) diblocks and poly(4-styrenesulfonate) polyanions. Macromolecules, **34**, 2745–2747 (2001).

[30] Kabanov A. V., Vinogradov V. V., Suzdaltseva Y. G., Valery Y. A.: Water-soluble block polycations as carriers for oligonucleotide delivery. Bioconjugate Chemistry, **6**, 639–643 (1995).

[31] Jiang H-L., Kim Y-K., Arote R., Nah J-W., Cho M-H., Choi Y-J., Akaike T., Cho C-S.: Chitosan-graft-polyethylenimine as a gene carrier. Journal of Controlled Release, **117**, 273–280 (2007).

[32] Cutrona G., Boffa L. C., Mariani M. R., Matis S., Damonte G., Millo E., Roncella S., Ferrarini M.: The peptide nucleic acid targeted to a regulatory sequence of the translocated c-myc oncogene in burkitt's lymphoma lacks immunogenicity: Follow-up characterization of PNAEμ-NLS. Oligonucleotides, **17**, 146–150 (2007).

[33] Yang C., Li H., Goh S. H., Li J.: Cationic star polymers consisting of α-cyclodextrin core and oligoethylenimine arms as nonviral gene delivery vectors. Biomaterials, **28**, 3245–3254 (2007).

[34] Vijayanathan V., Lyall J., Thomas T., Shirahata A., Thomas T. J.: Ionic, structural and temperature effects on DNA nanoparticles formed by natural and synthetic polyamines. Biomacromolecules, **6**, 1097–1103 (2005).

[35] Vijayanathan V., Thomas T., Thomas A., Shirahata A., Thomas, T. J.: Formation of DNA nanoparticles in the presence of novel polyamine analogues: A laser light scattering and atomic force microscopic study. Nucleic Acids Research, **32**, 127–134 (2004).

[36] Saminathan M., Thomas T., Shirahata A., Pillai C. K. S., Thomas T. J.: Polyamine structural effects on the induction and stabilization of liquid crystalline DNA: Potential applications to DNA packaging, gene therapy and polyamine therapeutics. Nucleic Acids Research, **30**, 3722–3731 (2002).

[37] Zimmerman S. B., Murphy L. D.: Macromolecular crowding and the mandatory condensation of DNA in bacteria. FEBS Letters, **390**, 245–248 (1996).

[38] Cheng S. H., Scheule R. K.: Airway delivery of cationic lipid: DNA complexes for cystic fibrosis. Advances in Drug Delivery Review, **30**, 173–184 (1998).

[39] Boussif O., Lezoualc'h F., Zanta M. A., Mergny M. D., Scherman D., Demeneix B., Behr J.: A versatile vector for gene and oligonucleotide transfer into cells in culture and in-vivo: Polyethylenimine. Proceedings of National Academy of Sciences of United States of America, **92**, 7297–7301 (1995).

[40] Jere D., Kim D-H., Arote R., Jiang H-L., Cho M-H., Nah J. W., Cho C-S.: A poly(β-amino ester) of spermine and poly(ethylene glycol) diacrylate as a gene carrier. Key Engineering Materials, **342**, 425–428 (2007).

[41] Vinogradov S. V., Bronich T. K., Kabanov A. V.: Self-assembly of polyamine-poly(ethylene glycol) copolymers with phosphorothioate oligonucleotides. Bioconjugate Chemistry, **9**, 805–812 (1998).

[42] Azzam T., Eliyahu H., Makovitzki A., Linial M., Domb A. J.: Hydrophobized dextran-spermine conjugate as potential vector for in vitro gene transfection. Journal of Controlled Release, **96**, 309–323 (2004).

[43] Eliyahu H., Joseph A., Schillemans J. P., Azzam T., Domb A. J., Barenholz Y.: Characterization and in vivo performance of dextran-spermine polyplexes and DOTAP/cholesterol lipoplexes administered locally and systemically. Biomaterials, **28**, 2339–2349 (2007).

[44] Kanatani I., Ikai T., Okazaki A., Jo J., Yamamoto M., Imamura M., Kanematsu A., Yamamoto S., Ito N., Ogawa O., Tabata Y.: Efficient gene transfer by pullulan-spermine occurs through both clathrin- and raft/caveolae-dependent mechanisms. Journal of Controlled Release, **116**, 75–82 (2006).

[45] Huddleston J. G., Willauer H. D., Swatloski R. P., Visser A. E., Rogers R. D.: Room temperature ionic liquids as novel media for 'clean' liquid-liquid extraction. Chemical Communications, **16**, 1765–1766 (1998).

[46] Vygodskii Y. S., Lozinskaya E. I., Shaplov A. S.: Ionic liquids as novel reaction media for the synthesis of condensation polymers. Macromolecular Rapid Communications, **23**, 676–680 (2002).

[47] Bloomfield V. A.: DNA condensation by multivalent cations. Biopolymers, **44**, 269–282 (1997).

[48] Glodde M., Sirsi S. R., Lutz G. J.: Physiochemical properties of low and high molecular weight poly(ethylene glycol)-grafted poly(ethylene imine) copolymers and their complexes with oligonucleotides. Biomacromolecules, **7**, 347–56 (2006).

[49] Sánchez-Carrasco, S., Delcros J. G., Moya-García A. A., Sánchez-Jiménez F., Ramírez, F. J.: Study by optical spectroscopy and molecular dynamics of the interaction of acridine-spermine conjugate with DNA. Biophysical Chemistry, **133**, 54–65 (2008).

[50] Hosseinkhani H., Azzam T., Tabata Y., Domb A. J.: Dextran-spermine polycation: An efficient nonviral vector for in vitro and in vivo gene transfection. Gene Therapy, **11**, 194–203 (2004).

[51] Jo J-I., Ikai T., Okazaki A., Nagane K., Yamamoto M., Hirano Y., Tabata Y.: Expression profile of plasmid DNA obtained using spermine derivatives of pullulan with different molecular weights. Journal of Biomaterials Science, Polymer Edition, **18**, 883–899 (2007).

eXPRESS Polymer Letters Vol.2, No.5 (2008) 339–348
Available online at www.expresspolymlett.com
DOI: 10.3144/expresspolymlett.2008.40

Effect of polyethersulfone and *N*,*N*′-bismaleimido-4,4′-diphenyl methane on the mechanical and thermal properties of epoxy systems

R. Rajasekaran[1], *M. Alagar*[2*], *C. Karikal Chozhan*[2]

[1]Department of Chemistry, St. Joseph's College of Engineering, Chennai – 600 119, India
[2]Department of Chemical Engineering, Anna University, Chennai – 600 025, India

Received 12 February 2008; accepted in revised form 22 March 2008

Abstract. In order to improve thermo mechanical properties of cured epoxy resin, hydroxyl terminated polyethersulfone (PES) and *N,N*′-bismaleimido-4,4′-diphenyl methane (BMI) were incorporated to diglycidyl ether of bisphenol A (DGEBA) type epoxy resin and cured with diaminiodiphenylmethane (DDM). The resulting hybrid matrices, in the form of castings, were characterized for their mechanical properties like tensile, flexural and impact strength. Differential scanning calorimetry, dynamic mechanical analysis and thermogravimetric analysis of the matrices were also performed to determine the glass transition temperature and thermal stability of the matrix systems. The results obtained from mechanical and thermal studies indicated that the incorporation of polyethersulfone into epoxy resin improved the toughness and thermal stability of the systems. This is attributed to the formation of interpenetration polymer networks (IPNs) composed of the epoxy network and the linear PES. The incorporation of BMI into polyethersulfone modified epoxy systems increased thermal stability, glass transition temperature, tensile and flexural properties and decreased the impact strength. Scanning electron microscopy studies of polyethersulfone modified epoxy and BMI incorporated polyethersulfone modified epoxy systems exhibit homogeneous morphology confirming efficient chemical interaction and formation of intercrosslinked network structure.

Keywords: *polymer composites, thermal properties, mechanical properties, morphology, moisture absorption*

1. Introduction

Epoxy resin systems are widely used for many important applications such as adhesives, encapsulating resins and as matrices in advanced structure composites in aerospace industry. Besides their adhesive properties, these highly cross linked networks posses excellent thermal and chemical stability as well as high modulus and strength [1–6]. However, the further use of epoxies is limited because of their inherent brittleness, poor crack resistance. In recent years, the feasibility of toughening highly crosslinked networks with high modulus and high T_g thermoplastics has been investigated [7–12]. Addition of thermoplastics into thermosets leads to different phenomena. The initial mixture is generally homogeneous and phase separation could take place during curing of the thermoset. This technique is called reaction induced phase separation [13–15]. But, morphologies are controlled by many factors, such as the miscibility, modifier concentration, curing temperature and reaction rate [10, 16]. Several attempts have been made to dissolve the thermoplastics in the epoxy resin homogeneously [17–18]. The IPN or semi-IPN technique is one of the effective modifications of epoxy resin which makes it possible to attain

---

[*]Corresponding author, e-mail: mkalagar@yahoo.com

homogeneous hybrid thermoplastic modified epoxy with low fractions of thermoplastics [18]. It is reported that the incorporation of high performance thermoplastics into a thermoset resin system leads to significant improvements in mechanical properties [9, 19–22].

In our laboratory, epoxy resin has been modified using different polymeric and chemical modifiers namely hydroxyl terminated polydimethylsiloxane [23], γ-aminopropyltriethoxysilane [24], unsaturated polyester [25], vinylester [26], bismaleimides, polyuretanes [27] and the results obtained have been published elsewhere.

The introduction of bismaleimide into epoxy resin improves the thermomechanical properties of epoxy resin [28–32]. Bismaleimides posses high crosslinking ability, high glass-transition temperature, high thermal ability, high char yield, excellent fire resistance, superior specific strength and specific modulus, and low water absorption. In continuation of our earlier studies, an attempt has been made in the present investigation to improve both toughness and thermo-mechanical properties of epoxy resin by incorporating hydroxyl terminated polyethersulfone (PES) and *N,N′*-bismaleimido-4,4′-diphenyl methane(BMI).

2. Materials and methods

Epoxy resin [diglycidyl ether of bisphenol A (DGEBA)] LY556 (epoxy equivalent 189 and viscosity 10 000 cP) and 4,4′-diaminodiphenylmethane (DDM) were obtained from Ciba-Geigy (India). *N,N′*-bismaleimido-4,4′-diphenyl methane was synthesized in our laboratory as per the reported procedure (Figure 1) [33]. Hydroxyl terminated polyethersulfone was supplied by Jilin University, China was used as received. The chemical structures of materials used are presented in Figure 2.

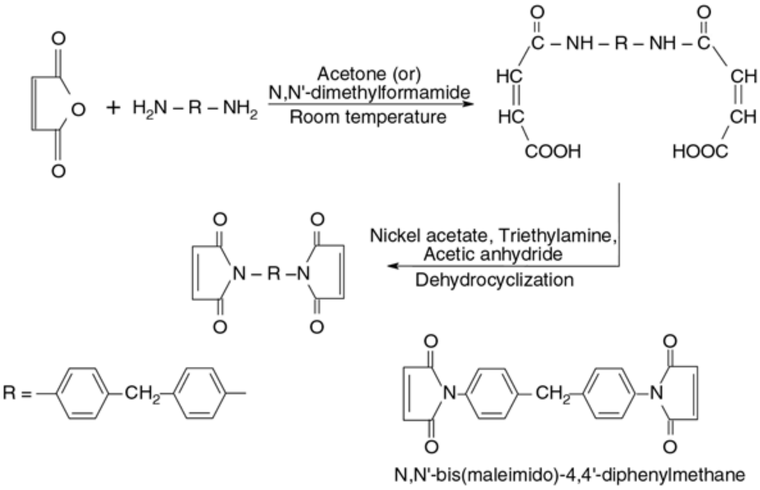

Figure 1. Synthesis of bismaleimide

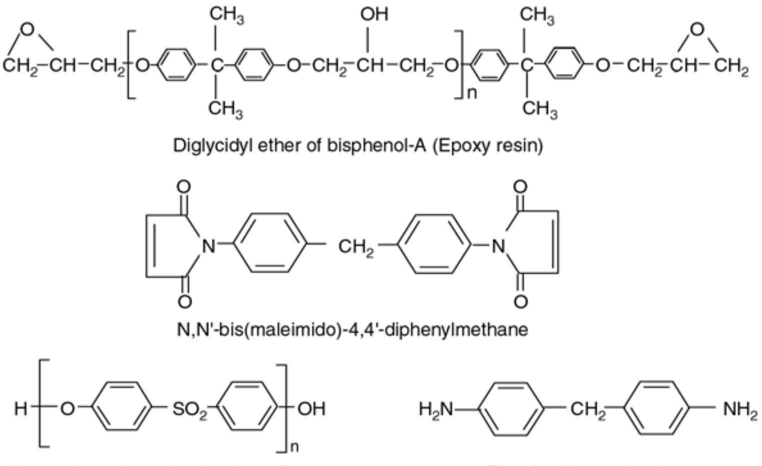

Figure 2. Chemical structure of monomers and of oligomer epoxy resin

2.1. Preparation of epoxy polyethersulfone/bismaleimide hybrid

The hybrid polyethersulfone epoxy matrices were prepared by dissolving varying percentages (4, 8, 12% by wt) of hydroxyl terminated polyethersulfone and tetramethyl ammonium hydroxide (TMAH) in known amount (100% by wt) of epoxy resin with continuous stirring at 150° C for two hours. The blend obtained was degassed under vaccum for half an hour and then cooled to 100°C. Then, calculated amount of bismaleimide was dissolved into polyethersulfone-epoxy blend at 100°C under vigorous stirring. The stoichiometric amount of 4,4′-diaminodiphenylmethane (with respect to epoxy) was added. The agitation was continued at 100° C until a homogeneous product was obtained. The product was subjected to vacuum to remove the trapped air and then cast and cured at 120°C for 3 hours. The castings were then post cured at 180°C for 2 hours and finally removed from the mould and characterized.

2.2. Test methods

The IR spectra for unmodified epoxy, polyethersulfone modified epoxy and bismaleimide incorporated polyethersulfone modified epoxy matrices were recorded on a Perkin-Elmer (Model RX1) FT-IR spectrometer. Glass transition temperature (T_g) of the samples was determined using NETZSCH DSC 200PC analyzer (TA instruments USA) in the temperature range between 50 and 250°C at a heating rate of 10°C per minute in nitrogen atmosphere. Dynamic mechanical analysis of the samples was measured by using NETZSCH DMA 242 dynamic mechanical analyzer having dynamic strain of 0.3 and frequency of 1 Hz. Thermogravimetric analysis (TGA) was carried out using NETZSCH STA 409PCanalyzer (TA instruments USA) at a heating rate of 10°C per minute in air. The heat deflection temperature (HDT) of the samples was tested as per ASTM D 648-72.

The tensile strength was determined using dog bone-shaped specimens according to ASTM-D3039, using an Instron testing machine (Model 6025; Instron, UK), at a crosshead speed of 10 mm/minute. The flexural properties were measured as per ASTM D 790, using an Instron testing machine (Model 6025 UK), at 10 mm/minute cross head speed. The Izod impact strength of the neat resin castings was evaluated as per ASTM D-256. As many as five test pieces were used to generate the data points for the mechanical tests.

Scanning electron microscopy (SEM) JEOL JSM (Model 6360) was used to investigate the morphology of unmodified epoxy, polyethersulfone modified epoxy and bismaleimide incorporated polyethersulfone modified epoxy matrix systems. The water absorption property of the samples was determined as per ASTM D 570. The results obtained are presented in Tables 1, 2 and Figures 2–10.

3. Results and discussion

3.1. IR spectroscopy

The formation of interpenetrating network of epoxy and polyethersulfone proceeds through the reaction between hydroxyl terminated polyethersulfone oligomer and large molar excess of epoxy resin in the presence of tetramethyl ammonium hydroxide (Figure 3). The large excess of epoxy resin was used to endcap the polyethersulfone oligomers which essentially prevents the further polymerization. The disappearance of IR absorption for oxirane ring of epoxy at 914 cm^{-1} was used to ascertain the completion of the reaction (Figure 4). The intensity of IR absorption peaks observed for oxirane ring of epoxy (Figure 4a) was very high at the initial stage of the reaction. The decrease in intensity of the peak for oxirane ring of epoxy confirms the reaction between epoxy and hydroxyl group of polyethersulfone (20%). The IR absorption peak of epoxy disappeared completely after the completion of the reaction between polyethersulfone modified epoxy and the curing agent, (DDM) (Figure 4d) which confirms the formation of interpenetrating polymer network structure (IPN).

3.2. Mechanical properties

The values of tensile properties observed for epoxy resin and epoxy systems modified with polyethersulfone and bismaleimide (BMI) are presented in Table 1. The introduction of 4, 8 and 12% polyethersulfone (by weight) into epoxy resin increased the tensile strength by marginal extent when compared with unmodified epoxy resin due to inherent rigid aromatic molecular structure of polyethersulfone which influences the enhancement of both tensile strength and modulus. The incorporation of 4, 8

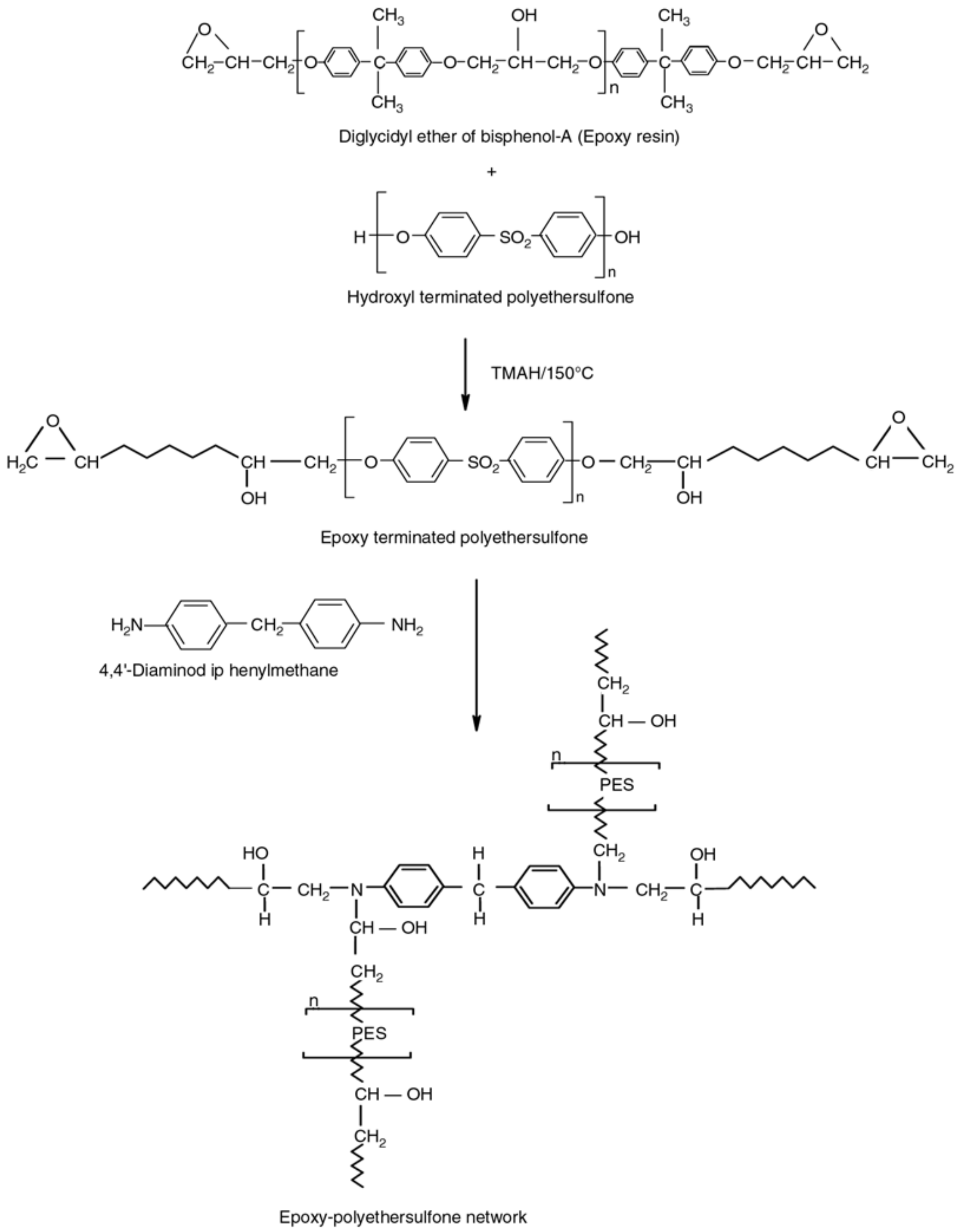

Figure 3. Formation of polyethersulfone modified epoxy-DDM interpenetrating polymer network (IPN)

and 12% BMI (by weight) into the epoxy resin increased the tensile strength by 7.5, 20.9 and 38.1% respectively (Table 1). This may be explained by the formation of intercrosslinking network between epoxy and BMI, which in turn increased crosslinking density. Similarly, the introduction of both BMI and polyethersulfone into epoxy resin increased the value of tensile strength according to their percentage content. The tensile strength values of polyethersulfone-epoxy system increased with increasing BMI content. The values of tensile modulus obtained for the unmodified epoxy and epoxy modified with polyethersulfone, bismaleimide and combinations of both are presented in Table 1 and exhibited a similar trend to that of tensile strength.

The data observed for the flexural behaviour of epoxy resin and epoxy systems modified with polyethersulfone and bismaleimide are presented in Table 1. The introduction of 4, 8 and 12% polyethersulfone into epoxy resin increased the flexural strength slightly when compared to unmodified epoxy resin which is attributed to the formation of interpenetrating polymer networks (IPN) composed

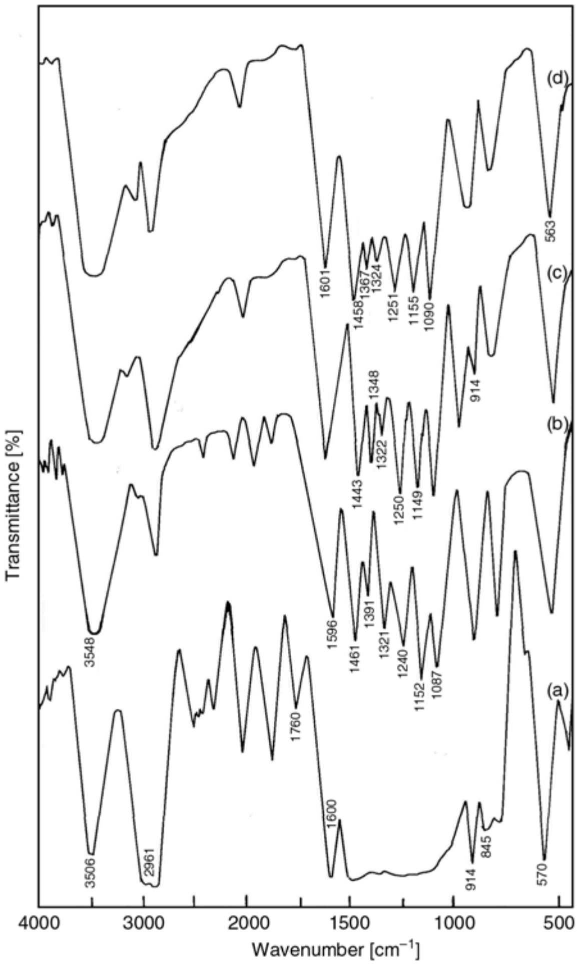

Figure 4. FTIR spectra of (a) unmodified epoxy resin, (b) polyethersulfone, (c) DDM-cured epoxy-polyethersulfone (100:20) cured at 140°C for 3 hours and postcured at 200°C for 2 hour

of the epoxy networks and linear PES. The high modulus in the rubbery region can be interpreted on the network interlock of the epoxy matrix and PES. The incorporation of 4, 8 and 12% BMI into the epoxy resin increased the flexural strength by 7.2, 19.9 and 27% respectively (Table 1). This may be explained by the occurrence of homopolymerization of bismaleimide and the formation of inter-crosslinking network structure between epoxy and bismaleimides [32, 34–35]. Similarly, the values of flexural strength of polyethersulfone modified epoxy increased with increasing BMI content. The values of flexural modulus of polyethersulfone modified epoxy bismaleimide systems also follow the similar trend to that of flexural strength.

The values of unnotched Izod impact strength obtained for unmodified epoxy resin and epoxy modified with polyethersulfone, bismaleimide, and a combination of both are presented in Table 1. It can be concluded that the increase in the impact strength is attributed to the increase in the ductility of the modified resin by the formation of the IPN structure. Whereas the incorporation of bismaleimide into epoxy decreased the impact strength behavior as a result of an intercrosslinked network formation, which in turn enhanced the rigidity and crosslinking density. The incorporation of bismaleimide in both the cases of epoxy and polyethersulfone modified epoxy systems decreased the unnotched Izod impact strength according to their percentage content.

Table 1. Mechanical properties of unmodified epoxy, polyethersulfone modified epoxy, BMI modified epoxy and BMI modified polyethersulfone-epoxy systems

Sample code	Tensile strength [MPa]	Tensile modulus [MPa]	Flexural strength [MPa]	Flexural modulus [MPa]	Impact strength [J/m]
E$_{100}$ PES$_0$ BMI$_0$	63.2 ± 5	2751.7 ± 28	110.0 ± 7	1812.9 ± 28	100.3 ± 5
E$_{100}$ PES$_4$ BMI$_0$	63.5 ± 3	2773.1 ± 25	111.0 ± 6	1827.1 ± 25	130.3 ± 6
E$_{100}$ PES$_8$ BMI$_0$	64.0 ± 4	2798.5 ± 26	112.6 ± 5	1855.8 ± 24	142.4 ± 5
E$_{100}$ PES$_{12}$ BMI$_0$	64.9 ± 6	2815.9 ± 28	113.2 ± 6	1874.0 ± 28	168.1 ± 6
E$_{100}$ PES$_4$ BMI$_4$	65.7 ± 5	2795.7 ± 20	113.2 ± 5	1863.2 ± 29	126.4 ± 5
E$_{100}$ PES$_4$ BMI$_8$	67.1 ± 4	2861.0 ± 24	115.0 ± 4	1947.6 ± 31	120.3 ± 4
E$_{100}$ PES$_4$ BMI$_{12}$	69.2 ± 3	2925.3 ± 29	117.9 ± 6	1974.5 ± 30	114.3 ± 6
E$_{100}$ PES$_8$ BMI$_4$	65.5 ± 3	2816.5 ± 25	114.3 ± 5	1892.5 ± 29	134.3 ± 4
E$_{100}$ PES$_8$ BMI$_8$	67.6 ± 4	2871.3 ± 26	116.8 ± 3	1922.2 ± 28	128.4 ± 6
E$_{100}$ PES$_8$ BMI$_{12}$	69.8 ± 5	2926.3 ± 30	118.9 ± 5	1947.8 ± 25	120.4 ± 7
E$_{100}$ PES$_{12}$ BMI$_4$	65.5 ± 4	2854.5 ± 21	115.5 ± 4	1909.3 ± 31	161.8 ± 5
E$_{100}$ PES$_{12}$ BMI$_8$	68.8 ± 6	2918.2 ± 26	117.1 ± 6	1946.4 ± 32	153.8 ± 5
E$_{100}$ PES$_{12}$ BMI$_{12}$	71.0 ± 5	2981.6 ± 28	119.4 ± 5	1998.2 ± 29	144.4 ± 6
E$_{100}$ PES$_0$ BMI$_4$	65.8 ± 4	2820.4 ± 30	118.3 ± 5	2040.5 ± 26	93.1 ± 5
E$_{100}$ PES$_0$ BMI$_8$	74.0 ± 2	2876.3 ± 29	127.3 ± 6	2275.9 ± 27	91.3 ± 4
E$_{100}$ PES$_0$ BMI$_{12}$	84.5 ± 3	3053.9 ± 25	132.6 ± 7	2596.8 ± 30	87.9 ± 3

E – epoxy; PES – hydroxyl terminated polyethersulfone; BMI – bismaleimide

3.3. Thermal properties

DSC thermograms of unmodified epoxy, and epoxy systems modified with polyethersulfone and BMI are presented in Figures 5 and 6. The polyethersulfone modified epoxy hybrids exhibit transparent behaviour at ambient temperature and there was no evidence of phase separation noticed. Further the single value of T_g observed for polyethersulfone modified epoxy suggested that the hybrid is chemically bonded homogeneous products of amorphous nature. The value of the glass transition temperature of the epoxy system modified with polyethersulfone was some what lower than that of unmodified epoxy resin. The incorporation of polyethersulfone raised the viscosity of the resulting hybrid epoxy system, which could result in an incomplete curing reaction due to the steric hindrance under the curing conditions [36]. The thickening effect and consequent chain lengthening of polyethersulfone skeleton lead to the reduction of the crosslinking density and hence molecular flexibility occurs at low temperature. The incorporation of BMI into both epoxy resin and polyethersulfone modified epoxy systems enhanced the T_g values (Table 2). An enhancement in the values of T_g is due to the occurrence of homopolymerisation of bismaleimides rather than to Michael addition reaction and is confirmed from our earlier studies [24]. Since Michael addition reaction reduced the crosslink density due to chain extension.

The data resulted from dynamic mechanical analysis for unmodified epoxy and epoxy modified with polyethersulfone and BMI are given in Figure 7. A single tanδ peak was observed for polyethersulfone modified epoxy hybrid. The glass transition temperature of polyethersulfone modified epoxy decreased when compared with that value of unmodified epoxy resin. However, the incorpora-

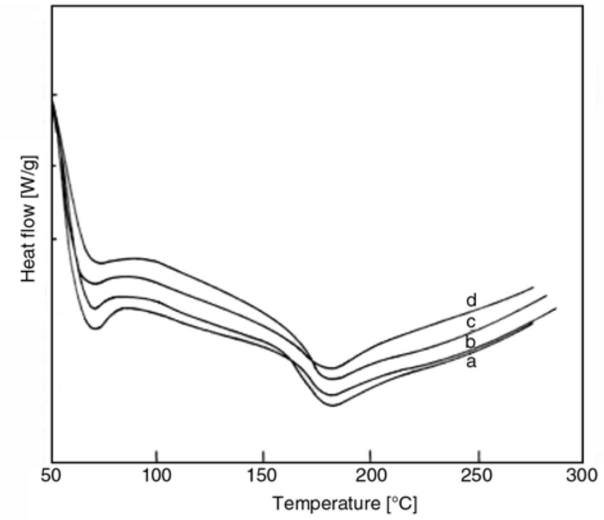

Figure 5. DSC traces of polyethersulfone modified epoxy systems (a) unmodified epoxy, (b) 4% PES modified epoxy, (c) 8% PES modified epoxy and (d) 12% PES modified epoxy

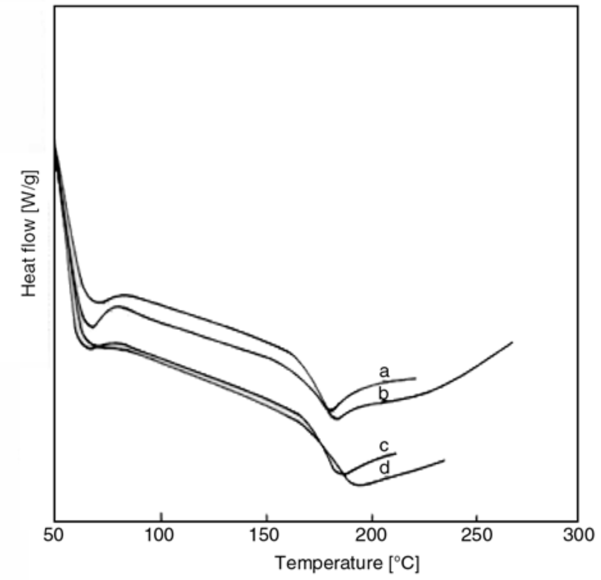

Figure 6. DSC traces of BMI modified polyethersulfone-epoxy systems (a) 4%, (b) 8% and (c) 12% BMI modified polyethersulfone (8%)-epoxy systems

Table 2. Percentage water absorption, glass transition temperature percentage weight loss and heat distortion temperature of unmodified epoxy, polyethersulfone modified epoxy, BMI modified epoxy and BMI modified polyethersulfone-epoxy systems

Sample code	Water absorption [%]	Heat deflection temperature [°C]	Glass transition temperature [°C]
E$_{100}$ PES$_0$ BMI$_0$	0.1201	153	165
E$_{100}$ PES$_4$ BMI$_0$	0.1182	152	164
E$_{100}$ PES$_8$ BMI$_0$	0.1123	151	162
E$_{100}$ PES$_{12}$ BMI$_0$	0.1085	151	161
E$_{100}$ PES$_4$ BMI$_4$	0.1131	153	166
E$_{100}$ PES$_4$ BMI$_8$	0.1076	156	169
E$_{100}$ PES$_4$ BMI$_{12}$	0.1024	158	171
E$_{100}$ PES$_8$ BMI$_4$	0.1095	152	163
E$_{100}$ PES$_8$ BMI$_8$	0.1031	154	167
E$_{100}$ PES$_8$ BMI$_{12}$	0.0977	157	179
E$_{100}$ PES$_{12}$ BMI$_4$	0.1019	152	162
E$_{100}$ PES$_{12}$ BMI$_8$	0.0942	153	165
E$_{100}$ PES$_{12}$ BMI$_{12}$	0.0893	156	168
E$_{100}$ PES$_0$ BMI$_4$	0.0853	154	167
E$_{100}$ PES$_0$ BMI$_8$	0.0781	156	172
E$_{100}$ PES$_0$ BMI$_{12}$	0.0693	159	180

E – epoxy; PES – hydroxyl terminated polyethersulfone; BMI – bismaleimide

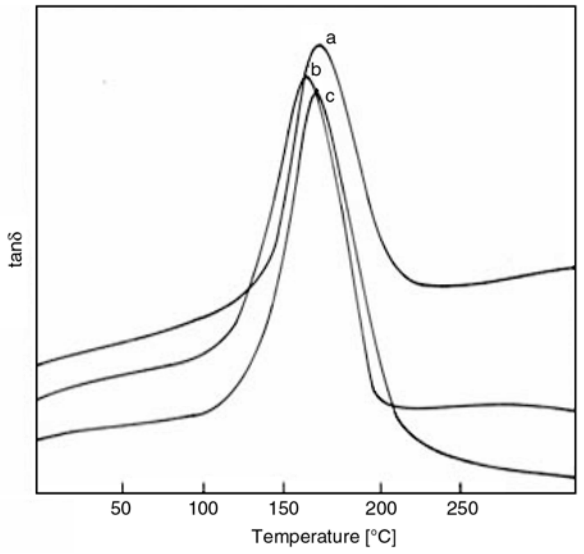

Figure 7. Variation of tanδ as a function of temperature (a) unmodified epoxy, (b) polyethersulfone modified epoxy and (c) BMI modified polyethersulfone-epoxy systems

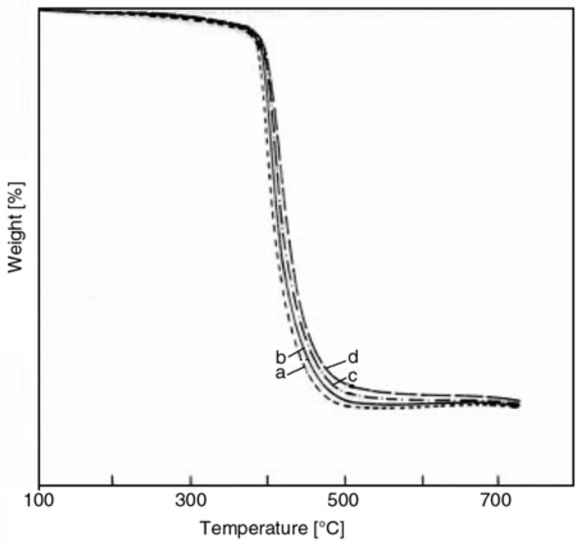

Figure 8. TGA curves of epoxy and polyethersulfone-epoxy systems (a) unmodified epoxy, (b) 4%, (c) 8% and (d) 12% PES-epoxy systems

tion of BMI into both epoxy resin and polyethersulfone modified epoxy systems enhanced the T_g values according to the percentage content. The DMA results obtained are in good agreement with those obtained from DSC studies.

Heat distortion temperature values for epoxy, polyethersulfone modified epoxy, BMI modified epoxy and BMI modified polyethersulfone-epoxy systems are presented in Table 2. From Table 2 it is evident that the values of HDT were decreased with increasing polyethersulfone concentration whereas the reverse trend in HDT values are observed for BMI modified epoxy and BMI modified polyethersulfone-epoxy systems. The enhancement in the values of HDT for bismaleimide modified systems is due to the rigidity and improved crosslink density imparted by heterocyclic bismaleimide.

Polyethersulfone incorporation into epoxy resin improved thermal stability and enhanced the degradation temperature compared to the unmodified epoxy resin according to its percentage concentration (Figure 8). The presence of polyethersulfone skeleton in the epoxy system delays the degradation process and high thermal energy is required to attain the same percentage weight loss than that required for unmodified epoxy system. The delay in degradation caused by the addition of polyethersulfone with a high T_g increased the viscosity of the system and in turn induced the formation of interpenetrating polymer network (IPN) within the system. The thermal degradation temperature of the BMI modified epoxy systems and BMI modified polyethersulfone epoxy systems were found to be increased with increasing bismaleimide concentration. It is evident from Figure 9 that the degradation temperature was increased with increasing BMI concentrations as observed in the case of polyethersulfone modified systems and this may be due to the rigidity and enhanced crosslink density imparted by bismaleimide.

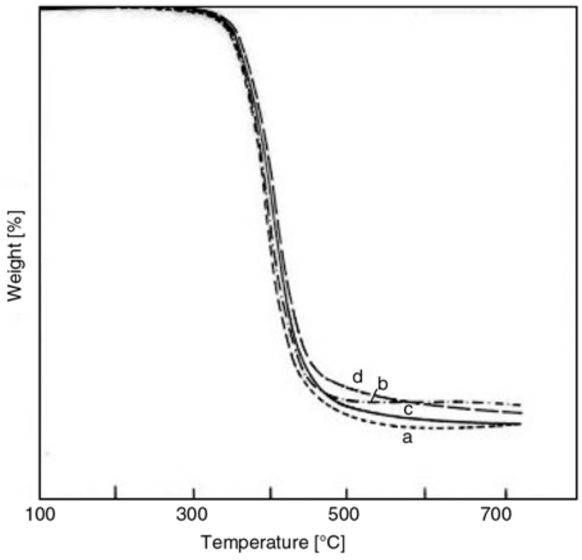

Figure 9. TGA curves of BMI modified polyethersulfone-epoxy systems (a) 4%, (b) 8% and (c) 12% BMI modified PES (8%)-epoxy systems

3.4. Morphology

The scanning electron micrographs of fractured surfaces of the unmodified epoxy, polyethersulfone modified epoxy and polyethersulfone modified bismaleimide incorporated epoxy systems revealed smooth and homogeneous microstructures (Figures 10a–d). This confirmed that the hybrid product is having single chemical entity. Further this observation supports the results obtained from DMA and DSC analysis. The efficient interaction between polyethersulfone and epoxy resin and consequent IPN formation may be the cause for the development of homogeneous morphology.

3.5. Water absorption behavior

The polyethersulfone incorporation into epoxy system and the incorporation of BMI into both epoxy resin and polyethersulfone modified epoxy systems decreased the water absorption behavior, due to the hydrophobic behaviour imparted by polyethersulfone and enhanced cross linking density coupled with water repellency induced by bismaleimide (Table 2).

4. Conclusions

The polyethersulfone modified epoxy, BMI modified epoxy and BMI modified polyethersulfone-epoxy intercrosslinked network having varied concentrations of BMI and polyethersulfone were prepared. The decreased thermal properties such as T_g, HDT were observed for polyethersulfone modified epoxy systems due to chain lengthening and consequent reduction in crosslink density induced by polyethersulfone skeleton. The values of mechanical properties indicated that the incorporation of polyethersulfone into epoxy resin improved tensile strength, flexural strength and fracture toughness and the incorporation of bismaleimide also increased

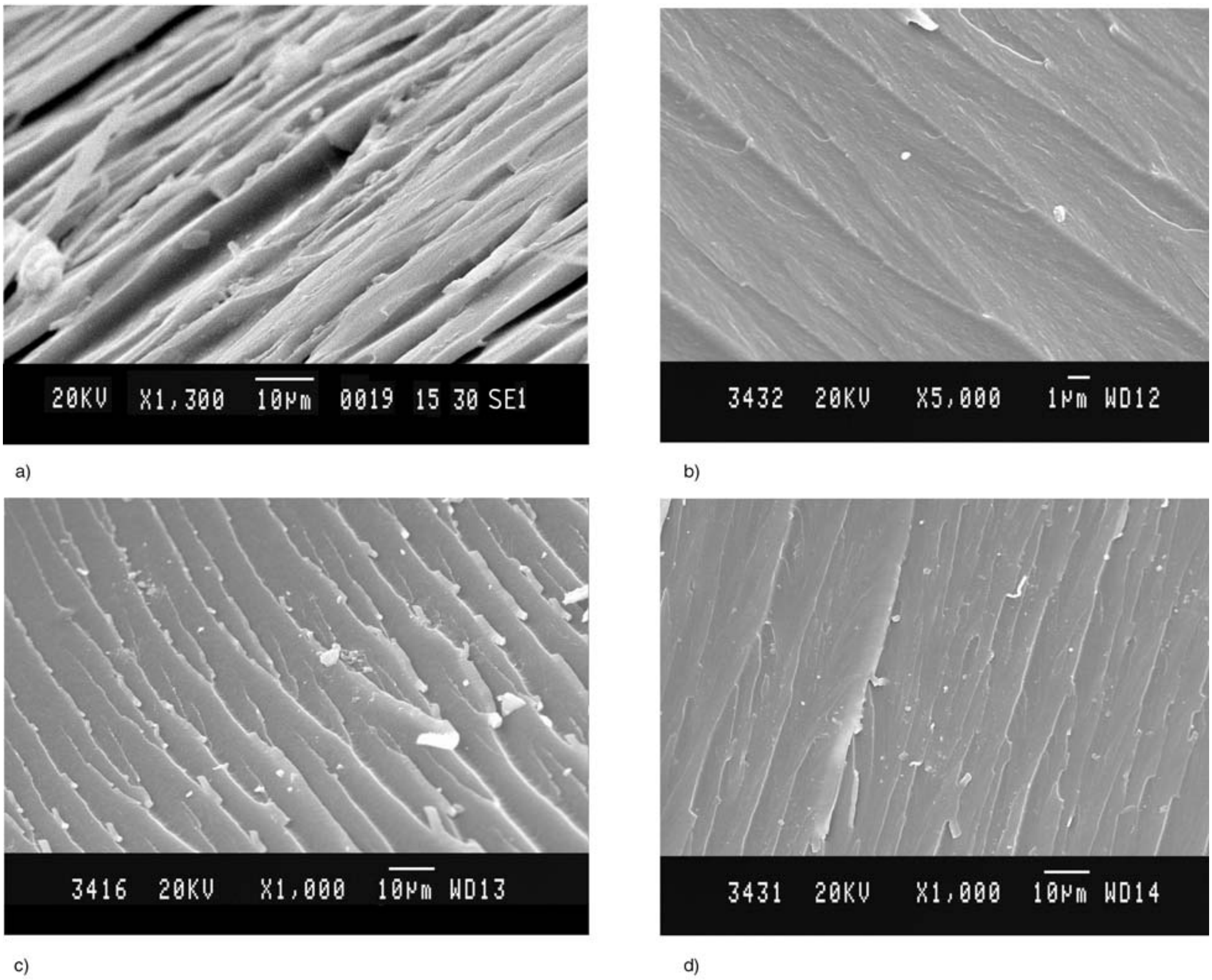

Figure 10. SEM micrographs of (a) unmodified epoxy, (b) 12% PES modified epoxy, (c) 12% BMI modified epoxy and (d) 12% PES and 12% BMI modified epoxy systems

the stress and strain properties with a marginal reduction in toughness and impact strength. It was also observed that the moisture absorption behavior decreased with the increasing polyethersulfone and BMI content in the epoxy systems. The incorporation of BMI plays an important role in reducing moisture absorption of epoxy resin. Data on mechanical properties indicated that by altering the percentage incorporation of polyethersulfone and BMI into epoxy resin, it is possible for the development of modified epoxy hybrid matrix materials with desired mechanical and thermal properties which can be used for high performance aerospace engineering applications.

References

[1] Akutsu U., Inoki M., Daicho N., Kasashima Y., Srirasish N., Marushima I.: Curing behavior and properties of epoxy resins cured with the diamine having the quinoxaline or triazine structure. Journal of Applied Polymer Science, **69**, 1737–1741 (1998).

[2] Vabrik Y., Czajlik I., Túry G., Rusznák I., Ille A., Víg A.: A study of epoxy resin-acrylated polyurethane semi-interpenetrating polymer networks. Journal of Applied Polymer Science, **68**, 111–119 (1998).

[3] Lin M. S., Liu C. C., Lee C. T.: Toughened interpenetrating polymer network materials based on unsaturated polyester and epoxy. Journal of Applied Polymer Science, **72**, 585–592 (1999).

[4] Li Y., Shen S., Liu Y., Gao J.: Kinetics of 4,4′-diaminodiphenylmethane curing of bisphenol-S epoxy resin. Journal of Applied Polymer Science, **73**, 1799–1803 (1999).

[5] Deng B-L., Hu Y-S., Chen L-A., Chiu W-Y., Wu T-R.: The curing reaction and physical properties of DGEBA/DETA epoxy resin blended with propyl ester phosphazene. Journal of Applied Polymer Science, **74**, 229–237 (1999).

[6] Kaji M., Nakahara K., Endo T.: Synthesis of a bifunctional epoxy monomer containing biphenyl moiety and properties of its cured polymer with phenol novolac. Journal of Applied Polymer Science, **74**, 690–698 (1999).

[7] Hedrick J. L., Yilgor I., Jurek M., Hedrick J. C., Wilkes G. I., Mcgrath J. E.: Chemical modification of matrix resin networks with engineering thermoplastics: 1. Synthesis, morphology, physical behaviour and toughening mechanisms of poly(arylene ether sulphone) modified epoxy networks. Polymer, **32**, 2020–2032 (1991).

[8] Mackinnon A. J., Jenkins S. D., McGrail P. T., Pethrick R. A.: Dielectric, mechanical and rheological studies of phase separation and cure of a thermoplastic modified epoxy resin: Incorporation of reactively terminated polysulfones. Polymer, **34**, 3252–3263 (1993).

[9] Huang P., Zheng S., Huang J., Geo Q., Zhu W.: Miscibility and mechanical properties of epoxy resin/polysulfone blends. Polymer, **38**, 5565–5571 (1997).

[10] Mimura K., Ito H., Fujioka H.: Improvement of thermal and mechanical properties by control of morphologies in PES-modified epoxy resins. Polymer, **41**, 4451–4459 (2000).

[11] Jiang X. L., Sunl K., Zhang Y. X.: Effects of dynamical cure and compatibilization on the morphology and properties of the PP/epoxy blends. Express Polymer Letters, **1**, 283–291 (2007).

[12] Cho J. B., Hwang J. W., Cho K., An J. H., Park C. E.: Effects of morphology on toughening of tetrafunctional epoxy resins with poly(ether imide). Polymer, **34**, 4832–4836 (1993).

[13] Oyanguren P. A., Riccardi C. C., Williams R. J. J., Mondragon I.: Phase separation induced by a chain polymerization: Polysulfone-modified epoxy/anhydride systems. Journal of Polymer Science, Part B: Polymer Physics, **36**, 1349–1359 (1998).

[14] Giannotti M. I., Mondragon I., Galante M. J., Oyanguren P. A.: Reaction-induced phase separation in epoxy/polysulfone/poly(ether imide) systems. II. Generated morphologies. Journal of Polymer Science, Part B: Polymer Physics, **42**, 3964–3975 (2004).

[15] Siddhamalli S. K., Kyu T.: Toughening of thermoset/thermoplastic composites via reaction-induced phase separation: Epoxy/phenoxy blends. Journal of Applied Polymer Science, **77**, 1257–1268 (2000).

[16] Giannotti M. I., Solsona M. S., Galante M. J., Oyanguren P. A.: Morphology control in polysulfone-modified epoxy resins by demixing behavior. Journal of Applied Polymer Science, **89**, 405–412 (2003).

[17] Teng K-C., Chang F-C.: Single-phase and multiple-phase thermoplastic/thermoset polyblends: 2. Morphologies and mechanical properties of phenoxy/ epoxy blends. Polymer, **37**, 2385–2394 (1996).

[18] Tanaka N., Iijima T., Fukuda W., Tomoi M.: Synthesis and properties of interpenetrating polymer networks composed of epoxy resins and polysulphones with cross-linkable pendant vinylbenzyl groups. Polymer International, **42**, 95–106 (1997).

[19] Hedrick J. L., Yilgor I., Wilkes G. L., McGrath J. E.: Chemical modification of matrix resin networks with engineering thermoplastics. Polymer Bulletin, **13**, 201–208 (1985).

[20] Hedrick J. L., Yilgor I., Jurek M., Hedrick J. C., Wilkes G. L., McGrath J. E.: Chemical modification of matrix resin networks with engineering thermoplastics: 1. Synthesis, morphology, physical behaviour and toughening mechanisms of poly(arylene ether sulphone) modified epoxy networks. Polymer, **32**, 2020–2032 (1991).

[21] Rajasekaran R., Alagar M.: Mechanical properties of bismaleimides modified polysulfone epoxy matrices for engineering applications. International Journal of Polymer Materials, **56**, 911–927 (2007).

[22] Rajasekaran R., Karikal Chozhan C., Alagar M.: Preparation and characterization of 3,3’-bis(maleimidophenyl)phenylphosphine oxide BMI)/polysulfone modified epoxy intercrosslinked matrices. Polymer Composites, in press (2008).

[23] Ashok Kumar A., Dinakaran K., Alagar M.: Preparation and characterization of siliconized epoxy-1,2-bis(maleimido) ethane intercrosslinked matrix materials. Journal of Applied Polymer Science, **89**, 3808–3817 (2003).

[24] Ashok Kumar A., Alagar M., Rao R. M. V. G. K.: Synthesis and characterization of siliconized epoxy-1,3-bis(maleimido)benzene intercrosslinked matrix materials. Polymer, **43**, 693–702 (2002).

[25] Dinakaran K., Alagar M.: Preparation and characterization of bismaleimide (*N,N′*-bismaleimido-4,4′-diphenyl methane)-unsaturated polyester modified epoxy intercrosslinked matrices. Journal of Applied Polymer Science, **85**, 2853–2861 (2002).

[26] Dinakaran K., Alagar M.: Preparation and characterization of bismaleimide (*N,N′*-bismaleimido-4,4′-diphenyl methane)-vinyl ester oligomer-modified unsaturated polyester interpenetrating matrices for advanced composites. Journal of Applied Polymer Science, **86**, 2502–2508 (2002).

[27] Mahesh K. P. O., Alagar M.: Preparation and characterization of chain-extended bismaleimide modified polyurethane-epoxy matrices. Journal of Applied Polymer Science, **87**, 1562–1568 (2003).

[28] Ashok Kumar A., Alagar M., Rao R. M. V. G. K.: Preparation and characterization of siliconized epoxy/bismaleimide (*N,N′*-bismaleimido-4,4′-diphenyl methane) intercrosslinked matrices for engineering applications. Journal of Applied Polymer Science, **81**, 38–46 (2001).

[29] Ashok Kumar A., Alagar M., Rao R. M. V. G. K.: Studies on thermal and morphological behavior of siliconized epoxy bismaleimide matrices. Journal of Applied Polymer Science, **81**, 2330–2346 (2001).

[30] Kim D. S., Han M. J., Lee J. R.: Cure behavior and properties of an epoxy resin modified with a bismaleimide resin. Polymer Engineering and Science, **35**, 1353–1358 (1995).

[31] Lin K-F., Lin J-S., Cheng C-H.: High temperature resins based on allylamine/bismaleimides. Polymer, **37**, 4729–4737 (1996).

[32] Musto P., Mariuscelli E., Ragosta G., Russo P., Scarinzi G.: An interpenetrated system based on a tetrafunctional epoxy resin and a thermosetting bismaleimide: Structure-properties correlation. Journal of Applied Polymer Science, **69**, 1029–1042 (1998).

[33] Crivello J. V.: Polyimidothioethers. Journal of Polymer Science, Part A: Polymer Chemistry, **14**, 159–182 (1976).

[34] Lüders G., Merker E., Raumbach H.: Polymerisation von n-substituierten Maleimiden in Epoxidverbindungen, 1. Die Angewandte Makromolekulare Chemie, **182**, 135–151 (1990).

[35] Musto P., Mariuscelli E., Ragosta G., Russo P., Scarinzi G.: An interpenetrated system based an tetrafunctional epoxy resin and a thermosetting bismaleimide: Structure-properties correlation. Journal of Applied Polymer. Science, **69**, 1029–1042 (1998).

[36] Zheng S., Zhang N., Luo X., Ma D.: Epoxy resin/poly(ethylene oxide) blends cured with aromatic amine. Polymer, **36**, 3609–3613 (1995).

eXPRESS Polymer Letters Vol.2, No.5 (2008) 349–356
Available online at www.expresspolymlett.com
DOI: 10.3144/expresspolymlett.2008.41

Nanoencapsulation of blocked isocyanates through aqueous emulsion polymerization

H. Yang, S. K. Mendon, J. W. Rawlins[*]

School of Polymers and High Performance Materials, The University of Southern Mississippi, 118 College Drive #10037, Hattiesburg, MS 39406, USA

Received 14 February 2008; accepted in revised form 24 March 2008

Abstract. Blocked isocyanates were successfully encapsulated into polystyrene and hydroxyl and amine functionalized polymeric nanospheres via emulsion polymerization. The nanocapsules were characterized via Fourier transform infrared spectroscopy, differential scanning calorimetry and transmission electronic microscopy. The blocked isocyanates generated free isocyanate functionality upon thermal annealing of nanocapsules. This research establishes a novel encapsulating method for release and retention of free isocyanates in aqueous media. These nanocapsules can provide active isocyanates in coatings and adhesive applications, and represent a novel application of nanoencapsulated materials for controlled or delayed active material utilization.

Keywords: *nanomaterials, nanoencapsulation, nanocapsules, emulsion polymerization, isocyanate*

1. Introduction

The synthesis and application of nanoparticles, i.e., particles smaller than one micron, are of growing interest to both industry and academia. Nanocapsules, a specific class of nanoparticles, are composed of one or more active materials (core) and a protective matrix (shell) [1]. Encapsulation technology has been used to prepare micro/nanocapsules with specific application properties in several areas including food [2], biology [3], and medicine [4]. Nanocapsules have been synthesized via miniemulsion [5, 6] and interfacial polymerization [7, 8] techniques. Couvreur reviewed nanocapsule technologies used in drug carrier systems [9].

Most encapsulation techniques employ isocyanates in either solvent or bulk to form shell (or matrix) materials for encapsulating functional materials, releasable fill materials [10], or making pressure sensitive copying paper [11]. The inherent reactivity of isocyanates with water makes it difficult to encapsulate them in aqueous media. It is even more challenging to maintain isocyanate activity in the presence of hydroxyl- or amine-functional systems. There are no references found in literature for either the incorporation of blocked isocyanates into polymeric nanoparticles or the encapsulation of isocyanates into reactive polymeric shell materials in aqueous media.

In this study, blocked isocyanates were encapsulated within polystyrene nanocapsules and in hydroxyl and amine functionalized nanocapsules via emulsion polymerization. Upon thermal treatment, the blocking agent was released and active isocyanate functionalities were generated that remained stable in the aqueous medium within the protective shell of the nanocapsules. The nanocapsules were characterized via Fourier transform infrared (FTIR) spectroscopy, differential scanning calorimetry (DSC), and transmission electron microscopy (TEM).

---

[*]Corresponding author, e-mail: James.Rawlins@usm.edu

2. Experimental section

2.1. Materials

Desmodur® N 3300A and Desmodur BL 3175A were received from Bayer MaterialScience, Pittsburgh, PA. 2-Hydroxyethyl methacrylate (HEMA), divinylbenzene (DVB), 2-(*tert*-butylamino)ethyl methacrylate (TBAEMA), 2,2′-azobisisobutyronitrile (AIBN), and sodium dodecyl sulfate (SDS) were purchased from Sigma-Aldrich, St. Louis, MO. Styrene was purchased from Alfa Aesar, Ward Hill, MA. Igepal® CO-887 was received from Rhodia, Cranbury, NJ. All reagents were used as received.

2.2. Preparation of nanocapsules

The nanocapsules were prepared through two steps of pre-emulsification (to form a pre-emulsion) and emulsion polymerization, which will be explained in detail below.

2.2.1. Pre-emulsion preparation

Pre-emulsion preparation for one of the nanocapsules (M-6) is provided as an example. The pre-emulsion was synthesized by blending two parts; Part I contained 40 g styrene, 0.8 g DVB, 0.82 g AIBN, and 40 g Desmodur BL3175A; and Part II contained 1.71 g SDS, 1.63 g Igepal CO-887, and 220 g water. Parts I and II were blended magnetically in separate containers for 10 minutes. Part II was then added to Part I under mechanical agitation and the contents were stirred for 30 minutes at 1800 rpm. The resulting pre-emulsion was cooled to <5°C before sonication using a Misonix® sonicator 3000 (until a particle size <250 nm was achieved).

2.2.2. Emulsion polymerization

The pre-emulsion was transferred to a three-neck round bottom flask equipped with a mechanical stirrer, reflux condenser, and a nitrogen inlet, and degassed for 30 minutes. The temperature was raised to 70°C and maintained for 8 hours to complete the polymerization.

2.3. Characterization

The latexes were freeze dried (lyophilization) for 48 hours in the Freezemobile 35EL. Glass transition temperatures (T_gs) were recorded on a differential scanning calorimeter (DSC Q1000, TA Instruments, New Castle, DE), summarized in Table 1. FTIR spectroscopy (attenuated total reflectance and diffuse reflectance, unless specifically stated) was performed using a Scimitar series spectrophotometer (Digilab, Canton, MA). Latex particle sizes were recorded on a capillary hydrodynamic fractionator (CHDF 2000, Matec Applied Sciences, Northborough, MA). TEM was performed on a JEOL JEM-2100 microscope (JEOL Ltd., Tokyo, Japan).

For deblocking studies, the freeze dried samples were treated thermally in the DSC under a nitrogen atmosphere as summarized in Table 2 and characterized via FTIR.

For acetone extraction studies, the freeze dried samples were blended with acetone and agitated on a Vortex-Genie 2™ shaker for 48 hours. The blend was centrifuged using SPD SpeedVac® SPD 121P (Thermo Fisher Scientific, Waltham, MA), and the supernatant liquid was discarded (repeated twice, 20 minutes centrifugation). The pellets were air dried for further analysis.

Table 1. DSC Measurement procedure

Step	Equilibrate [°C]	Ramp to (at 10°C/min) [°C]	Isothermal [min]
I	–50	–	–
II (1st heating)	–	120	3
III	–	–50	3
IV (2nd heating)	–	180	3
V	–	–50	3
VI (3rd heating)	–	180	3
VII	–	–50	3
VIII (4th heating)	–	180	–

Table 2. Deblocking treatment procedure

Step	Equilibrate [°C]	Ramp to (at 10°C/min) [°C]	Isothermal [min]
I	–50	–	–
II	–	120	1
III	–	–50	3
IV	–	160	40
V	–	–50	3
VI	–	180	–

3. Results and discussion

3.1. Isocyanate encapsulated by polystyrene

Blocked isocyanates (BNCO) are widely used in coatings, elastomers, composites, and rubber industries to thermally regenerate isocyanate functionalities. In this study, Desmodur BL3175A, a blocked aliphatic polyisocyanate based on hexamethylene diisocyanate (75% solids, deblocking temperature ~135°C) was chosen for encapsulation into nanocapsules. The BNCO nanocapsules prepared via miniemulsion polymerization are summarized in Tables 3 and 4 (non-functionalized and functionalized nanocapsules are designated as M and N series, respectively). Desmodur N3300A (polymeric hexamethylene diisocyanate) was employed as the control for FTIR characterization. The latex particle sizes are included in the tables and were also confirmed by TEM (TEM image of nanocapsule M-7 is shown as an example in Figure 1).

Table 3. Blocked isocyanate (BNCO) nanocapsules

Sample	DVB* [%]	BNCO* [%]	Particle size [nm]
M-1	2	0	58
M-2	2	10	59
M-3	0	10	57
M-4	2	20	59
M-5	2	30	62
M-6	2	40	59
M-7	2	60	53
M-8	2	80	82
M-9	0	30	56
M-10	4	30	53
M-11	6	30	57

*weight percentage on styrene

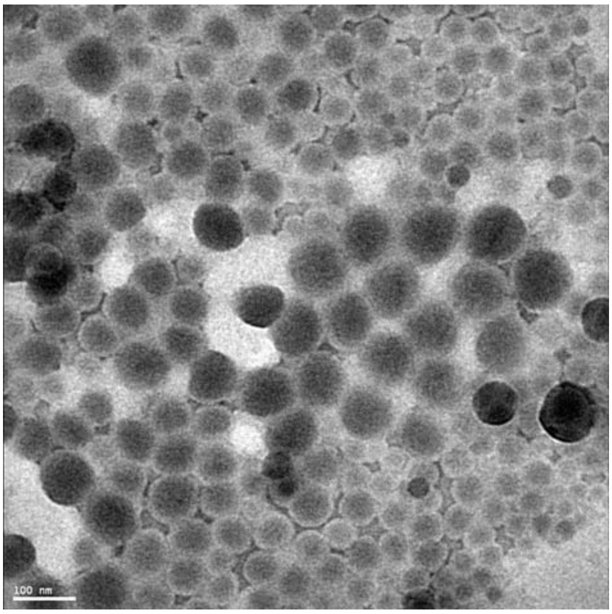

Figure 1. TEM photo of M-7 (scale bar is 100 nm)

3.1.1. FTIR analysis

Isocyanates are characterized by peaks at 1682 (urethane C=O stretching) and 2270 cm^{-1} (N=C=O stretching) for Desmodur N3300A, and at 1682 (urethane C=O stretching) and 1725 cm^{-1} (blocked isocyanate >C=N–O–C(O)–NH, C=O stretching) for Desmodur BL3175A (Figures 2a and 2b). The presence of the characteristic BNCO peaks in the FTIR spectrum of the nanocapsule, M-6 (Figure 2e), and its absence in the FTIR spectrum of the hollow nanosphere, M-1 (Figure 2d), confirmed BNCO inclusion in the nanocapsules.

Nanocapsule M-6 was treated with acetone to extract the incorporated BNCO. The FTIR spectrum of M-6 after acetone extraction (Figure 2f) shows complete disappearance of the characteristic BNCO peaks indicating that the blocked isocyanate was extracted from the nanocapsules by acetone.

Nanocapsules containing the blocked isocyanates generated active isocyanates upon thermal treatment. For deblocking studies, the nanocapsules were freeze dried and treated thermally in the DSC to release the blocking agent. The FTIR spectrum of the BNCO nanocapsule M-6 subjected to deblocking treatment shows the characteristic isocyanate peak (2270 cm^{-1}) (Figure 2g). Figure 2c displays the effect of the deblocking thermal treatment on the blocked isocyanate BL3175A. While

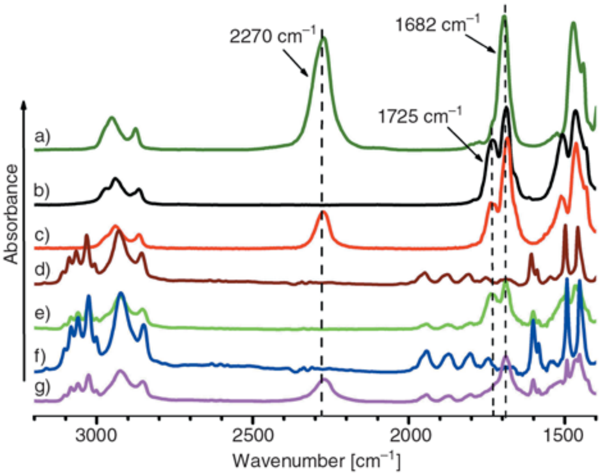

Figure 2. FTIR spectra of a) N3300A, b) BL3175A, c) BL3175A after deblocking treatment, d) M-1, e) M-6, f) M-6 after acetone extraction, and g) M-6 after deblocking treatment

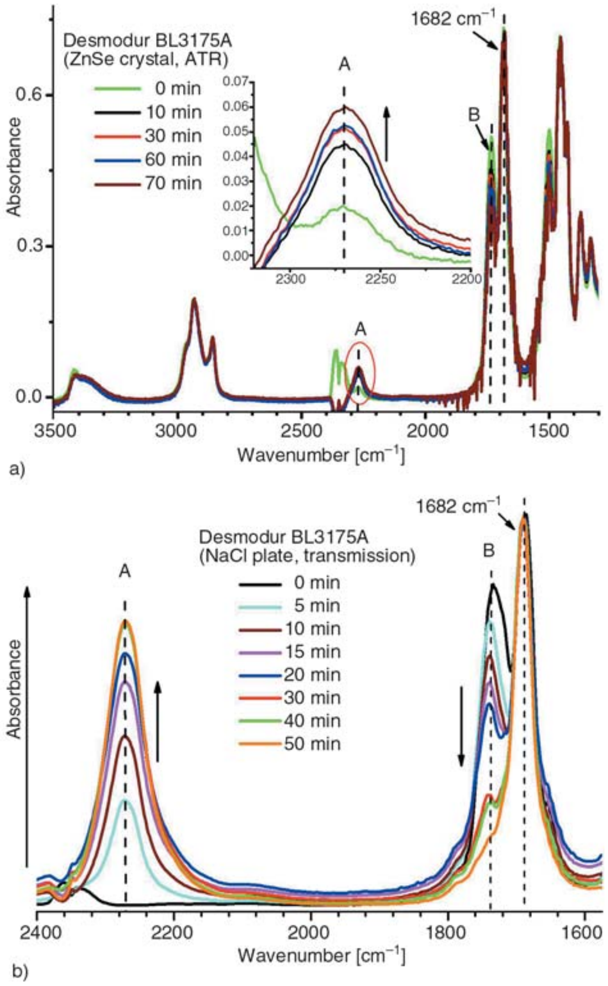

Figure 3. FTIR spectra of BL3175A maintained isothermally for various times at 140°C with a) ATR and b) transmission methods

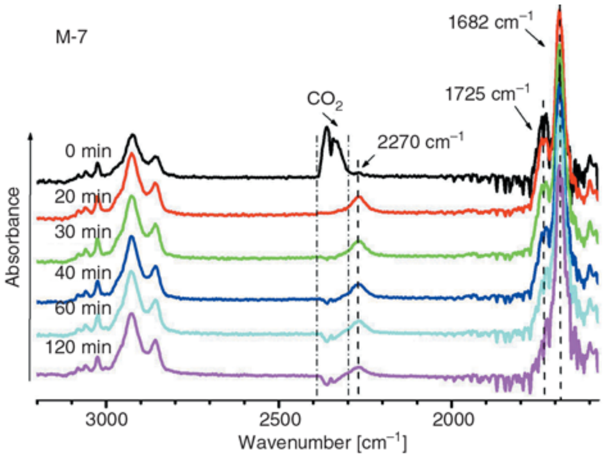

Figure 4. FTIR spectra of M-7 maintained isothermally for various times at 140°C

the presence of the isocyanate peak at 2270 cm^{-1} indicates deblocking, the peak at 1725 cm^{-1} indicates that the BNCO was not completely deblocked by the thermal treatment. The deblocking appeared to be a function of time, therefore BL3175A and nanocapsule M-7 (2% DVB, 60% BNCO) were heated isothermally at 140°C for varying lengths of time and analyzed via FTIR (Figures 3 and 4).

In Figure 3a, the first curve for BL3175A (0 min, bottom line) reveals a small amount of deblocked NCO, which indicates initiation of the deblocking process at 140°C. Subsequent spectra show the effects of isothermal heating of BL3175A for varying lengths of time. The close-up profile (Figure 3a, area A) shows increasing intensity of the NCO peak (2270 cm^{-1}) with time. Even after 70 minutes at 140°C (top line), a small peak is visible at 1725 cm^{-1} (peak B) suggesting the presence of residual blocked isocyanate. Since the ATR method primarily probes only the top two microns of the sample that is in direct contact with the ZnSe crystal, the deblocking of BL3175A was also analyzed via transmission FTIR on sodium chloride plates (Figure 3b). To show the time-dependent deblocking property of BNCO, the transmission FTIR data were re-plotted after normalization at 1682 cm^{-1}. It is evident that the peak A height increased while peak B decreased with time. Peak B disappeared after 50 minutes at 140°C, suggesting that by this time, the isocyanate is completely dissociated via thermal treatment of blocked isocyanate.

A similar heating profile for the M-7 BNCO nanocapsule summarizes the effect of deblocking by the appearance and continued presence of deblocked isocyanate (Figure 4). At the end of 120 minutes, the 1725 cm^{-1} peak has almost disappeared indicating complete deblocking of the original BNCO and free NCO retention.

3.1.2. Effects of crosslinking

The blocking and deblocking of diisocyanates with methyl ethyl ketoxime is a reversible reaction [12]. In these nanocapsules, the polystyrene shell functions as a 'shield' for the deblocked isocyanate by preventing the liberated blocking agent from reentering the nanocapsule. As shown in Figure 5, varying the degree of crosslinking in the polystyrene shell further exemplifies the 'shield effect' (FTIR spectra of N3300A, BL3175A, and BL3175A after deblocking treatment are re-plotted to facilitate comparison).

After subjecting the nanocapsule M-9 (no DVB crosslinker in the shell) to the deblocking treatment, a small shoulder peak is revealed at

1725 cm^{-1}, indicating the presence of residual BNCO (Figure 5f). Nanosphere M-1 (no blocked isocyanate) was blended with BL3175A in the same proportion as present in nanocapsule M-6 and subjected to deblocking treatment (Figure 5e). The strong peak at 1725 cm^{-1} observed upon deblocking the blend indicates the effect of the polystyrene shell on the reaction between the isocyanate and the liberated blocking agent. Increasing the proportion of DVB from 2% (M-5) to 6% (M-11) results in shorter peaks at 1725 cm^{-1} (Figures 5h and 5i). The data validate that increasing the shell's degree of crosslinking (polystyrene shell) enhances the 'shield effect'.

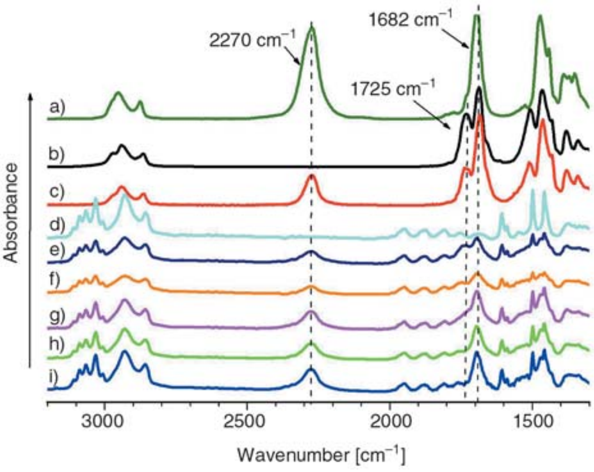

Figure 5. FTIR spectra of a) N 3300A, b) BL3175A, c) BL3175A after deblocking treatment, d) M-1, e) M-1 and BL3175A blend after deblocking treatment, f) M-9 after deblocking treatment, g) M-5 after deblocking treatment, h) M-10 after deblocking treatment, and i) M-11 after deblocking treatment

3.1.3. DSC analysis

DSC thermograms of lyophilized nanocapsules are summarized in Figure 6. BL3175A (Figure 6a) exhibits a T_g of –11.26°C in the second heating cycle before the isocyanate deblocks at 136.59°C. The T_g shifted to –2.51°C in the next heating cycle and the deblocking peaks were no longer evident. However, this does not signify complete deblocking of the blocked isocyanate. For instance, the DSC profile of the thermally treated BL3175A (Figure 2c), does not exhibit a deblocking thermal peak in the heating cycle following isothermal treatment at 160°C for 40 minutes but the IR spectrum of the same sample shows the presence of

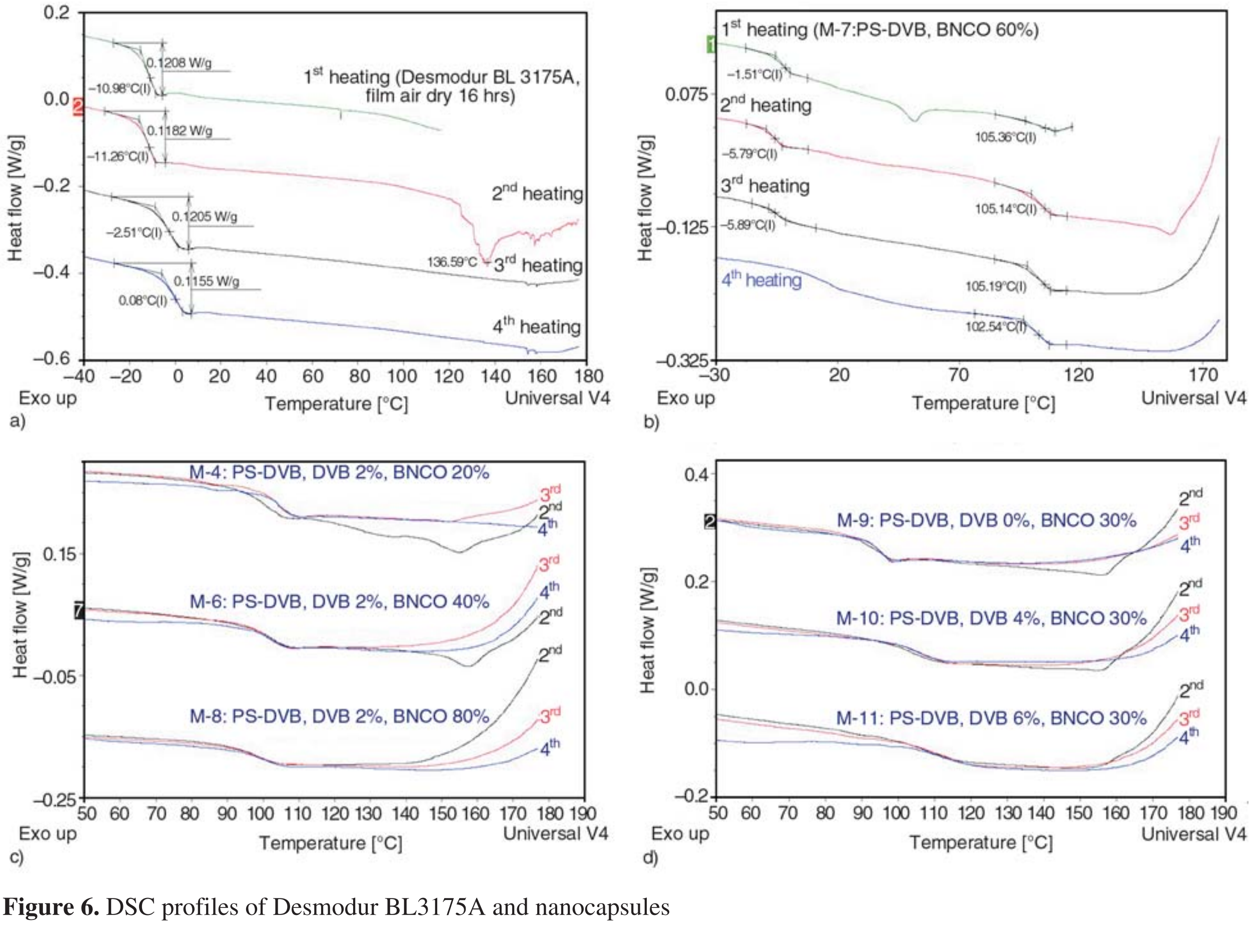

Figure 6. DSC profiles of Desmodur BL3175A and nanocapsules

residual blocked isocyanates. Two distinct T_gs are discernible in the DSC profile of nanocapsule M-7 (Figure 6b). The first Tg of approximately –5°C is attributed to the incorporated BNCO, and the second T_g of approximately 105°C is attributed to the presence of partially crosslinked polystyrene. The separate and distinct T_gs confirm distinct phase separation within nanocapsules.

The effects of time and temperature on deblocking BL3175A should also be noticed in the DSC thermograms of nanocapsules containing varying amounts of BNCO. Nanocapsules containing >20% BNCO exhibited exothermic responses after the second heating cycle, while nanocapsules containing <20% BNCO did not show similar responses (the profile is not included in Figure 6). Additionally, higher degrees of crosslinking in the shell (DVB increased from 2 to 6 wt%) also required longer deblocking times (Figure 6d). Higher crosslinking of the shell is seen to promote the 'shield effect'. DSC analysis was also conducted with open samples (no lid) and closed samples (pan capped with a small hole in the center). The DSC thermograms shown in this paper were all recorded on closed pans. The thermal behaviors of both processes were similar except for the lack of exothermic responses in the open samples, which reflect the effect of crosslinking on the deblocking behavior and the reversible nature of blocked isocyanates establishing an equilibrium in sealed pans, which is consistent with the observations reported by Wicks [13].

3.2. Hydroxyl or amine functionalized polymers encapsulated isocyanate nanocapsule

The above synthesis technique was repeated using HEMA and TBAEMA as comonomers with styrene and divinyl benzene to encapsulate isocyanates via miniemulsion polymerization. The resulting N-series of nanocapsules are summarized in Table 4.

3.2.1. Encapsulation of isocyanate by hydroxyl functionalized polymer

Isocyanate encapsulation was confirmed via FTIR characterization. The FTIR spectra of N3300A and BL3175A are re-plotted for comparison in Figures 7 and 8. The nanocapsule N-5 (Figure 7e) shows a characteristic BNCO peak at 1682 cm^{-1} that is not observed in the FTIR spectrum of the empty nanosphere, N-4 (Figure 7d), and confirms the presence of blocked isocyanate. However, the peak at 1725 cm^{-1} overlaps with the HEMA ester carbonyl of N-4.

The IR spectrum of N-5 treated with acetone to extract the encapsulated BNCO (Figure 7f) shows total disappearance of the BNCO peak at 1682 cm^{-1} confirming blocked isocyanate extraction from the nanocapsules by acetone. The data also suggests that a core-shell structure (isocyanate

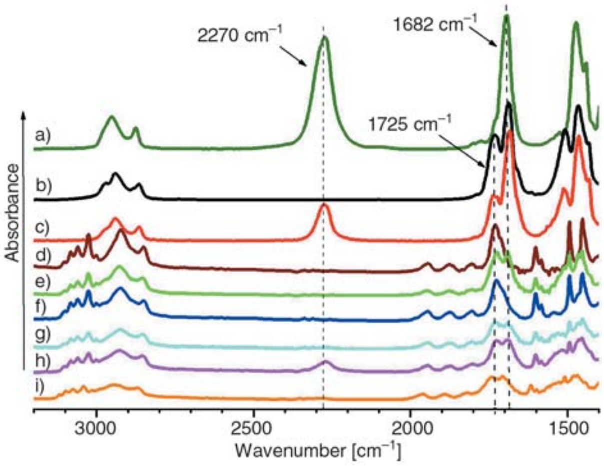

Figure 7. FTIR spectra of a) N3300A, b) BL3175A, c) BL3175A after deblocking treatment, d) N-4, e) N-5, f) N-5 after acetone extraction, g) blend of N-4 and BL3175A after deblocking treatment, h) N-5 after deblocking treatment, and i) N-6 after deblocking treatment

Table 4. Hydroxyl or amine functionalized BNCO nanocapsules

Sample	DVB* [%]	BNCO* [%]	HEMA/S weight ratio	TBAEMA/S weight ratio	Particle size [nm]
N-4	2	0	0.25	–	61
N-5	2	30	0.25	–	57
N-6	0	30	0.25	–	–
N-7	2	30	–	0.25	62
N-8	2	0	–	0.25	–
N-9	0	30	–	0.25	–

*weight percentage on total monomer

core) for nanocapsules was maintained until acetone extraction.

For isocyanate releasing studies, nanocapsules N-6 were freeze dried and treated thermally in the DSC to release the blocking agent. Figures 7c, 7g, and 7h show the effects of deblocking treatment on BL3175A, blend of nanospheres N-4 and BL3175A, and N-5, respectively. While the presence of the free NCO peak at 2270 cm^{-1} indicates deblocking of BL3175A, the peak at 1725 cm^{-1} supports the presence of residual BNCO. After the deblocking treatment, nanocapsule N-5 showed the characteristic NCO peak at 2270 cm^{-1} indicating the presence of active isocyanate functional groups. The functionalized nanocapsules are expected to have the hydroxyl groups on the outside of the shell due to their hydrophilicity. When the blend of hydroxyl-functional empty nanosphere N-4 and BL3175A was subjected to the deblocking treatment (Figure 7g), no peak was seen at 2270 cm^{-1} suggesting that the isocyanate generated upon deblocking had reacted with the hydroxyl groups present on the nanosphere. On the other hand, the isocyanate generated upon deblocking in nanocapsule N-5 is retained in the core of the nanocapsule and does not react with the hydroxyl groups on the outside of the shell. The data is strong support for the efficient encapsulation of isocyanate by the hydroxyl functionalized polymer shells.

The degree of crosslinking in the shell is also demonstrated in Figure 7. Unlike nanocapsule N-5 (2% DVB in the shell), the nanocapsule N-6 (no crosslinker in the shell) does not display the NCO peak at 2270 cm^{-1} after deblocking thermal treatment (Figure 7i). During deblocking, the active isocyanate flows from the uncrosslinked shell, and reacts with the hydroxyl groups on the outside of the shell. It is obvious therefore that DVB plays an important role as a crosslinker in confining the BNCO to the core of the nanocapsule.

3.2.2. Encapsulation of isocyanate by amine functionalized polymer

The nanocapsule N-7 (Figure 8e) shows a characteristic BNCO peak at 1682 cm^{-1} that is not observed in the FTIR spectrum of the empty nanosphere N-8 (Figure 8d). The peak at 1725 cm^{-1} overlaps with the TBAEMA ester carbonyl of N-8.

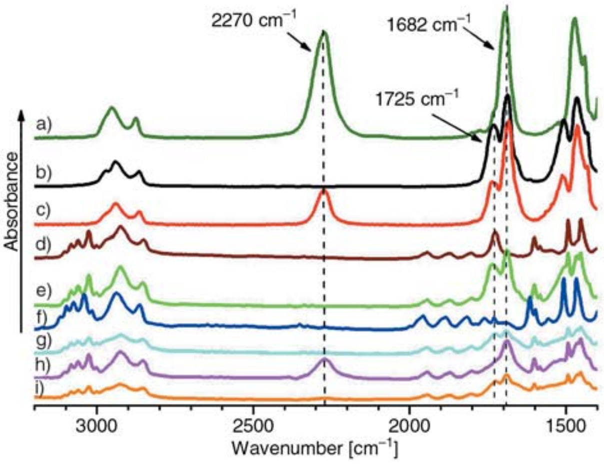

Figure 8. FTIR spectra of a) N3300A, b) BL3175A, c) BL3175A after deblocking treatment, d) N-8, e) N-7, f) N-7 after acetone extraction, g) blend of N-8 and BL3175A after deblocking treatment, h) N-7 after deblocking treatment, and i) N-9 after deblocking treatment

The IR spectrum of N-7 treated with acetone to extract the encapsulated BNCO (Figure 8f) shows the total disappearance of the BNCO peak at 1682 cm^{-1} indicating that the blocked isocyanate was extracted from the nanocapsules by acetone, and supports the core (isocyanate)-shell structure of the nanocapsules. Figures 8c, 8g, and 8h summarize the effect of deblocking treatment on BL3175A, blend of nanospheres N-8 and BL3175A, and N-7, respectively. After deblocking, nanocapsule N-7 exhibits the characteristic NCO peak at 2270 cm^{-1} indicating the presence of active isocyanate functional groups. This peak is not seen in the similarly treated blend of empty nanospheres N-8 and BL3175A (Figure 8g) as the active isocyanate generated upon deblocking reacts with the TBAEMA amine groups present on the nanocapsule shell. However, the isocyanate generated upon deblocking in nanocapsule N-7 does not react with amine groups, and remains in the core as the dissociated free isocyanate, thus confirming the isocyanate encapsulation.

The nanocapsule N-9 (Figure 8i) without DVB crosslinker in the shell does not depict a NCO peak at 2270 cm^{-1} after deblocking treatment. As discussed earlier, it is believed that the deblocked isocyanate is able to flow from the uncrosslinked shell and react with the amine groups on the shell periphery.

Since isocyanate deblocking appeared to be a function of time, nanocapsule N-7 was heated isother-

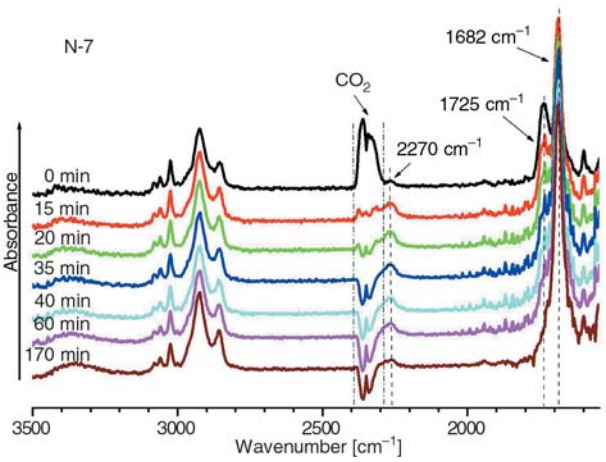

Figure 9. FTIR spectra of N-7 maintained isothermally at 140°C

mally at 140°C for varying lengths of time (Figure 9). The characteristic BNCO peak at 1725 cm^{-1} decreased steadily with time. At 170 minutes, a small shoulder is seen that represents the TBAEMA ester carbonyl. The time-dependent deblocking behavior noted here is consistent with our earlier observations. The NCO peak at 2270 cm^{-1} confirms that the deblocked isocyanates were retained in the core of the nanocapsule and not consumed by the amine groups on the nanocapsule periphery.

4. Conclusions

Isocyanates have been successfully encapsulated into polystyrene, and hydroxyl and amine functionalized nanospheres using a commercially available blocked isocyanate. The research provides a new method for synthesizing nanocapsules containing either blocked or free isocyanates in aqueous media. The thermally dissociated isocyanate can be utilized as an active functional group in coatings and adhesive applications. Nanocapsules containing blocked isocyanates are of interest in self-healing systems where the isocyanate can be liberated by thermal treatment or extracted via solvent or reactive agents such as amines. Nanocapsule shells functionalized with amines and hydroxyls provide a ready moiety for the isocyanate to react once it is liberated from the protective shell of the nanocapsule. Quantitative characterization of the encapsulated isocyanate and the reactivity of released isocyanate are under investigation and will be reported in a subsequent article.

Acknowledgements

This material is based upon work supported by the Cooperative State Research, Education, and Extension Service, U.S. Department of Agriculture, under Agreement Nos. 2001-38202-10424 and 2006-38202-16954. The authors thank Bayer MaterialScience for donating the isocyanates used in this study.

References

[1] Arshady R.: Microspheres, microcapsules and liposomes, Volume 1. Citrus Books, London (1999).
[2] Jackson L. S., Lee K.: Microencapsulation and the food industry. Lebensmittel-Wissenschaft und -Technologie, **24**, 289–297 (1991).
[3] Hildebrand G. E., Tack J. W.: Microencapsulation of peptides and proteins. International Journal of Pharmaceutics, **196**, 173–176 (2000).
[4] Stenekes R. J. H., Loebis A. E., Fernandes C. M., Crommelin D. J. A., Hennink W. E.: Degradable dextran microspheres for the controlled release of liposomes. International Journal of Pharmaceutics, **214**, 17–20 (2001).
[5] Landfester K.: The generation of nanoparticles in miniemulsions. Advanced Materials, **13**, 765–768 (2001).
[6] Qi D-M., Bao Y-Z., Weng Z-X., Huang Z-M.: Preparation of acrylate polymer/silica nanocomposite particles with high silica encapsulation efficiency via miniemulsion polymerization. Polymer, **47**, 4622–4629 (2006).
[7] Ni K-F., Shan G-R., Weng Z-X.: Synthesis of hybrid nanocapsules by miniemulsion (co)polymerization of styrene and γ-methacryloxypropyltrimethoxysilane. Macromolecules, **39**, 2529–2535 (2006).
[8] Jang J., Bae J., Park E.: Selective fabrication of poly(3,4-ethylenedioxythiophene) nanocapsules and mesocellular foams using surfactant-mediated interfacial polymerization. Advanced Materials, **18**, 354–358 (2006).
[9] Couvreur P., Barratt G., Fattal E., Legarnd P., Vauthier C.: Nanocapsule technology: A review. Critical Reviews in Therapeutic Drug Carrier Systems, **19**, 99–134 (2002).
[10] Matkan J., Treleaven R. J.: Particles containing releasable fill material and method of making same. US patent 4681806, USA (1987).
[11] Irii S., Shiozaki T.: Manufacture of microcapsules. JP patent 62193641, Japan (1987).
[12] Lee W-F., Hwong G-Y.: Curing behavior of poly(vinyl chloride)-graft-2-hydroxyethyl methacrylate. European Polymer Journal, **33**, 1499–1504 (1997).
[13] Wicks D. A., Wicks Z. W.: Blocked isocyanates III: Part A. Mechanisms and chemistry. Progress in Organic Coatings, **36**, 148–172 (1999).

eXPRESS Polymer Letters Vol.2, No.5 (2008) 357–363
Available online at www.expresspolymlett.com
DOI: 10.3144/expresspolymlett.2008.42

Thermally conductive and electrically insulating EVA composite encapsulants for solar photovoltaic (PV) cell

B. Lee[1,2*], *J. Z. Liu*[3], *B. Sun*[1], *C. Y. Shen*[1], *G. C. Dai*[1]

[1]National Key Laboratory of Chemical Engineering, East China University of Science and Technology,
130 Meilong Road, Shanghai 200237, P. R. China
[2]School of Mechanical and Power Engineering, East China University of Science and Technology,
130 Meilong Road, Shanghai 200237, P. R. China
[3]Shanghai Solar Energy Science and Technology Co., Ltd., West Gangde Road, Shanghai 200336, P. R. China

Received 26 February 2008; accepted in revised form 26 March 2008

Abstract. A new way of improving the heat dissipating ability and PV efficiency of the solar cells by enhancing the thermal conductivity of the rear EVA layer was reported. The thermal conductivity, electrical resistivity, degree of curing of the EVA encapsulating composites and the PV efficiency of the solar cells are investigated. Filling with the thermal conductive fillers enhances the thermal conductivity of the composites effectively. The thermal conductivity of the filler influences significantly the thermal conductivity of the composite at high filler loading (greater than 20 vol%). Thermal conductivities of the composites filled with SiC, ZnO or BN reach respectively 2.85, 2.26 and 2.08 W/m·K at filler content of 60 vol%. The composites filled with ZnO or BN exhibit superior electrical insulation to those filled with SiC or Al_2O_3. ZnO can promote the cross-linking reaction of the EVA matrix. The test results indicated that the EVA composite encapsulating rear films filled with thermal conductive fillers are able to improve the PV efficiency and the heat dissipating ability of the solar cell effectively.

Keywords: *thermal properties, EVA composite, electrically insulating, encapsulant, solar cell*

1. Introduction

Photovoltaics represent a clean, silent, renewable alternative energy source, potentially beneficial to the environment by preventing greenhouse gases from being produced and entering the atmosphere. With increasing energy demand and environmental pollution, better utilization of solar energy is considered to be the best way for energy generation [1, 2]. In fact, only a small fraction of the incoming sunlight striking the cell is converted into electrical energy (a typical efficiency value for crystalline-Si cells is 14–17%) ; most of the absorbed solar radiation energy by solar cells will be converted into thermal energy and may cause the cells junction temperature to rise unless the heat is efficiently dissipated to the environment [3, 4]. The photovoltaic cell efficiency decreases with increasing cell temperature because of the negative temperature coefficient of crystalline-Si (about –0.4 ~ –0.5%/K). The cells will also exhibit long-term degradation if the temperature exceeds a certain limit [5, 6]. Therefore, some technology means have been developed for cooling the solar cells, such as hybrid photovoltaic/thermal solar system (PV/T) [7–9] and jet impingement cooling device [4, 10].

In practical use, most solar cells are in fact encapsulated into a ‘sandwich’ structure that typically consists of Glass/Ethylene-vinyl acetate (EVA)/ARC-Si/EVA/Tedlar (see Figure 1). The sizes and properties of each layer in encapsulated cells are

---

[*]Corresponding author, e-mail: binlee10@yahoo.cn

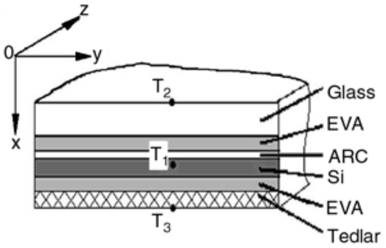

Figure 1. The configuration of laminated & encapsulated Si solar cells [11] (ARC: anti-reflecting coating, Tedlar: a kind of composite film of PET-PVF from DuPont)

Table 1. The sizes and properties of each layer in encapsulated Si solar cells

No.	Layer	Thickness δ [mm]	Thermal conductivity k [W·m^{-1}·K^{-1}]
1	Glass	3.0	0.98*
2	EVA	0.5	0.23*
3	ARC	(0.06–0.1)·10^{-3}	1.38
4	Si	0.25–0.4	148
5	EVA	0.5	0.23*
6	Tedlar	0.1	0.36*

*measured value

listed in Table 1 [11]. Analyzing the properties and sizes in Table 1, it is not difficult to understand that the EVA is the main thermal resistance layer in encapsulated solar cells. So, we hope to improve the heat dissipating ability and PV efficiency of the solar cells by enhancing the thermal conductivity of rear EVA layer. To the authors' knowledge publications related to this aspect have not appeared.

Polymers filled with thermally conductive fillers are emerging as a cost effective way to copy with thermal management issues. The incorporation of highly thermal conductive fillers in polymers to develop high performance thermal conductive encapsulants or thermal interface materials has been mostly desired [12, 13]. A thermal conductivity value of 2.3 W/(m·K) for epoxy resin filled with boron nitride at the loading of 31 vol% was reported, a high thermal conductivity of 4.5 W/(m·K) for 80 vol% aluminum nitride filled epoxy was also achieved [13]. The thermal conductivity of composites is determined by the shape, the size distribution and surface treatment of the filler [14]. Besides the clarity, non-yellowing and dimensional stability, the electrical insulation, curing performance and adhesive processability are also very important to the capsulant of solar cell.

In this paper, we introduce a new way to improve the heat dissipating ability and PV efficiency of the solar cells. The EVA encapsulating composites of solar cell were filled with thermally conductive fillers. The electrical resistivity, thermal conductivity and curing degree of the EVA encapsulating composites are investigated. The PV efficiency of the solar cells encapsulated with the EVA composites or the contrast EVA films on the rear are reported and compared .

2. Experimental

2.1. Materials

The ethylene-vinylacetate (EVA), Elvax-220W, with a melt flow index of 150 g/10 min,vinyl acetate content of 28% and density of 0.951 g/cm^3, supplied by DuPont chemical company was used in this work. Magnesium oxide (MgO) and aluminium oxide (Al_2O_3) were obtained from Sinopharm Shanghai Chemical Reagent Co., Ltd. Zinc oxide (ZnO) was obtained from Shanghai Jinghua Chemical Co., Ltd. Silicon carbide (SiC), boron nitride (BN) and aluminium nitride (AlN) were obtained from Shanghai Institute of Ceramics, Chinese Academy of Sciences. The silane coupling agents of glycidoxypropyl trimethoxysilane (KH-560) and amino-propyl triethoxysilane (KH-550) were obtained from Shanghai Yaohua chemical Co., Ltd. The aluminium and titanium composite coupling agent (OL-AT1618, $Al(OR)_n(OOCR'')_{3-n}Ti(OR')_m(OOCR'')_{4-m}$) was supplied by Shanxi Provincial Institute of Chemical Industry. The titanate coupling agent (NDZ-132, $(CH_3)_2CHOTi(OOCR)_3$) was obtained from Nanjing Shuguang Chemical Co., Ltd., China.

Table 2. The property of fillers [15]

	MgO	Al_2O_3	ZnO	SiC	BN	AlN
Density [g /cm^3]	3.58	3.96	5.6	3.22	2.25	3.26
Thermal conductivity [W·m^{-1}·K^{-1}]	30	26	34	56	35	31
Average size [μm]	1.1	1.3	1.0	1.9	1.5	2.0
Shape	random grain					

2.2. Surface modification

In order to ensure filler good dispersion and to improve the interface interaction between the filler and matrix, we used the coupling agents as described above for surface modification of the fillers. The surface modification was carried out as follows: (1) mixing the filler and the coupling agent of 1 wt% in terms of filler weight in a small amount of isopropyl alcohol at 80°C for 2 h, (2) vacuum drying to remove solvent at 85°C for 24 h, (3) exposing the filler to ambient air for 4 h, (4) heat treating the filler at 100/120°C for 4 h. The treated fillers were stored in vacuum dryer.

2.3. Composite sample preparation

The EVA and fillers, which were weighed in terms of a certain volume content, were mixed on a two-roll mill (SK-160B, Shanghai Rubber Machine Company, China) at temperature of 90±5°C for 15 minutes; and then the molten compounds were transferred into the mold with the required dimension (50 mm diameter and 5–7 mm thickness for thermal conductivity, 150 mm diameter and 1–3 mm thickness for electrical insulation). Pressure up to 10 MPa was applied by hydraulic press (YX-25, Shanghai Ximaweili Rubber and Plastic Machine Company, China) and kept for 3 minutes at room temperature. The cylinder sample with 50 mm diameter and 5–7 mm thickness was released out of the mold. The samples were polished with sandpaper until surface become smooth. For the EVA encapsulating composite rear film of solar cell, the peroxide (Trogonox 101, Akzo Nobel) of 1.5 wt% and the coupling agent (KH-560 or OLAT-1618) of 1 wt% in terms of matrix weight were mixed with EVA and fillers. Pressure up to 10 MPa was applied by hydraulic press and kept for 10–15 minutes at 80–85°C until the thickness of film was about 0.5 mm.

2.4. Preparation of solar cells

In this paper, the solar cells are laminated and encapsulated into a typical ‘sandwich’ structure that consists of Glass/EVA/ARC-Si/Composites rear film/Tedlar (refer to Figure 1). The lamination was done at temperature of 135°C for 30 min, under a pressure of 0.07–0.08 MPa.

2.5. Characterization

The thermal conductivity of composites was measured with an Anter thermal conductivity meter (Quickline-10B, American Anter Corporation) according to ASTM E 1530 (Guarded heat flow meter method).

The electrical resistivity of composites was directly measured with CANY high resistivity meter (ZC-43, Shanghai Cany Precision Instrument Co., Ltd. China).

The curing degree of composites was measured as the ratio of remaining EVA weight to original EVA weight after Soxhlet extracted with toluene at 110°C for 12 h.

PV efficiency of the solar cells was evaluated by surveying maximum output power of the solar cells under given irradiation intensity (1000.0 W/m^2) and ambient temperature (25°C). Surfaces temperatures (T_2 – upper, T_3 – rear, see Figure 1) were measured with infrared thermometer after 2 h out’-door (the ambient temperature of 27–29°C).

3. Results and discussion

3.1. The effect of fillers on the thermal conductivity of EVA composite

Various thermally conductive fillers were mixed to EVA matrix in order to improve the thermal conductivity and heat dissipating ability of the EVA encapsulating composite rear film of the solar cell. The thermal conductivities of EVA composites filled with different fillers are shown in Figure 2. It can be seen that all thermal conductivities of the EVA composites rise gradually with the volume contents of fillers increasing. The thermal conductivities of composites rise very slowly at low filler

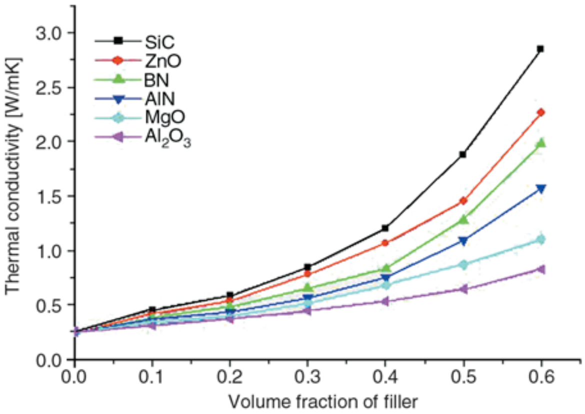

Figure 2. Thermal conductivity of the EVA composites

loading, because the thermally conductive filler particles are surrounded by matrix can not touch each other and the matrix has high thermal resistance. When the loading of thermally conductive filler exceeds 20 vol%, the filler particles easily to touch each other and form more compact packing heat conductive structure, and that results in thinner layers of matrix between the particles, which decreases the contact heat resistance; so, the heat conductive filler have a greater effect on the thermal conductivity of the composites than that at low filler loading, and the thermal conductivity increases rapidly.

However, there are marked differences between the thermal conductivities of the EVA composites filled with differet fillers at high filler loading (greater than 20 vol%). The thermal conductivities of the composites filled with SiC, ZnO or BN all rise rapidly, but the thermal conductivities of the composites filled with Al_2O_3 or MgO increase slowly. The thermal conductivity of the composites filled with SiC, ZnO or BN reach respectively 2.85, 2.26 and 2.08 W/(m·K) at a filler content of 60 vol%. Comparing the thermal conductivities of the composites and that of the fillers, it is not difficult to understand that the thermal conductivity of the filler still have a main effect on the thermal conductivity of the composite at high filler loading (greater than 20 vol%) though the ratios of the thermal conductivities of the fillers to that of EVA matrix are all greater than 100. Therefore, the view that there is no significant improvement in the thermal conductivity of the composite when the intrinsic thermal conductivity of the filler is greater than 100 times that of the polymer matrix [16, 14], is valid only for composites with low filler loading (typically less than 15 vol%). The law of experimental data can be explained with the geometric mean model, which is valid and suitable for predicting the thermal conductivities of multicomponent systems (Equation (1)) [17]:

$$k = k_m^{(1-\Phi)} k_f^{\Phi} \tag{1}$$

where k, k_m and k_f represent respectively the thermal conductivities of the composites, the polymer matrix and the fillers, Φ represent the volume fraction of the fillers. According to the equation, the higher the thermal conductivity of the filler, the faster the thermal conductivity of the composite rise with the volume fraction of the filler increasing. The geometric mean model is fairly good agreement with the law of measured thermal conductivities. In this paper, SiC, ZnO and BN are more suitable to be taken for thermally conductive filler than Al_2O_3 and MgO.

3.2. The influence of fillers on the electrical resistivity of EVA composite

The electrical insulation is a very important property of the encapsulant of a solar cell; therefore, we investigated the influence of different fillers on the electrical resistivity of EVA composite in this paper. Figure 3. shows the bulk electrical resistivity curves of EVA composites filled with different fillers at various volume fractions. It can be seen that the bulk electrical resistivities of EVA composites all increase first and then decrease with the volume fractions of the fillers. At low filler loading, there is no electrical current between the filler particles (by tunneling or hopping) as a result of long distance between the particles, and the potential barrier due to the interfaces are too high for electron hopping. So, the bulk electrical resistivities of composites are high. As the filler load increases and the distance between particles decreases, the electrical current increases, conductive clusters appear resulting in a gradual decrease of the bulk electrical resistivities of the composites [18].

From Figure 3, there are obvious differences between the bulk electrical resistivities of the EVA composites filled with various fillers. The bulk resistivities of the composites filled with ZnO or BN decrease slowly, but that with SiC or Al_2O_3 decrease rapidly with rising filler loading. At the

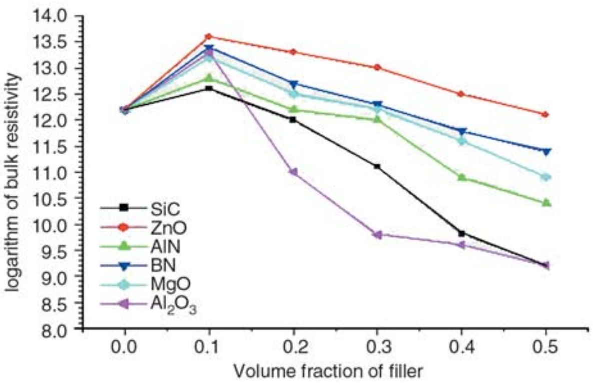

Figure 3. The bulk electrical resistivity of the EVA composites

volume fraction of 0.5, the bulk resistivities of the composites filled with ZnO still maintain 10^{12} Ω·m, but that with SiC or Al_2O_3 decrease to 10^9 Ω·m. Consequently, from the viewpoint of electrical insulation, ZnO and BN are more suitable as a filler of the composite encapsulant than SiC or Al_2O_3 in this paper.

3.3. The influence of different fillers on the curing degree of the EVA composites

As one of the important property of encapsulant film of the solar cell, the curing degree ought to reach about 65% or higher usually. So, in this paper, we also investigated the influence of different fillers on the curing degree of EVA composites. Figure 4 shows the experimental results.

From Figure 4, it can be found out that SiC and BN are able to reduce the cross-linking degree of the EVA matrix, but the ZnO can increase the cross-linking curing degree. The reason of these phenomena is probably that the cross-linking reaction of the EVA matrix is a kind of free radical cross-linking reaction, and the ZnO known as an activator of the peroxide decomposition may activate the free radical reaction, but SiC and BN may have deactivating effect on the free radical reaction. Treated with the coupling agents (KH-560 or OLAT-16), the activating property of the ZnO and the deactivating properties of the SiC and BN all were reduced. So, the cross-linking curing degrees of the EVA composites filled with treated SiC or BN all rise; however, that with treated ZnO decrease.

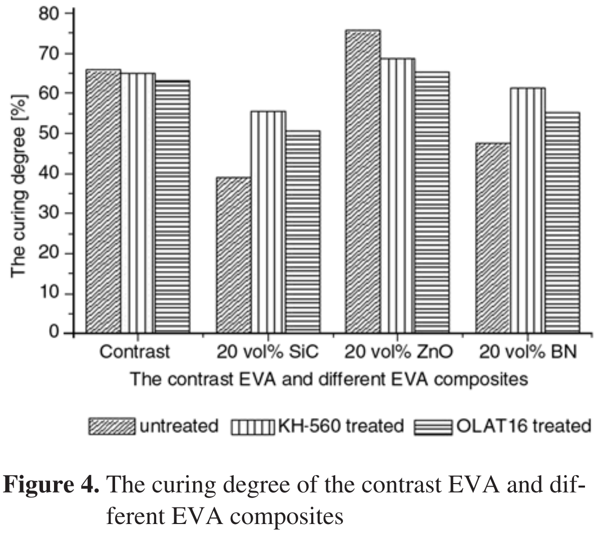

Figure 4. The curing degree of the contrast EVA and different EVA composites

3.4. SEM of the EVA encapsulating composites filled with fillers

The SEM of the EVA composites filled with BN (27 vol%) or ZnO (27 vol%) are shown in Figure 5 and Figure 6. From those figures, it can be seen that fillers (BN or ZnO) treated with the coupling agents (KH-560 or OLAT-16) can be dispersed well and compounded effectively in the EVA matrix.

3.5. The effect of the fillers and couplers on the PV efficiency and heat dissipating ability of the solar cells encapsulated with the EVA composites film on the rear

Enhancing the PV efficiency of the solar cell is our main aim of improving the EVA encapsulating rear film of the solar cell. So, we investigated the maximum output powers (P_{max}) of the solar cells encapsulated with the EVA composite rear films or the

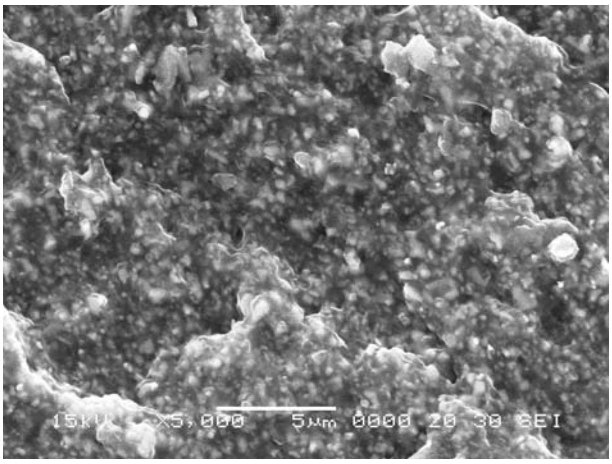

Figure 5. SEM of the EVA composite filled with BN (27 vol%)

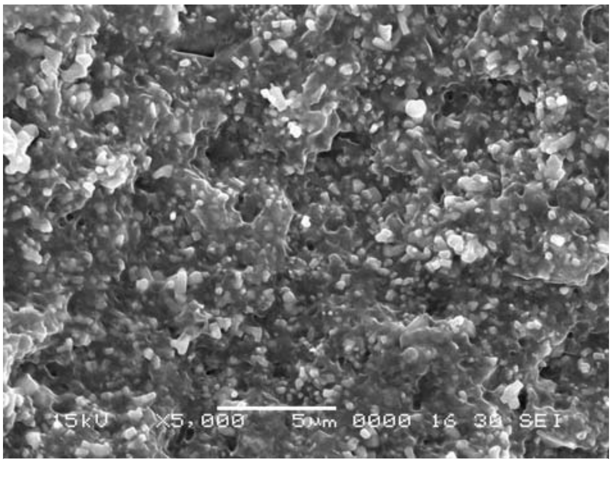

Figure 6. SEM of the EVA composite filled with ZnO (27 vol%)

Table 3. The maximum output power and the surface temperatures of the solar cells

Rear film	Reference	20 vol% SiC (KH-560)	20 vol% BN (KH-560)	20 vol% ZnO (KH-560)	20 vol% ZnO (OLAT-1618)	10 vol% ZnO (KH-560)
P_{max} [W]	5.15	5.25	5.29	5.41	5.10	5.23
ΔP/P [%]	0	1.94	2.72	5.05	–0.97	1.55
T_2 (upper) [°C]	44.8	44.2	44.2	43.8	44.4	44.6
T3(rear) [°C]	45.4	48.6	47.2	47.8	46.6	46.4
ΔT (T_3–T_2) [°C]	0.6	4.4	3.0	4.0	2.2	1.8

reference EVA rear film (Bridgestone) under given irradiation intensity (1000.0 W/m^2). The surface temperatures of the solar cells also were measured after outdoor exposed 2 h. The test results shown in Table 3.

From Table 3, we can find out that various couplers and thermally conductive fillers have different effect on the PV efficiency and heat dissipating ability of the solar cell, the composite rear film mixed with KH-560 and the thermal conductive fillers improve the maximum output powers of the solar cells effectively, the maximum rate of the cell output power increase reaches 5.05%; but the composite encapsulating rear film treated with OLAT-1618 caused the maximum output power of the solar cell decrease slightly, and yellowing obviously after high temperature curing. It can also be seen that the composite encapsulated rear film filled with thermal conductive fillers allow the increase of the rear surface temperature (T_3) and the difference between T_2 and T_3 (ΔT). It indicate that the composite encapsulated rear film has more effective heat dissipating ability than the reference EVA film at the same ambient temperature. Several other factors, such as the properties of the silicon, light reflection, the temperature of cell and the insulation of encapsulant etc, can effect the PV efficiency of the solar cell [19]. From the test results, the EVA composite encapsulating rear film filled with the thermal conductive fillers and KH-560 enhance the PV efficiency and heat dissipating ability of the solar cell effectively.

4. Conclusions

Filling with thermally conductive fillers can enhance the thermal conductivity of the composites effectively. The thermal conductivity of the filler exert a major effect on the thermal conductivity of the composite at high filler loading (greater than 20 vol%). The thermal conductivities of the EVA composites filled with SiC, ZnO or BN reach respectively 2.85, 2.26 and 2.08 W/(m·K) at a filler content of 60 vol%. The EVA composites filled with ZnO or BN have more superior electrical insulation than that those filled with SiC or Al_2O_3. ZnO can promote the cross-linking reaction of the EVA matrix, but SiC and BN reduce the cross-linking curing degree of the EVA matrix. Treated with the coupling agents (KH-560 or OLAT-16), the fillers (BN or ZnO) can be dispersed well and compounded effectively in the EVA matrix . The EVA composite encapsulating rear films filled with suitable coupler and thermally conductive fillers are able to improve the PV efficiency and the heat dissipating ability of the solar cell effectively.

References

[1] Sun S-S., Sariciftci N. S.: Organic photovoltaics: Mechanisms materials and devices. CRC Press, Boca Raton (2005).

[2] Bube R. H.: Photovoltaic materials. Imperial College Press, London (1998).

[3] Tripanagnostopoulos Y., Nousia T., Souliotis M., Yianoulis P.: Hybrid photovoltaic/thermal solar system. Solar Energy, **72**, 217–234 (2002).

[4] Royne A., Dey C. J., Mills D. R.: Cooling of photovoltaic cells under concentrated illumination: A critical review. Solar Energy Materials and Solar Cells, **86**, 451–483 (2005).

[5] Fraisse G., Ménézo C., Johannes K.: Energy performance of water hybrid PV/T collectors applied to combisystems of direct solar floor type. Solar Energy, **81**, 1426–1438 (2007).

[6] Brinkworth B. J., Cross B. M., Marshall R. H., Yang H.: Thermal regulation of photovoltaic cladding. Solar Energy, **61**, 169–178 (1997).

[7] Huang B. J., Lin T. H., Huang W. C., Sun F. S.: Performance evalution of solar photovoltaic/thermal systems. Solar Energy, **70**, 443–448 (2001).

[8] Rockendorf G., Sillmann R., Podlowski L., Litzenburger B.: PV-hybrid and thermoelectric collectors. Solar Energy, **67**, 227–237 (1999).

[9] Sandnes B., Rekstad J.: A photovoltaic/thermal (PV/T) collector with a polymer absorber plate. Experimental study and analytical model. Solar Energy, **72**, 63–73 (2002).

[10] Royne A., Dey C. J.: Design of a jet impingement cooling device for densely packed PV cells under high concentration. Solar Energy, **81**, 1014–1024 (2007).

[11] Lu Z. H., Yao Q.: Energy analysis of silicon solar cell modules based on an optical model for arbitrary layers. Solar Energy, **81**, 636–647 (2007).

[12] Procter P., Solc J.: Improved thermal conductivity in microelectronic encapsulants. in' Proceedings of 41st Electronic Components and Technology Conference, Atlanta, USA' 835–842 (1991).

[13] Bujard P., Kuhnlein G., Ino S., Shiobara T.: Thermal conductivity of molding conpounds for plastic packaging. in' Proceedings of 44th Electronic Components and Technology Conference, Washington, USA', 159–163 (1994).

[14] Lee G-W., Park M., Kim J., Lee J. I., Yoon H. G.: Enhanced thermal conductivity of polymer composites filled with hybrid filler. Composites, Part A: Applied Science and Manufacturing, **37**, 727–734 (2006).

[15] Ma Q. F., Fang R. S., Ciang L. C., Guo S.: Handbook of thermophysical properties (in Chinese). Chinese Agricultural Machinery Press, Beijin (1986).

[16] Bhattacharya S. K.: Metal-filled polymers. Marcel Dekker, New York (1986).

[17] Dawson D. M., Briggs A.: Prediction of the thermal conductivity of insulation materials. Journal of Materials Science, **16**, 3346–3356 (1981).

[18] Huang J-C.: Carbon black filled conducting polymers and polymer blends. Advances in Polymer Technology, **21**, 299–313 (2002).

[19] Zweibel K.: Basic photovoltaic principles and methods. Van Nostrand Reinhold Press, New York (1984).

eXPRESS Polymer Letters Vol.2, No.5 (2008) 364–372
Available online at www.expresspolymlett.com
DOI: 10.3144/expresspolymlett.2008.43

Structural, mechanical and electrical characterization of epoxy-amine/carbon black nanocomposites

Th. V. Kosmidou[1], A. S. Vatalis[1], C. G. Delides[1], E. Logakis[2], P. Pissis[2*], G. C. Papanicolaou[3]

[1]Technological Educational Institute of West Macedonia, Laboratories of Physics and Materials Technology, 50100 Kila, Kozani, Greece
[2]National Technical University of Athens, Department of Physics, Zografou Campus, 15780 Athens, Greece
[3]University of Patras, Department of Mechanical and Aeronautical Engineering, Rio Patras 26500, Greece

Received 5 February 2008; accepted in revised form 30 March 2008

Abstract. This work presents an insight into the effect of preparation procedure and the filler content on both electrical and mechanical properties of a nanocomposite system. For the preparation of the nanocomposites diglycidyl ether of bisphenol A (DGEBA) was used with triethylenetetramine (TETA) as a curing agent. As fillers carbon black (CB) nanoparticles with size from 25 to 75 nm were used. The characterization was done using Dynamic Mechanical Analysis (DMA), Dielectric Relaxation Spectroscopy (DRS), Differential Scanning Calorimetry (DSC), Wide Angle X-ray Diffraction (WAXD) and electrical conductivity measurements. The dependence of the dynamic mechanical and dielectric parameters (E', E'', tanδ, ε', ε'', σ and T_g) is associated with the filler content and is controlled by the employed curing conditions. An increase in electrical conductivity, which is observed at about 1% w/w of carbon black, indicates the creation of conducting paths and is associated with the Maxwell Wagner Sillars (MWS) relaxation, probably due to the formation of aggregated microstructures in the bulk composite.

Keywords: *nanocomposites, epoxy resin, carbon black, curing, glass transition*

1. Introduction

Nanocomposites show properties different from bulk polymers because of the small size of the filler and the corresponding increase in the surface area [1–7]. It is well known that the composite properties can change dramatically with the dispersion state, geometric shape, surface properties, particle size, and particle size distribution. Because of the recent commercial availability of nanoparticles, there is an increasing interest in polymer nanocomposites. These composites exhibit substantial improvements in their mechanical properties, such as the strength, modulus, and dimensional stability, permeability to gases, water and hydrocarbons, thermal stability, flame retardancy, chemical resistance, and electrical, dielectric, magnetic and optical properties [8–15].

The effect of the nanofillers in polymer composites on the glass transition (T_g) and the relaxation behaviour of the polymer matrix has been studied for different filler-resin composites. In some cases an increase in T_g is reported in literature [2–4, 7], but the opposite result is also possible [5]. An initial decrease in T_g followed by an increase, at higher filler loadings, was observed in epoxy/carbon nanotubes composites [11]. In many cases, the amount, the dispersion and the surface conditions of the nanoparticles play important role in the changes in T_g and the mechanical properties of the nanocomposites [2, 6, 7].

---

[*]Corresponding author, e-mail: ppissis@central.ntua.gr

In epoxy nanocomposites (generally in thermoset nanocomposites) there is an additional difficulty, as compared to thermoplastic nanocomposites. The conditions of the nanocomposites curing (and consequently the results of it) are usually different from those of the pure epoxy, due to the participation of the nanoparticles on the crosslinking mechanism [16].

Epoxy resins are electrical insulators. In order to dissipate electrostatic charges and to prepare materials with antistatic properties conductive nanoparticles such as carbon are dispersed in the polymer matrix [17]. Conductive filler – insulating polymer composites become conductors when the filler content reaches a critical value and their electrical conductivity show a sharp increase (percolation threshold). Balancing electrical conductivity with desirable mechanical behavior is one of the largest challenges for the use of filled polymer nanocomposites in various applications.

In this work we focus on the effect of both the curing procedure and the filler content, on the glass transition and the electrical and mechanical behaviour of the system.

2. Experimental

2.1. Materials

The pre-polymer D.E.R.332 used in this study is diglycidyl ether of bisphenol A (DGEBA) supplied by Fluka SA, U.S.A. The hardener used was triethylenetetramine (TETA) supplied by Sigma Aldrich, U.S.A. The extra conductive carbon black (particle size 25–75 nm) was obtained from Degussa, Germany; the typical values of the materials properties are presented in Table 1. All the components of the system are commercial products and were used without purification.

Table 1. Typical values for the carbon black used

Iodine absorption	[mg/g]	1075	ASTM D1510
CTAB surface area	[m^2/g]	600	ASTM D3765
OAN*	ml/100 g	380	ASTM D2414
COAN**	ml/100 g	370	ASTM D3493
Ash content	[%]	0.3	ASTM D1506
Heating loss at packaging	[%]	0.2	ASTM D1509
Sieve residue, 325 mesh	[ppm]	20	ASTM D1514
Pour density	[g/dm^3]	130	ASTM D1513

*oil absorption number

**oil absorption number on compressed sample

2.2. Sample preparation and methods

2.2.1. Sample preparation

The DGEBA/TETA/CB nanocomposites were prepared by the dispersion of the determined amount of CB in a glass vessel. Prior to that procedure, the pre-polymer was heated at 40°C in order to decrease the viscosity. The stoichiometric amount of TETA was added to the DGEBA matrix, and then the mixture was mechanically stirred for 1 h at 2000 rpm and degassed under vacuum for 15 min. Finally, the mixture was sonicated for 30 min in order to break up the CB agglomerates [1] and degassed again. The homogeneous liquid was poured in rectangular shaped Teflon molds and the samples were cured at 60°C for 20 h. Some of the samples were subjected to a post-curing procedure at 150°C for 2 h.

The amount of the hardener in the material is 14 phr (per hundred resin) corresponding to the stoichiometric ratio for complete curing of the resin. Seven series of specimens were produced, each one with different filler content, starting from 0% filler (pure resin), 0.05, 0.1, 0.5, 0.7, 1 and 2% w/w.

2.2.2. Wide angle X-ray scattering

Wide angle X-ray diffraction (WAXD) data were collected in the range of 2θ from 5 to 65° by a Philips PW1965/20 powder diffractometer, with Bragg-Brentano (θ, 2θ) geometry, using non-monochromated CuK_α radiation ($\lambda = 1.54051$ Å). The reflected intensities were recorded as a function of the scattering angle (2θ). The size of the orientation regions L was calculated by the Scherrer's formula (1) [18]:

$$L = \frac{0.9\lambda}{\cos\theta \cdot \mathrm{FWHM}} \tag{1}$$

where λ is the wavelength, θ is the position of the peak and FWHM the width in the middle of the peak.

2.2.3. Dynamic Mechanical thermal Analysis (DMA)

A Polymer Laboratories dynamic mechanical thermal analyzer MK III operating at a frequency of 10 Hz, a strain of 4× and a scanning rate of 2°C/min was used. Measurements were performed from room temperature up to 200°C and the resultant changes in E', E'' and tanδ were plotted.

2.2.4. Differential Scanning Calorimetry (DSC)

A Perkin Elmer Differential Scanning Calorimeter (Pyris 6, DSC) was used under nitrogen atmosphere. The measurements were performed from room temperature to 200°C at a programmed heating rate of 20°C/min.

2.2.5. Dielectric measurements

With DRS analysis, the complex dielectric permittivity ($\varepsilon^* = \varepsilon' - i\varepsilon''$, where ε' is the dielectric constant and ε'' is the dielectric loss) is measured as a function of frequency (10^{-2}–10^6 Hz) and temperature (from –150 to 200°C) [19–22]. An Alpha Analyser, in combination with a Quatro Cryosystem (Novocontrol, Germany), was used. Each sample was clamped between gold-plated, stainless steel electrodes in a Novocontrol dielectric cell. By measuring the complex impedance ($Z^* = Z' - iZ''$) of the circuit, the complex permittivity ($\varepsilon^* = \varepsilon' - i\varepsilon''$) arises from Equation (2):

$$\varepsilon^*(\omega) = \frac{1}{i\omega Z^*(\omega) C_0} \qquad (2)$$

where ω is the angular frequency ($\omega = 2\pi f$) of the applied electric field and C_0 the equivalent capacitance of the free space.

2.2.6. Conductivity measurements

Using the complex permittivity data, the frequency-dependent ac electrical conductivity (real part, σ) is obtained from Equation (3):

$$\sigma = \varepsilon'' \cdot \omega \cdot \varepsilon_0 \qquad (3)$$

where $\varepsilon_0 = 8.85 \cdot 10^{-12}$ F·m^{-1} is the permittivity of free space.

3. Results and discussion

3.1. Morphological characterization

The WAXD spectra are shown in Figure 1. Epoxy nanocomposites were completely amorphous showing an amorphous halo at 19° of 2θ which is independent in position and magnitude from the filler content. This broad peak is probably attributed to the formation of small clusters with some molecular orientation [18], the size of which is calculated from the Scherrer's formula (Equation (1)) to be about 8 Å. These regions of molecular order are consistent with the close alignment of the epoxy elements of the matrix which occurs when the bisphenol groups are able to close pack.

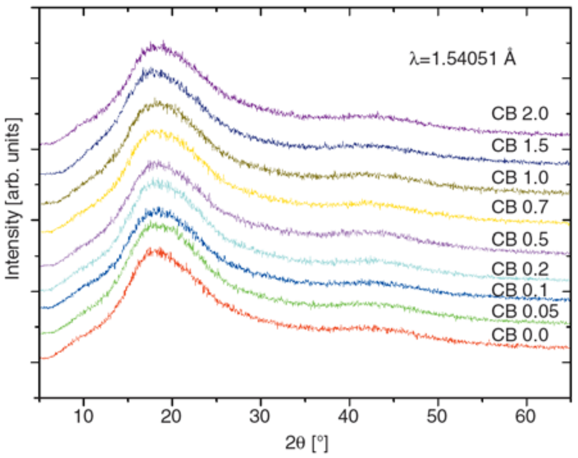

Figure 1. Wide angle X-ray diffraction patterns of DGEBA/TETA/CB nanocomposites

3.2. Mechanical properties

In the DGEBA/TETA/CB system, the components of the dynamic modulus and T_g are examined in two distinguished curing conditions (a: 60°C for 20 h stage 1 and b: 150°C for 2 h stage 2) as a function of the filler content.

Typical traces for the DMA of the unfilled resin and filled composites cured at 60 and 150°C are presented in Figures 2–5.

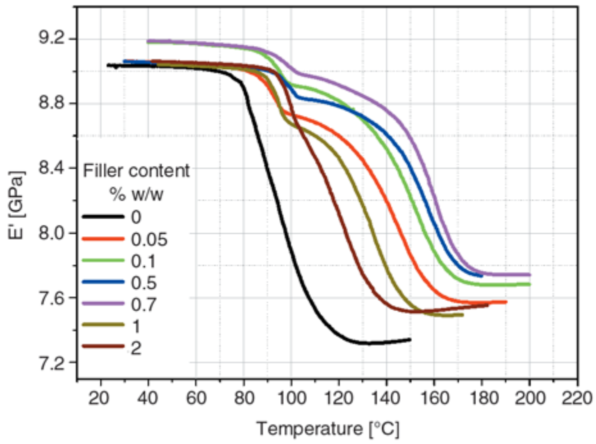

Figure 2. DMA spectra: E' as a function of temperature at frequency of 10 Hz. Curing conditions: 60°C, 20 h (non post-cured)

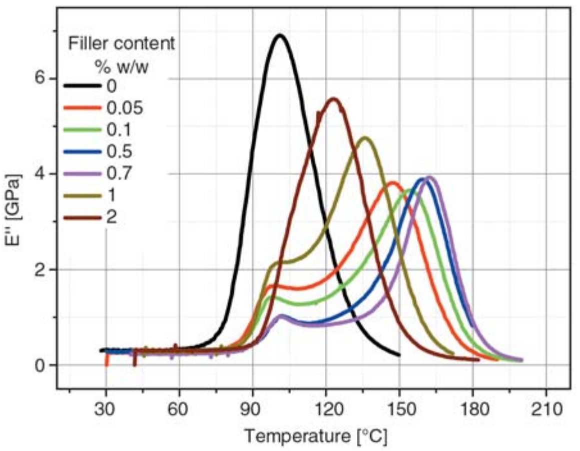

Figure 3. DMA spectra: E'' as a function of temperature at frequency of 10 Hz. Curing conditions: 60°C, 20 h (non post-cured)

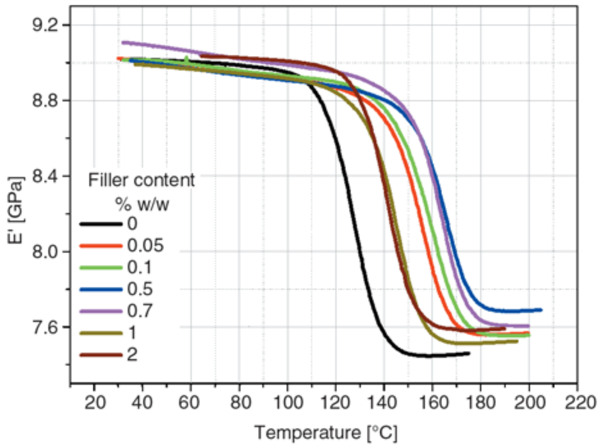

Figure 4. DMA spectra: E' as a function of temperature at frequency of 10 Hz. Curing conditions: 60°C, 20 h and 150°C, 2 h (post-cured)

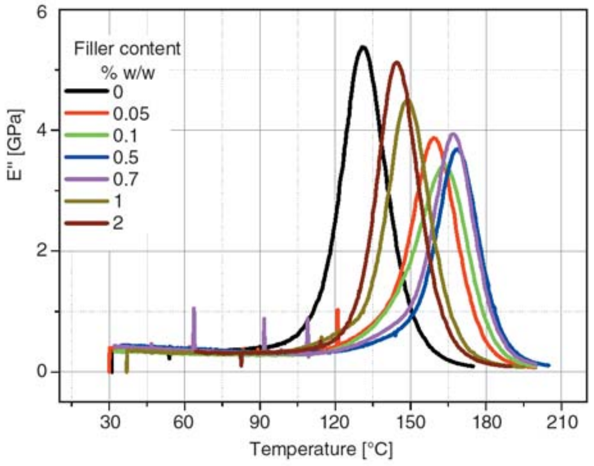

Figure 5. DMA spectra : E'' as a function of temperature at frequency 10 Hz. Curing conditions: 60°C, 20 h and 150°C, 2 h (post-cured)

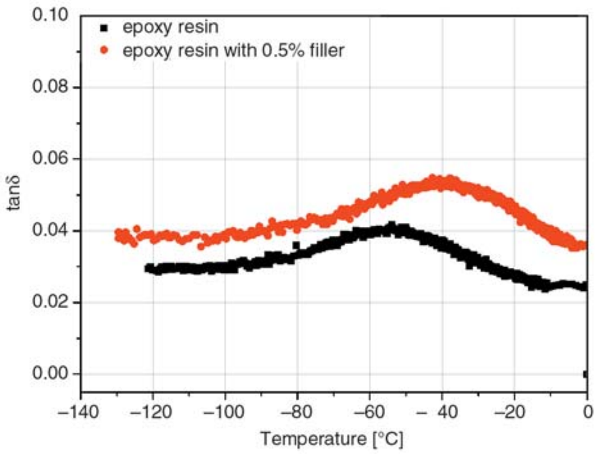

Figure 6. Low temperature DMA spectra: tanδ as a function of temperature at frequency 10 Hz for pure resin and resin nanocomposite with 0.5% w/w CB

As it is clearly shown, E' is slightly affected by the filler content in the glassy state and increases significantly in the rubbery one. The T_g, which was determined as the temperature of tanδ peak, increases with the curing temperature (for the pure epoxy T_g increases from 101°C up to the ultimate post-curing value of 131°C) due to further crosslinking of unreacted epoxy with the TETA amine groups. Also an additional relaxation is observed in the partially cured nanocomposites which will be discussed later.

Raw data of tanδ for the pure resin and the nanocomposite with 0.5% CB content at subzero temperatures are shown in Figure 6. There is a small peak in tanδ at about –55°C which corresponds to the secondary β-relaxation [23–25]. This peak shifts to higher temperatures (around –40°C) in the nanocomposite. Such a behavior is in agreement with dielectric relaxation spectroscopy results which are presented below and perhaps is an evidence for different curing procedure in the pure epoxy and in the nanocomposites.

3.3. Effect of curing procedure and filler content on T_g

The T_g dependence on the CB-content is presented in Figure 7 for the two distinctly different curing conditions (60°C, 20 h and 150°C, 2 h).

In both cases, at low filler contents, T_g increases up to a maximum value (at about 0.7% w/w) of filler content, and afterwards decreases. This dependence is similar in both groups of samples (before and

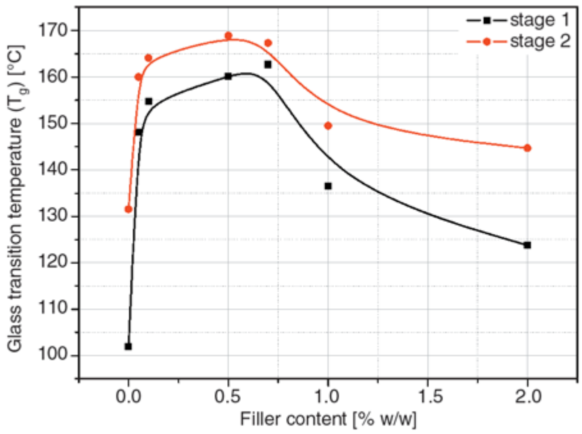

Figure 7. The dependence of T_g as a function of filler content at curing conditions (stage 1): 60°C, 20 h and (stage 2): 60°C for 20 h plus 150°C, 2 h

Table 2. Glass transition Temperatures for sub(T_{gs})- and post(T_{gp})-cured states

Filler content [wt%]	0.0	0.05	0.1	0.5	0.7	1.0	2.0
T_{gs} [°C]	102	110	115	160	142	137	124
T_{gp} [°C]	132	136	137	169	154	149	145
ΔT_g [°C]	30	26	22	9	12	17	21

after post-curing) and is confirmed also by DSC measurements. In Table 2 the glass transition temperatures for sub(T_{gs})- and post(T_{gp})-cured states and the difference $T_{gp} – T_{gs}$ are presented.

This unexpected behavior shows a remarkable difference with the predictions of the statistical theory available for randomly dispersed and distributed fillers. A similar behaviour was observed in poly(vinyl alcohol)/clay nanocomposites [26]. It can be qualitatively explained by the coexistence of the two mechanisms (namely interfacial constrains and free volume increase [20]) which can be responsible for the T_g shifting. In any nanocomposite the two mechanisms are in dynamic equilibrium. The equilibrium point depends on many factors (filler's amount, size, etc.) and in that way it analogically affects the T_g.

According to the first mechanism, a short-range, highly immobilized layer of a few nm thick is developed near the surface of the fillers. In this interaction region of the polymer layer surrounding the particles, the conformational entropy and the chains kinetics are significantly altered. As the filler content increases the volume fraction of the interaction region in the nanocomposites increases too. The polymer chains in this region are under constrain because of the interfacial polymer-particle interactions and therefore T_g of the nanocomposites has been shifted to higher temperatures.

Based on the concept of free volume, the increase of the filler content increases the free volume due to loosened molecular packing of the chains. This extra created free volume assists the large-scale segmental motion of the polymer. As a result, T_g of the nanocomposites decreases as the filler loading increases.

In our case, at low filler content the first mechanism (interfacial constrains) dominates and therefore contributes to a T_g increase with the filler loading. After a certain amount of filler (0.7% w/w) the second mechanism (free volume increase) stars to be dominant and the T_g decreases with the filler content.

This inversion in the domination of the mechanisms which are responsible to T_g shifting could be explained as a consequence of a transition of the filler arrangement within the matrix. The critical value of CB content separates, in fact, a dispersed and an agglomerated state and can therefore not be compared with the one obtained through a purely random geometrical process. The CB particles have permanent electrical charges at their surfaces, which are probably responsible for this morphological structure.

3.4. The new sub-T_g

As it is clearly shown in Figures 2 to 5 an additional relaxation is observed (a peak below and close to T_g and in the same temperature as for the pure resin) in the partially cured nanocomposites. This indicates the existence of two crosslinking mechanisms which act in these stages of curing. The first mechanism is caused by the reaction of the crosslink agent with the epoxy groups and the second one appears as a result of the filler's effect on the curing reaction, giving in that way the dominated α-relaxation.

The presence of this new relaxation in the subcured samples (60°C curing temperature) indicates that a formation of a resin-filler interphase takes place just before the full curing procedure is completed.

The development of short-range, highly immobilized layer near the surface of the filler with a thickness of about 2 nm has been reported in these systems [5–7]. In this interaction region of the polymer layer which surrounds the particles, the conformational entropy and chain kinetics are significantly altered [5]. Due to the small size of the filler particle, the filler-matrix interphase is rapidly increased with filler content. This becomes the basis for potentially remarkable changes in the nanocomposite properties. In the post-cured composites the crosslink density increases tremendously, the interphase region reduces significantly and the sub-T_g relaxation disappears. Perhaps this could be attributed to the incorporation of the loose chains into the network.

3.5. The DRS and conductivity measurements

Molded samples of the DGEBA/TETA/CB system cured at 60°C for 20 h (non post-cured) were used for dielectric measurements. The samples were scanned in the DRS at room temperature in the frequency region from 10^{-2} to 10^6 Hz. The data were analyzed in terms of real part of dielectric permittivity (constant) ε', imaginary part of dielectric permittivity (dielectric loss) ε'' and ac electrical conductivity σ. At low filler content, below 1% w/w, $\varepsilon'(f)$ increases moderately in the composites with respect to the pure matrix (results shown in the inset to Figure 8). It is interesting to note that in this group of composites ε' decreases systematically with increasing filler content. This decrease is in very good agreement with the increase of the glass transition temperature T_g with increasing filler content in Table 2. Bearing in mind that $\varepsilon'(f)$ reflects the ability of molecular dipoles connected with the polymer chains for reorientation in the applied electric field, i.e. molecular mobility [27], these results can be understood as follows. With increasing filler content, molecular mobility in the composites decreases as a result of polymer-filler interactions. The decrease of molecular mobility is reflected as an increase of T_g in DSC and DMA measurements and as a concomitant decrease of $\varepsilon'(f)$ in DRS measurements. This explanation does not apply for the pure matrix, which exhibits the lowest $\varepsilon'(f)$ values and at the same time the lowest T_g (Table 2). Similar to other results reported above, by comparing data for the pure matrix with those for the composites we should keep in mind that curing in the composites occurs in the presence of the filler, i.e. curing conditions are different in the two cases. At higher filler contents, starting with 1%, a significant increase of $\varepsilon'(f)$ is observed in Figure 8. The origin of that increase will be discussed in relation to $\varepsilon''(f)$.

Experimental data of the imaginary part of the dielectric constant ε'' vs. frequency at room temperature are shown in Figure 9. In the first group of samples (pure matrix and composites with less than 1% CB) a relaxation (loss peak) is observed at about 10^5 Hz. Comparison with data in the literature indicates that this is the β-relaxation attributed to the crankshaft rotation of the hydroxyether group [–CH_2–CH(OH)–CH_2–O–] generated by the reaction between epoxide and amino groups [2, 7, 16]. In the second group of composites, those with higher filler content, starting with 1%, an overall and significant increase of $\varepsilon''(f)$ is observed. As a

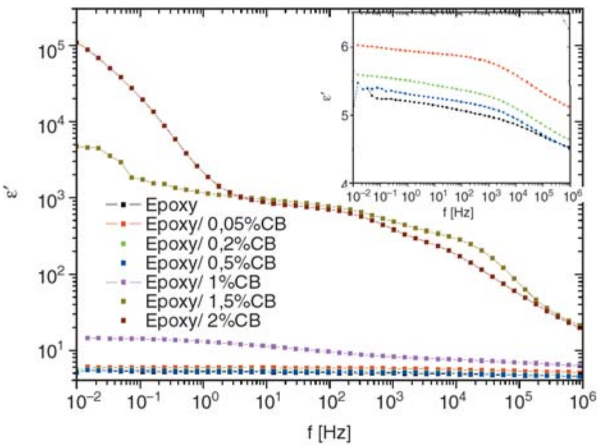

Figure 8. Real part of the dielectric permittivity (ε') versus frequency f at room temperature for the samples indicated on the plot. The inset shows details for the samples with low filler content

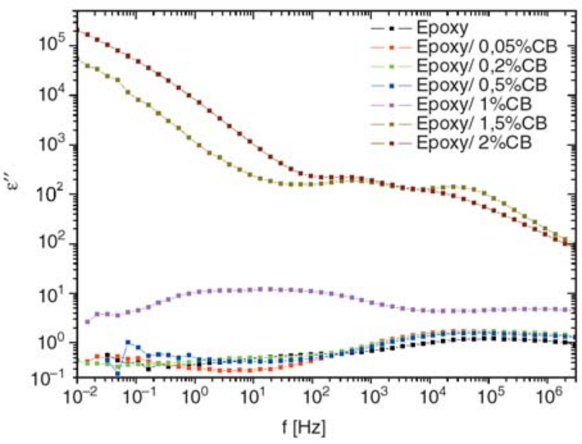

Figure 9. Imaginary part of the dielectric permittivity (ε'') versus frequency f at room temperature for the samples indicated on the plot

result, the β-relaxation is masked and can no more be followed. Please note the high values of $\varepsilon'(f)$ for the same group of composites in Figure 8. In agreement with data reported for similar systems in the literature [7, 16], the large increase of both $\varepsilon'(f)$ in Figure 8 and $\varepsilon''(f)$ in Figure 9 is to a large extent related to the formation of a percolation structure of the nanoparticles, as confirmed by conductivity data in Figure 10 to be discussed later. Please note that the percolation structure, related with the formation of agglomerates in the bulk composite, is reflected also in the CB content dependence of the glass transition temperature T_g discussed in Section 3.3.

In addition to the overall increase of $\varepsilon'(f)$ and $\varepsilon''(f)$ in the composites with high CB content, a broad and complex relaxation is observed between 1 and 100 Hz for the sample with 1% CB content, which is shifted to higher frequencies at higher CB content. We think that this is Maxwell–Wagner–Sillars (MWS) relaxation, associated with the formation of agglomerates of CB [16]. It is reasonable to assume a broad distribution of size and conductivity of these agglomerates, which give rise to the broad and complex MWS relaxation observed. It is interesting to note that, as pointed out by one of the referees, $\varepsilon'(f)$ goes to saturation at low frequencies for the sample with 1% CB, this result providing support for the attribution of the relaxation to MWS polarization. The same is true for the samples with higher CB content. The further increase of $\varepsilon'(f)$ in these samples at even lower frequencies is attributed to space charge polarization [28].

Figures 10 and 11 show results for the electrical ac conductivity σ calculated from the measured dielectric loss $\varepsilon'(f)$ by using Equation (3). A typical dielectric behavior is observed below 1% CB (conductivity increases linearly with the frequency). At higher CB contents conductivity increases significantly and plateau values are observed at low frequencies for the composites with 1.5 and 2% CB. In consistency with the dielectric data presented in Figures 8 and 9 and discussed above, the large increase of conductivity in these samples is attributed to the formation of a percolation structure. Thus, the results suggest that in the system under investigation the percolation threshold is between 1.0 and 1.5 wt% CB. A final comment refers to the relatively low values of both the percolation threshold and the dc conductivity of the composites under investigation (dc conductivity 10^{-9} to 10^{-8} S/cm for the composite with 2 wt% CB), as compared to metal/polymer composites [29]. Please note, however, that similar values to those of the present work were reported in the past and recently [30] for various CB/polymer composites.

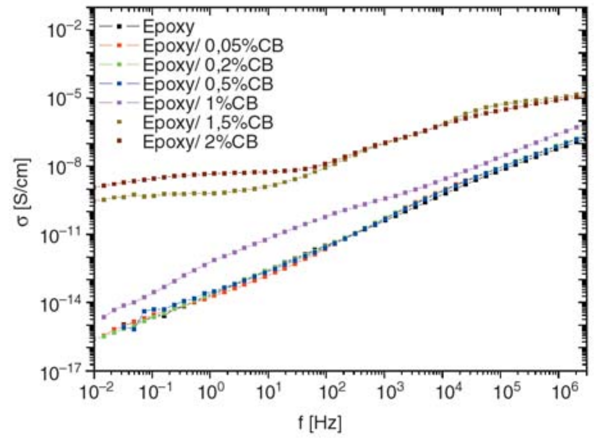

Figure 10. Electical conductivity (σ) versus frequency *f* at room temperature for the samples indicated on the plot

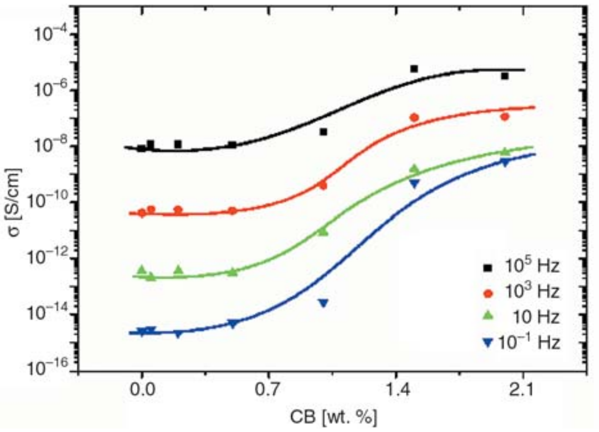

Figure 11. Electrical conductivity (σ) as a function of nanoparticle content at different frequencies indicated on the plot. The lines are guides for the eye

4. Conclusions

The dielectric and dynamic mechanical behaviour of epoxy/carbon black composite was systematically investigated. WAXD patterns show the existence of small, about 8 Å in size, orientated regions which are consistent with the close alignment of the epoxy elements of the matrix which occurs when the bis phenol groups are able to close pack.

The dependence of T_g on the filler content shows a peculiar behaviour. An increase up to a maximum, corresponding to about 0.7% w/w of CB, followed by a decrease, with the appearance of a new relaxation below and close to T_g in the sub-cured samples is observed. The shift of the β-relaxation (associated to the crankshaft rotation of the hydroxyether group) to higher temperature is an evidence for different curing between the pure epoxy and the nanocomposites.

The increase of the high temperature modulus (rubbery state) as the filler content increases indicates that the CB acts as classical filler and that the polymer interacts with the filler particles. The lack of significant increase in the low temperature modulus (glassy state) with the filler content is unexpected. This partially could be attributed to high degree of crosslink density of the matrix which covers the filler contribution.

The low dielectric constant below the filler content of 1% w/w indicates clearly that no cluster formation takes place and this filler content separates, in fact, the dispersed and the agglomerated state of nanoparticles.

A correlation between conductivity and glass transition behavior in epoxy resin based nanocomposites is observed.

Acknowledgements

This work has been funded by the projects 'Archimedes' and 'PENED'. PENED is co financed 75% of public expenditure through EC – European Social Fund, 25% of public expenditure through Ministry of Development – General Secretariat of Research and Technology and through private sector, under measure 8.3 of OPERATIONAL PROGRAMME 'COMPETITIVENESS' in the 3rd Community Support Programme. Acknowledgements are also expressed to Professor R. A. Pethrick for the stimulating discussions during this work and to student Vangelis Varsamidis for his contribution to sample preparation.

References

[1] Sun Y., Zhang Z., Moon K-S., Wong C. P.: Glass transition and relaxation behavior of epoxy nanocomposites. Journal of Polymer Science, Part B: Polymer Physics, **42**, 3849–3858 (2004).

[2] Brown J., Rhoney I., Pethrick R. A.: Epoxy resin based Nanocomposites: 1. Diglycidilether of bisphenol A (DGEBA) with triethylenetetramine (TETA). Polymer International, **53**, 2130–2137 (2004).

[3] Cao Y. M., Sun J., Yu D. H.: Preparation and properties of nano-Al_2O_3 particles/ polyester/epoxy resin ternary composites. Journal of Applied Polymer Science, **83**, 70–77 (2002).

[4] Pham J. Q., Mitchell C. A., Bahr J. L., Tour J. M., Krishanamoorti R., Green P. F.: Glass transition of polymer/single-walled carbon nanotube composite films. Journal of Polymer Science, Part B: Polymer Physics, **41**, 3339–3345 (2003).

[5] Ash B. J., Schadler L. S., Siegel R. W.: Glass transition behavior of alumina/polymethylmethacrylate nanocomposites. Materials Letters, **55**, 83–87 (2002).

[6] Xiong M., Gu G., You B., Wu L.: Preparation and characterization of poly(styrene butylacrylate) latex/ nano-ZnO nanocomposites. Journal of Applied Polymer Science, **90**, 1923–1931 (2003).

[7] Kotsilkova R., Fragiadakis D., Pissis P.: Reinforcement effect of carbon nanofillers in an epoxy resin system: Rheology, molecular dynamics, and mechanical studies. Journal of Polymer Science, Part B: Polymer Physics, **43**, 522–533 (2005).

[8] Pelster R., Simon U.: Nanodispersions of conducting particles: Preparation, microstructure and dielectric properties. Colloid and Polymer Science, **277**, 2–14 (1999).

[9] Krishnamoorti R., Giannelis E. P.: Rheology of end-tethered polymer layered silicate nanocomposites. Macromolecules, **30**, 4097–4102 (1997).

[10] Reynaud E., Jouen T., Gauthier C., Vigier G., Varlet J.: Nanofillers in polymeric matrix: A study on silica reinforced PA6. Polymer, **42**, 8759–8768 (2001).

[11] Berriot J., Montes H., Lequeux F., Long D., Sotta P.: Evidence for the shift of the glass transition near the particles in silica-filled elastomers. Macromolecules, **35**, 9756–9762 (2002).

[12] Arrighi V., McEwen I. J., Qian H., Serrano Prieto M. B.: The glass transition and interfacial layer in styrene-butadiene rubber containing silica nanofiller. Polymer, **44**, 6259–6266 (2003).

[13] Psarras G. C., Gatos K. G., Karahaliou P. K., Georga S. N., Krontiras C. A., Karger-Kocsis J.: Relaxation phenomena in rubber/layered silicate nanocomposites. Express Polymer Letters, **1**, 837–845 (2007).

[14] Zhou Y. X., Wu P. X., Cheng Z-Y., Ingram J., Jeelani S.: Improvement in electrical, thermal and mechanical properties of epoxy by filling carbon nanotube. Express Polymer Letters, **2**, 40–48 (2008).

[15] Bajpai A. K., Bajpai J., Soni S. N.: Preparation and characterization of electrically conductive composites of poly(vinyl alcohol)-g-poly(acrylic acid) hydrogels impregnated with polyaniline (PANI). Express Polymer Letters, **2**, 26–39 (2008).

[16] Pissis P., Fragiadakis D.: Dielectric studies of segmental dynamics in epoxy nanocomposites. Journal of Macromolecular Science: Physics, **46**, 119–136 (2007).

[17] Markov A., Fiedler B., Schulte K.: Electrical conductivity of carbon black/fibres filled glass-fibre-reinforced thermoplastic composites. Composites, Part A: Applied Science and Manufacturing, **37**, 1390–1395 (2006).

[18] Guinier A.: X-ray diffraction in crystalls, imperfect crystals and amorphous bodies. W. H. Freeman and Company, San Francisco (1963).

[19] Krishnamoorti R., Vaia R., Giannelis E.: Structure and dynamics of polymer-layered silicate nanocomposites. Chemistry of Materials, **8**, 1728–1734 (1996).

[20] Bershtein V. A., Egorova L. M., Yakushev P. N., Pissis P., Sysel P., Brozova L.: Molecular dynamics in nanostructured polyimide-silica hybrid materials and their thermal stability. Journal of Polymer Science, Part B: Polymer Physics, **40**, 1056–1069 (2002).

[21] Kanapitsas A., Pissis P., Kotsilkova R.: Dielectric studies of molecular mobility and phase morphology in polymer-layered silicate nanocomposites. Journal of Non-crystalline Solids, **305**, 204–211 (2002).

[22] Pissis P., Kanapitsas A., Georgoussis G., Bershtein V. A., Sysel P.: Dielectric studies of phase morphology and molecular mobility in novel nanocomposites based on polyimide. Advanced Composites Letters, **11**, 49–58 (2002).

[23] Delides C. G., Hayward D., Pethrick R. A., Vatalis A. S.: Real time dielectric investigations of phase separation and cure in rubber modified epoxy resin systems. European Polymer Journal, **28**, 505–512 (1992).

[24] Delides C. G., Hayward D., Pethrick R. A., Vatalis A. S.: Dielectric and morphological investigations of phase separation and cure in rubber-modified epoxy resins: Comparison between teta- and DDM-based systems. Journal of Applied Polymer Science, **47**, 2037–2051 (1993).

[25] Delides C. G., Vatalis A. S., Pissis P., Pethrick R. A.: Dielectric and thermally stimulated discharge current studies of rubber-modified epoxy resins. Journal of Macromolecular Science: Physics, **32**, 261–274 (1993).

[26] Bandi S., Schiraldi D. A.: Glass transition behavior of clay aerogel/poly(vinyl alcohol) composites. Macromolecules, **39**, 6537–6545 (2006).

[27] Runt J. P., Fitzgerald J. J.: Dielectric spectroscopy of polymeric materials. American Chemical Society, Washington (1997).

[28] Kyritsis A., Pissis P., Grammatikakis J.: Dielectric relaxation spectroscopy in poly(hydroxyethyl acrylate)/water hydrogels. Journal of Polymer Science, Part B: Polymer Physics, **33**, 1737–1750 (1995).

[29] Mamunya Y. P., Davydenko V. V., Pissis P., Lebedev E. V.: Electrical and thermal conductivity of polymers filled with metal powders. European Polymer Journal, **38**, 1887–1897 (2002).

[30] Koysuren O., Yesil S., Bayram G.: Effect of composite preparation techniques on electrical and mechanical properties and morphology of nylon 6 based conductive polymer composites. Journal of Applied Polymer Science, **102**, 2520–2526 (2006).

eXPRESS Polymer Letters Vol.2, No.5 (2008) 373–381
Available online at www.expresspolymlett.com
DOI: 10.3144/expresspolymlett.2008.44

Relaxation dynamics of carboxylated nitrile rubber filled with organomodified nanoclay

J. Fritzsche[1], *A. Das*[2], *R. Jurk*[2], *K. W. Stöckelhuber*[2], *G. Heinrich*[2], *M. Klüppel*[1]*

[1]Deutsches Institut für Kautschuktechnologie e.V., Eupener Straße 33, D-30519 Hannover, Germany
[2]Leibniz-Institut für Polymerforschung Dresden e.V., Hohe Straße 6, D-01069 Dresden, Germany

Received 28 January 2008; accepted in revised form 3 April 2008

Abstract. In order to improve the physical properties of elastomers and to get more insight into the polymer dynamics close to filler interphases a carboxylated nitrile rubber (XNBR) was filled with up to 10 phr of layered silicate and investigated by dielectric and dynamic-mechanical analysis as well as by IR spectroscopy. Three relaxation processes have been detected beside the electrode polarization effect obtained in dielectric measurements. The relaxation process at low temperatures can be assigned to the β-process due to the rotational motion of side groups. Its temperature dependence follows an Arrhenius-like behaviour and there is no significant change in the shape of this process with the incorporation of filler. The glass transition at medium temperature shows a Vogel-Fulcher-dependence but seems to be independent of filler as well. At higher temperatures a new relaxation process was detected which is probably due to the formation of zinc-carboxyl-clusters. In dielectric and dynamic-mechanical measurements this process increases with increasing loading of organoclay and is shifted to higher temperature.

Keywords: *nanocomposites, layered silicate, dielectric spectroscopy, relaxation dynamics, dynamic-mechanical spectroscopy*

1. Introduction

Recently, reinforcement of polymers with nanostructured fillers became more and more important. Comparing with traditional fillers like silica and carbon black the physical properties of elastomers are improved due to the fine dispersion and pronounced flocculation of nanoscopic filler particles. However, dispersion of nano-particles in a polymer matrix can be problematic in the case of strong polar bonding between the filler particles, especially for non-polar rubbers. In particular, the application of precipitated silica in high performance tires became a successful technology only after the dispersion problem was solved by coating the silica with a bifunctional silane in a specific complicated multi-step procedure. In addition to nano-scale silica the incorporation of layered silicate into the polymer matrix is a field of intensive research. In the literature an extensive variety of reports can be found describing the improvement effects concerning for instance mechanical and tribological properties [1–3] as well as thermal and chemical stability [4, 5]. Due to the intercalation and exfoliation of organolayered silicate and consequently a large increase in the active surface of the filler the low concentration of clay is one of the most important aspects of rubber layered silicate nanocomposites. The effect of reinforcement mainly depends on the degree of dispersion of the inorganic and polar clay in the organic and in most cases non polar polymer matrix. The dispersion of these particles from its staged layer conformation with individual

---

*Corresponding author, e-mail: Manfred.Klueppel@DIKautschuk.de

mono layer into rubber matrix with poor surface energy is experimentally difficult [6]. This factor is predominantly noticeable for the case of non polar rubber like EPDM (Ethylene Propylene Diene Rubber), NR (Natural rubber) and SBR (Styrene Butadiene Rubber). For this reason a polar rubber like carboxylated nitrile rubber was chosen for insuring a reasonable interaction between organoclay and polymer. In a separate paper we describe the physical properties, XRD-data and filler distribution of layered silicate in carboxylated nitrile rubber [17]. In this present work especially the polymer-filler interaction has been investigated using dielectric and dynamic-mechanical analysis as well as IR-spectroscopy.

2. Experimental

2.1. Sample preparation

The samples have been prepared with the carboxylated nitrile rubber (Krynac 7.40, ML 1+4[at 100°C] 38±4, acrylonitrile content 26.5, carboxylic acid content 7%, Lanxess, Germany) which was filled with different loadings, in example 0, 2.5, 5, 7.5 and 10 phr, of organomodified layered silicate (organomodified pristine sodium montmorillonite, Cloisite Na$^+$ (Na-MMT) Süd Chemie AG, Germany, containing quaternary ammonium salt as organic modifier, basal spacing of this organoclay is 2.98 nm). 3 phr zinc oxide, 2 phr stearic acid, 2 phr diphenyl-guanidine (DPG), 1,7 phr n-cyclohexyl-2-benzothiazole-sulfenamide (CBS) and 1,4 phr soluble sulfur were used as vulcanisation system. The compounds were prepared in a laboratory size mixing mill with a friction ratio of 1:1.2 and using an internal mixer rotating at 50 rpm during 10 min. At first the rubber and organoclay were mixed in the internal mixer at 160°C and then rest of curatives was added at 40°C in the two-roll mill. The curing study was carried out with the help of a moving die rheometer (Scarabaeus V-50) at 160°C. The stocks were cured under pressure at 160°C to 2 mm plates.

2.2. Dielectric broadband spectroscopy

Dielectric investigations have been carried out in a wide temperature range (–100°C to +150°C) and at frequencies from 0.1 Hz to 10 MHz using a broadband dielectric spectrometer BDS 40 (Novocontrol GmbH, Germany). The temperature was varied in five degree steps using the temperature control system Novocool. The temperature uncertainty amounts to ±0.5°C.

The measured geometry was a disc shaped plate capacitor with a diameter of 40 mm. The sample with a thickness of 2 mm was placed between two gold-plated electrodes. To provide a excellent contact between sample and electrodes thin gold layers have been sputtered onto the flat surface of the sample plate. The dielectric permittivity and the dielectric loss have been recorded for each sample in dependence of temperature and frequency.

2.3.Dynamic-mechanical analysis

The dynamic-mechanical measurements were performed in the torsion-rectangular mode with strip specimen of 2 mm thickness on a ARES rheometer (Rheometrix). The dynamic moduli were measured over a wide temperature range (–80 to +80°C) at a frequency of 1 Hz and 0.5% strain amplitude.

2.4. IR-spectroscopy

Infrared spectroscopic studies have been carried out using a Fourier-Transform-Infrared-spectrometer (Thermo Nicolet Nexus). The spectra were obtained using the attenuated total reflectance (ATR) technique with a diamond crystal.

2.5. TEM

For TEM investigations ultra-thin sections were cut by microtome at about –100°C and the images were taken by Libra 120 transmission electron microscope by Zeiss with an acceleration voltage of 200 kV.

3. Results and discussion

3.1. Dielectric investigations

Due to its carboxyl groups and the nitrile content the high polarity of a XNBR provides large values for the dielectric loss ε''. Examples of the results obtained for the dielectric loss ε'' in dependence of temperature and frequency for the unfilled sample and the sample filled with 10 phr organoclay are given in Figure 1.

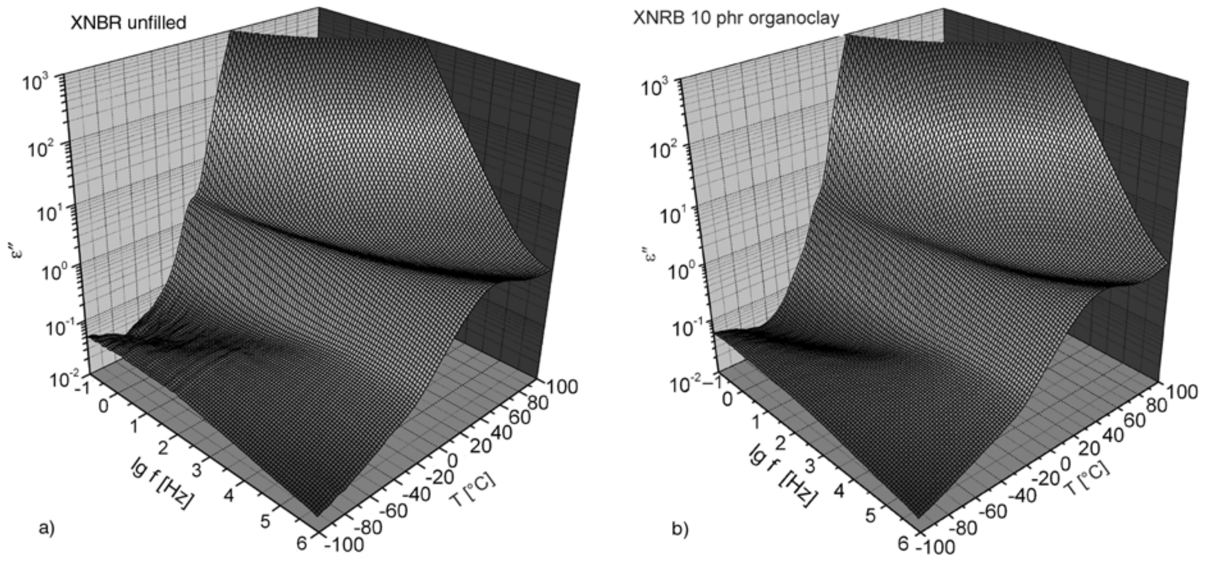

Figure 1. Dielectric loss ε'' in dependence of temperature an frequency for a) the unfilled sample and b) the sample filled with 10 phr of organoclay

In all measurements the glass transition process (α-process) due to the cooperative segmental motion of the chain is observable forming a characteristic temperature and frequency dependent Vogel-Fulcher-behaviour. At low temperatures the Arrhenius-activated β-process can be observed in all samples which is due to local fluctuations of chain segments or side groups. At high temperatures the value of ε'' increases extremely with increasing temperatures probably due to conductivity effects or electrode polarization.

To analyze the high temperature part of the spectra the analyzing procedure developed by Steeman and van Turnhout [7] was applied to the measured data, which has been reviewed by Wübbenhorst and van Turnhout [8]. This method is based on the Kramers-Kronig-relation, one of which is Equation (1), saying that both ε' and ε'' carry the same information about relaxation processes and are related by a Hilbert transformation:

$$\varepsilon''(\omega_0) = \frac{\sigma_{dc}}{\varepsilon_0\omega_0} + \frac{2}{\pi}\int_0^\infty \varepsilon'(\omega)\frac{\omega_0}{\omega^2 - \omega_0^2}\,d\omega \qquad (1)$$

In this procedure the derivation of ε' denoted as ε''_{deriv} (2) is used in order to obtain narrow and sharp peaks and to eliminate conductivity effects due to the independence of ε' from ohmic conductivity:

$$\varepsilon''_{deriv} = -\frac{\pi}{2}\frac{\partial\varepsilon'(\omega)}{\partial\ln\omega} \approx \varepsilon'' \qquad (2)$$

In the case of broad relaxation peaks like those of the α-transition, Equation (2) is almost exact and the derivative reproduces the measured frequency dependent ε'' data. Contrary, for narrow Debye-like processes a peak sharpening is observed and $\varepsilon''_{deriv} \sim \omega^{-2}$ is obtained for large frequencies instead of $\varepsilon'' \sim \omega^{-1}$ [8]. This opens the interesting possibility to get more information about low frequency relaxation processes of dipolar origin, which are often obscured by strong electrode polarization due to ionic conduction. In the XNBR samples under consideration ionic conductance probably results from mobile protons due to the presence of carboxylic groups and other ions obtained from the addition of the processing agents zinc oxide and stearic acid. The blocking of ions at the metallic electrodes leads to the pronounced relaxation process at high temperatures and low frequencies observed in Figure 1. This electrode polarization refers typically to a sharp Debye-like processes and therefore the application of the derivative considered in Equation (2) is expected to sharpen this undesired peak. As a consequence, other processes of dipolar origin may become visible in the spectrum.

The spectrum of the XNBR sample filled with 10 phr is shown in Figure 2 after applying the derivative method Equation (2). Interestingly, the resulting spectra now show an additional relaxation process at higher temperatures in all investigated samples, which obviously was obscured in the orig-

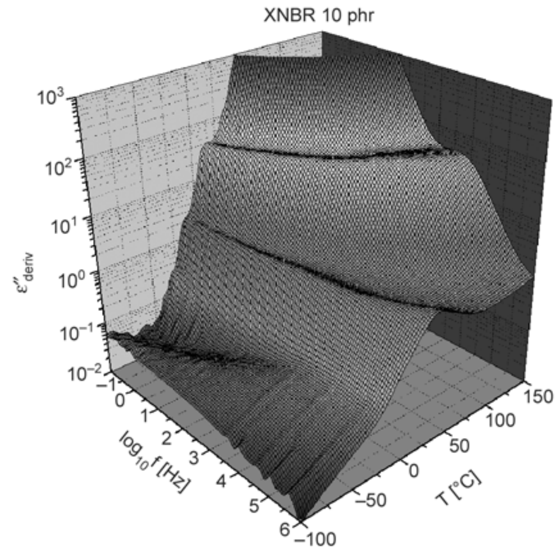

Figure 2. Representation of ε''_{deriv} in dependence of temperature and frequency after applying the analyzing procedure Equation (2) for the XNBR filled with 10 phr organoclay [7, 8]

inal spectra by the strong electrode polarization. Though this process is still partly covered by electrode polarization its location and activation behavior can be evaluated. A plot of ε''_{deriv} against temperature at 0.5 kHz given in Figure 3 shows an increase of the dielectric loss with increasing content of organoclay. Additionally a reasonable shift to higher temperatures of this process from the unfilled sample to the filled samples is detectable. This shifting indicates the assumption of different processes in the unfilled and the filled samples.

To investigate the activation energies of these processes as well as the relaxation process parameters like dielectric strength, relaxation rate and shape parameters the obtained data have been analyzed using the fitting program WINFIT (Novocontrol, Germany).

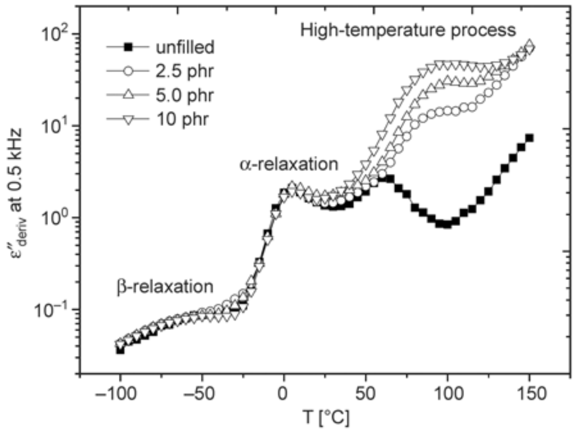

Figure 3. Plot of ε''_{deriv} against temperature at 0.5 kHz for all investigated samples

The Cole-Cole-plot of dielectric loss against the dielectric permittivity shows symmetric semicircles, hence the fits have been carried out using Cole-Cole-functions (3) to describe symmetrical but broadened relaxation processes with respect to the Debye model:

$$\varepsilon^{*}_{CC} = \varepsilon_{\infty} + \frac{\Delta\varepsilon}{1+(i\omega\tau)^{\alpha}} \tag{3}$$

Here ε_{∞} describes the dielectric permittivity at infinite frequencies, $\Delta\varepsilon$ the dielectric strength and α the broadening parameter. The fitting procedure has been carried out for each temperature and is exemplarily shown in Figure 4 for the unfilled XNBR sample and in Figure 5 for the sample filled with 10 phr organoclay at 298.15 K. Obviously, the low frequency peak, corresponding to the high temperature process in Figure 3 increases significantly with the addition of organoclay and is shifted to lower frequencies. The activation diagram of all XNBR samples is shown in Figure 6. The resulting parameters are shown in Table 1.

The α-processes have been analyzed with a Vogel-Fulcher-Tamman equation (4) resulting in values for the apparent activation energy E_A, the relaxation rate lgf_0 and the Vogel-temperature T_{VF}:

$$f(T) = f_0 \exp\left(\frac{E_A}{k_B(T-T_{VF})}\right) \tag{4}$$

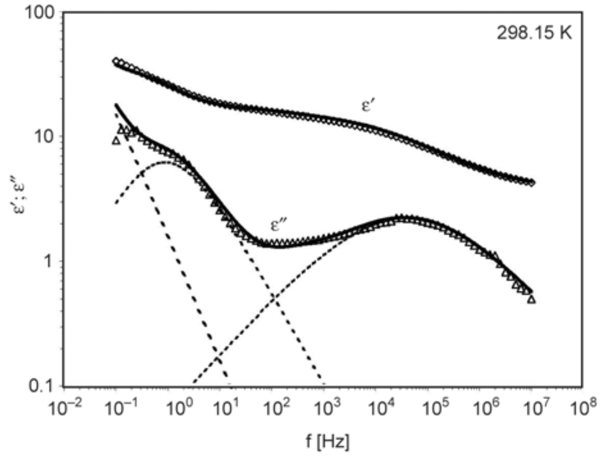

Figure 4. Fitting procedure of ε′ and ε''_{deriv} for the unfilled sample at 298.15 K. Symbols are experimental data, dashed lines are single Cole-Cole functions, solid lines are the resulting fit curves

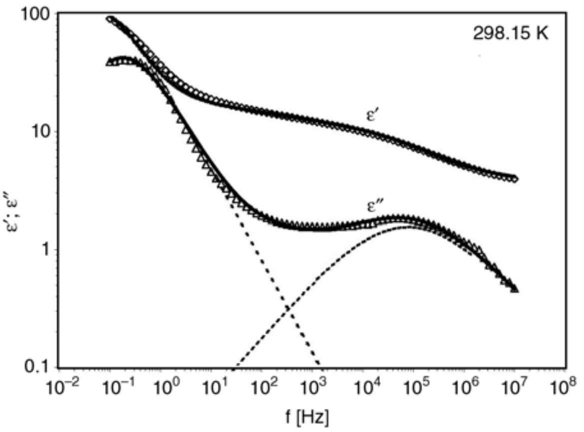

Figure 5. Fitting procedure of ε′ and ε''_{deriv} for the sample filled with 10 phr organoclay at 298.15 K. Symbols are experimental data, dashed lines are single Cole-Cole functions, solid lines are the resulting fit curves

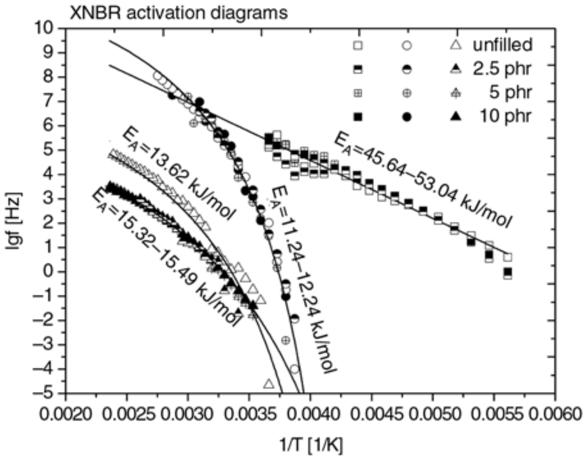

Figure 6. Activation diagram of the XNBR samples after applying the derivation procedure

Table 1. Activation parameters of the XNBR samples for the detected processes

	unfilled	2.5 phr	5 phr	10 phr
	α-process			
lgf_0 [Hz]	12.505	12.505	12.505	12.505
E_A [kJ/mol]	11.84	12.24	11.24	12.21
T_{VF} [K]	217.18	214.13	222.72	223.21
	β-process			
lgf_0 [Hz]	14.12	14.13	15.88	15.25
E_A [kJ/mol]	45.64	46.65	53.04	50.29
	high-temperature process			
lgf_0 [Hz]	8.18	7.75	7.08	6.94
E_A [kJ/mol]	13.62	15.32	15.49	15.44
T_{VF} [K]	210.97	208.77	191.93	188.32

Since the relaxation rate f_0 of the α-process can hardly be fitted, it was set to the constant universal value lgf_0 = 12,5 empirically found for diene rubbers. The activation energies are with 11–12 kJ/mol nearly equivalent. Accordingly the glass transition process seems to be independent of the incorporation of organoclay. The β-process was described by a simple Arrhenius relation. As well the activation energies of the β-process do only show small difference with 45–53 kJ/mol, here the uncertainty is much higher due to the linear behavior.

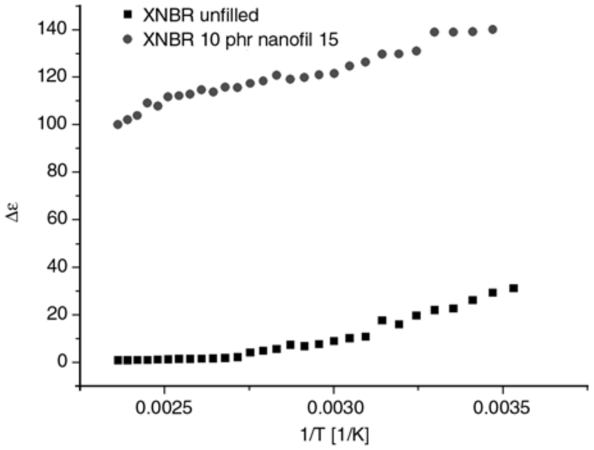

Figure 7. Relaxation strength in dependence of temperature for the high-temperature process of the unfilled sample and the sample filled with 10 phr of organoclay

It is clearly shown that the high-temperature process can be described by the Vogel-Fulcher-Tamman equation. Here the relaxation rate was also a fit parameter. The relaxation rate is decreasing with increasing organoclay content as well the Vogel-Temperature is decreasing. The activation energy for the unfilled sample is 13 kJ/mol, in the filled samples 15 kJ/mol. The difference is not significant, conspicuous is the very small difference among the different filled samples.

The relaxation strength of the high-temperature process investigated for the unfilled sample and the sample filled with 10 phr of organoclay is shown in Figure 7. It is evident that the relaxation strength is extremely higher in case of the filled sample which was as well visible in Figure 3. In both cases the relaxation strength is increasing with decreasing temperature, showing the typical behavior of a dipole based process.

3.2. Dynamic-mechanical investigations

In dynamic-mechanical measurements the tanδ for the unfilled and filled samples are obtained and plotted against the temperature in Figure 8. The glass transition process is detectable at –10°C and

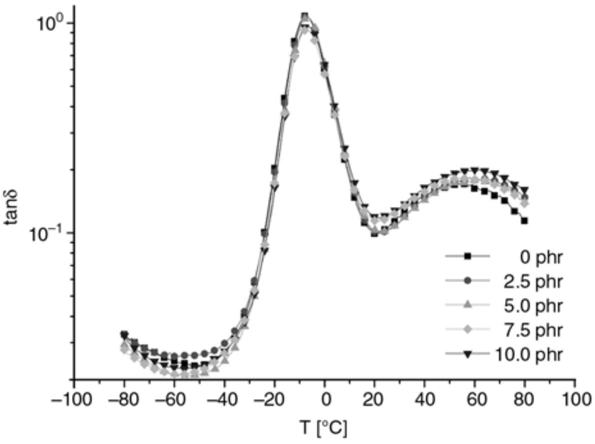

Figure 8. Representation of tanδ vs. temperature of all investigated systems

the tanδ maximum decreases slightly with increasing filler content. An additional relaxation process at high temperatures is also confirmed in dynamic-mechanical investigations but the difference between different amounts of organoclay are not as significant as in dielectric investigations. But like in dielectric measurements a shift to higher temperatures with incorporation of organoclay is detectable.

3.3. TEM

TEM pictures are able to give a direct impression about the distribution of nanoscale filler in the elastomer matrix. Figure 9 shows the sample filled with 5 phr organoclay. Here the silicate layers in the rubber matrix are oriented preferably during the processing. A closer look gives the simultaneous existence of intercalated and exfoliated structures but as well there are still a few agglomerates of staged silicate layers so total exfoliation/intercalation is not achieved through melt processing.

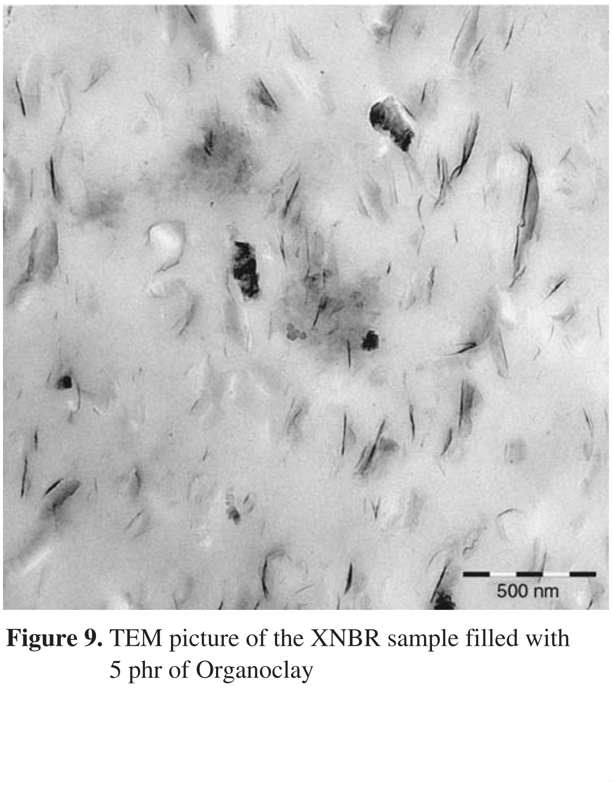

Figure 9. TEM picture of the XNBR sample filled with 5 phr of Organoclay

3.4. Discussion

In literature the process at high temperatures is assigned to a formation of clusters due to the presence of ZnO and carboxylic groups [9–12]. This assumption was proven by IR-spectroscopic studies by Mandal [9] where characteristic peaks for Zn-carboxyle-complexes have been be detected. The results of our IR-investigation are presented in Figure 10 and confirmed the interpretation given in literature.

The IR spectra show two strong peaks around 2925 and 2854 cm^{-1} due to the presence of CH$_2$-groups. Another strong peak around 2237 cm^{-1} is due to the CN-group in the acrylonitrile component. The important part of the spectrum is the range between 1500 and 1700 cm^{-1}, where peaks due to the carboxylic part are responsible for effects of C=O in different chemical environment. There is one peak at 1734 cm^{-1} due to the transesterfication of the monomeric carboxylic acid group. The peak at 1586 cm^{-1} was assigned to carbonyl stretching vibration of zinc carboxylate salt, the peak at 1540 cm^{-1} can be assigned to the hexacoordinated zinc carboxylate multiplet.

The infrared spectra for unfilled and filled specimen do not show a significant difference in the range between 1500 and 1700 cm^{-1}. Accordingly, there seems to be no change of the chemical arrangement.

The high temperature peak of silica filled XNBR has been studied by Mandal *et al.* [10] using dynamic-mechanical measurements. Here, the increase of the relaxation process at high temperatures is accompanied by a shift of the relaxation process to higher temperatures with increasing silica loading. It is assumed that the increase of tanδ in the high temperature relaxation process is due to the interaction of filler particles with the rubber chains in the cluster region.

In our dielectric measurements this interpretation agrees with the increase of the high-temperature relaxation process with increasing amount of

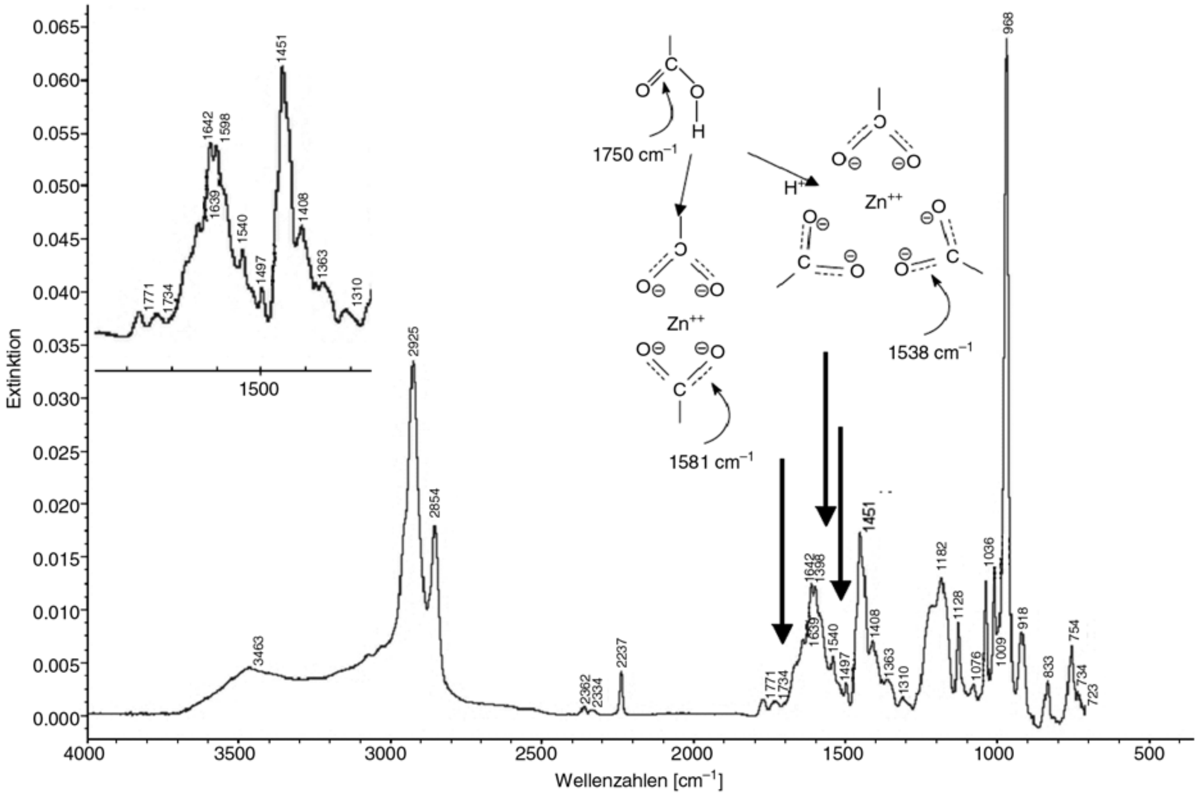

Figure 10. IR-spectrum of the unfilled XNBR sample

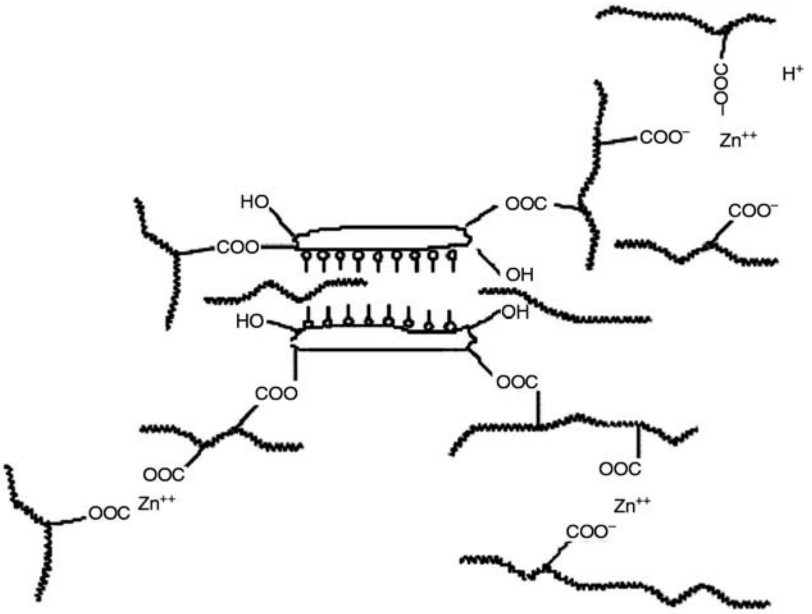

Figure 11. Model of reinforcement of organoclay in XNBR

organoclay and with the shift to higher temperatures. As well, the increase of the activation energy with the incorporation of organoclay seems to support the interpretation given in literature of a reinforcement in the cluster region. In that case the incorporation of layered silicate stabilizes the Zn-carboxyle clusters resulting in the observed effects. This can be the case when a direct bond between the layered silicate and the Zn-Clusters is formed. A possible mechanism of Zn-Cluster-reinforcement is shown in Figure 11. In that case the relaxation process at high temperatures in the filled samples is interpreted as a modification of the Zn-cluster-based process detected in the unfilled sample.

As mentioned above the very small difference in activation energy of the high-temperature process among the different filled samples is conspicuous. With the underlying mechanism mentioned in Figure 11 one would expect an increasing activation energy with increasing organoclay loading. As well, the dynamic-mechanical data do not show the significant shift to higher temperatures as described in the literature for silica filled XNBR.

It is also possible to interpret the process in the filled samples as a separate filler based process which overlaps the process in the unfilled sample. A different process would explain the different activation energy of 15 kJ/mol observed in the filled samples independent of filler content and also the apparently different location of the high temperature peaks for filled and unfilled samples as shown in Figure 3. In the frame of this interpretation the high temperature peak of the filled samples results from the glass transition of the immobilized polymer layer around the filler particles, which is more precisely a glass transition gradient near the filler surface due to attractive polymer-filler interaction [13] as described by several authors.

It was shown that the mobility of chain units adjacent to the filler surface differs considerably from the bulk resulting in an individual glass transition temperature of the interphase [14–16]. Hereby, the influence of this interphase on the macroscopic properties of the sample increases with the amount of filler. These effects are far from being well understood on a microscopic level due to the complex interplay between bulk and interphase. The specific glass transition temperature of the interphase usually lies several degrees above the glass transition temperature of the bulk due to the attractive polymer-filler forces. As well the Vogel-Fulcher-Tamman activation behaviour and the value of the activation energy are not differ significantly from the value of the main glass transition process.

4. Conclusions

In this study the reinforcement effects of organoclay in XNBR have been investigated using dielectric and dynamic-mechanical analysis. Dielectric measurements as well as dynamic-mechanical studies suggest the formation of ionic clusters due to the presence of ZnO. Infrared studies confirmed these assumptions, where peaks due to zinc carboxylate salts or multiplets have been detected. Measurements of dynamic-mechanical properties show only small reinforcement effects in areas away from the cluster region, in the cluster region itself a strong effect is detectable with dielectric measurements. Further investigations dealing with nano-silica [17] and with different kinds of organoclay as filler in XNBR are deemed to be necessary to have a clear understanding about concept and mechanism of elastomer reinforcement by nanoparticles.

Acknowledgements

This work has been supported by the German Federal Ministry of Education and Research (BMBF Grant 03X0002D). Helpful discussions with W. Herrmann (ContiTech AG, Hannover, Germany), C. Schmidt and C. Recker (both Continental AG, Hannover, Germany) and T. Engelhardt (Südchemie AG, Moosburg, Germany) are appreciated.

References

[1] Herrmann W., Uhl C., Heinrich G., Jehnichen D.: Analysis of HNBR-montmorillonite nanocomposites. Morphology, orientation and macroscopic properties. Polymer Bulletin, **57**, 395–405 (2006).

[2] Ganter M., Gronski W., Reichert P., Mülhaupt R.: Rubber nanocomposites: Morphology and mechanical properties of BR and SBR vulcanizates reinforced by organophilic layered silicates. Rubber Chemistry and Technology, **74**, 221–235 (2001).

[3] Tsuruk V. V.: Nanocomposite polymer layer for molecular tribology. Tribology Letters, **10**, 127–132 (2001).

[4] Wang S., Zhang Y., Peng Z., Zhang Y.: New method for preparing polybutadiene rubber/clay composites. Journal of Applied Polymer Science, **98**, 227–237 (2005).

[5] Li W., Huang Y. D., Ahmadi S. J.: Preparation and properties of ethylene-propylene-diene rubber/organomontmorillonite nanocomposites. Journal of Applied Polymer Science, **94**, 440–445 (2004).

[6] Das A., Jurk R., Stöckelhuber K. W., Engelhardt T., Fritzsche J., Klüppel M., Heinrich G.: Nanoalloy based on clays: Intercalated-exfoliated layered silicate in high performance elastomer. Journal of Macromolecular Science, Part A: Pure and Applied Chemistry, **45**, 144–150 (2008).

[7] Steeman P. A. M., van Turnhout J.: A numerical Kramers-Kronig transform for the calculation of dielectric relaxation losses free from ohmic conduction losses. Colloid and Polymer Science, **275**, 106–115 (1997).

[8] Wübbenhorst M., van Turnhout J.: 'Conduction-free' dielectric loss $\sigma\varepsilon/\sigma\ln f$ – A powerful tool for the analysis of strong (ion) conducting dielectric materials. Dielectrics Newsletters, **14**, 1–3 (2000).

[9] Mandal U. K.: Ionic elastomer based on carboxylated nitrile rubber: Infrared spectral analysis. Polymer International, **49**, 1653–1657 (2000).

[10] Mandal U. K., Tripathy D. K., De S. K.: Effect of silica filler on dynamic mechanical properties of ionic elastomer based on carboxylated nitrile rubber. Journal of Applied Polymer Science, **55**, 1185–1191 (1995).

[11] Ibarra L., Marcos-Fernández A., Alzorriz M.: Mechanistic approach to the curing of carboxylated nitrile rubber (XNBR) by zinc peroxide/zinc oxide. Polymer, **43**, 1649–1655 (2002).

[12] Mahaling R. N., Jana G. K., Das C. K., Jeong H., Ha C. S.: Carboxylated nitrile elastomer/filler nanocomposite: Effect of silica nanofiller on thermal, dynamic-mechanical behaviour and interfacial adhesion. Macromolecular Research, **13**, 306–313 (2005).

[13] Berriot J., Montes H., Lequeux F., Long D., Sotta P.: Evidence for the shift of the galss transition near the particles in silica-filled elastomers. Macromolecules, **35**, 9756–9762 (2002).

[14] Soles C. R., Douglas J. F., Wu W-L.: Dynamics of thin polymer films: Recent insights from incoherent neutron scattering. Journal of Polymer Science, Part B: Polymer Physics, **42**, 3218–3234 (2004).

[15] Gagliardi S., Arrighi V., Ferguson R., Telling M. T. F.: Restricted dynamics in polymer-filler systems. Physica B, **301**, 110–114 (2001).

[16] Anastasiadis S. H., Karatasos K., Vlachos G., Manias E., Giannelis E. P.: Nanoscopic-confinement effects on local dynamics. Physcal Review Letters, **84**, 915–918 (2000).

[17] Das A., Jurk R., Stöckelhuber K. W., Majumder P., Engelhardt T., Fritzsche J., Klüppel M., Heinrich G.: Nanocomposites based on layered silicate and carboxylated nitrile rubber: Effect of type of processing on the reinforcement. Polymer Engineering and Science, in press, (2008).

eXPRESS Polymer Letters Vol.2, No.5 (2008) 382–390
Available online at www.expresspolymlett.com
DOI: 10.3144/expresspolymlett.2008.45

Solvent transport through carbon black filled poly(ethylene-co-vinyl acetate) composites

K. Priya Dasan[1]*, *G. Unnikrishnan*[2], *E. Purushothaman*[1]

[1]Department of Chemistry, University of Calicut, Calicut-673635, India
[2]Polymer science and technology laboratory, NITC, Calicut-673601, India

Received 27 January 2008; accepted in revised form 4 April 2008

Abstract. Poly(ethylene-co-vinyl acetate) (EVA) was reinforced with three different types of carbon black viz. semi-reinforcing furnace (SRF), high abrasion furnace (HAF) and intermediate super abrasion furnace (ISAF). The solvent transport by the composites were analyzed using benzene, toluene and xylene as penetrant molecules. The observed cure characteristics and solvent uptake behaviour of the composites has been explained on the basis of particle size of the filler and bound rubber content. The mode of transport in all the cases was found to be anomalous. A sorption-desorption-resorption (S-D-RS) experiment was carried out to study the physical changes in the polymer matrix, associated with the transport of the solvents through the composites.

Keywords: *polymer composites, carbon black, EVA, cure characteristics, diffusion coefficient*

1. Introduction

Molecular transport through polymers has become a subject with a variety of challenges and opportunities for practitioners of chemical engineering and applied chemistry in recent years. The knowledge of the performance of polymers in the environment of hazardous solvents, vapours and temperature is essential for their successful applications as structural engineering materials. The diffusion and permeation properties of polymers play a very major role in designing food packaging materials [1], solvent reservoirs [2], pervaporators [3], controlled release devices [4, 5] etc. In order to examine the suitability of a membrane as a barrier material, it is essential to acquire a thorough understanding of its interactions with liquids and vapours.

The influence of carbon black on solvent transport through elastomer networks has gained the attention of scientists for many years. Guth studied the effect of filler reinforcement in elastomers in detail [6]. Porter [7] studied the degree to which the addition of HAF black reduced the swelling of conventionally vulcanized NR in *n*-decane. De Candia *et al.* [8] investigated the transport properties of networks filled with carbon black, in order to obtain information about rubber-filler interactions. Kwei and Kumins [9] found that the sorption of chloroform by an epoxy resin was lowered by about 70% when 5% filler was added. Anfimova *et al.* [10] reported the equilibrium swelling in benzene of NR vulcanizates having different degrees of crosslinking, filled with technical carbon. The diffusivity and solubility of argon, methane, oxygen, and carbon dioxide in two EPDM based polymers, one formulated with 34 wt% carbon black and the other without carbon black, have been studied by Rutherford *et al.* [11]. A linear relationship was observed between the amount sorbed material and pressure for all gases, indicative of Henry's law behaviour. Choi [12] examined the influence of

---

*Corresponding author, e-mail: kpriyadasan@yahoo.com temperature on the extraction of bound rubber. For both silica and carbon black filled compounds, the bound rubber content was found to increase with increase in filler-rubber content ratio and decrease with increasing extracting temperature. Activation energy for the extraction of the unbound and loosely bound rubbers became higher as the total filler content increased. Many other reports including those from our laboratory exist regarding carbon black-elastomer interaction and their influence on the mechanical and solvent transport properties of black filled elastomers [13–19].

The main goal of the present chapter is to study the effects of three different types of carbon black fillers viz. semi-reinforcing furnace (SRF), high abrasion furnace (HAF) and intermediate super abrasion furnace (ISAF) on the cure and solvent transport properties of EVA. These properties of the composites were evaluated in terms of particles size and loading of filler.

2. Experimental

2.1. Materials

EVA used in the present work is obtained from Polyolefin Industries Limited, Chennai, India. The vulcanizing agent used, dicumyl peroxide (40% active), was of commercial grade. The solvents such as benzene, toluene and xylene were obtained from E. Merck (India) Ltd., Mumbai, India and were of reagent grade (99%). The properties of the solvents are given in Table 1. The carbon black fillers, SRF (N220), HAF (N330) and ISAF (N770) were of commercial grade. The properties of the fillers are given in Table 2.

2.2. Mixing

The mixing of EVA with various ingredients was carried out on a two-roll mixing mill (150 mm × 300 mm) with a friction ratio 1:1.4 as per ASTM D15-627. The EVA granules were sheeted out first and then the mixing was carried out. The amount of curing agent, dicumyl peroxide (DCP), was kept constant (4 phr) for all the mixes. Special attention was taken to attain uniform filler distribution. The loading of the fillers are varied as 10, 20, 30, 40 and 50 phr. The formulation of the mixes are given in Table 3.

Table 1. Properties of the solvents

Solvents	Molecular weight	Density [g/cc]	Boiling point [°C]
Benzene	78.11	0.874	79
Toluene	92.14	0.867	109
Xylene	106.17	0.860	137

Table 2. Properties of carbon black

Carbon black type	Particle size [nm]	DBP absorption [cm^3/g]	Pour density [g/l]
SRF	61–100	0.70	375
HAF	26–30	1.05	375
ISAF	20–25	1.15	345

Table 3. Formulations of EVA/carbon black mixes [phr]

Sample code	Ingredients			
	EVA	SRF	HAF	ISAF
G	100	–	–	–
S10	100	10	–	–
S20	100	20	–	–
S30	100	30	–	–
S40	100	40	–	–
S50	100	50	–	–
H10	100	–	10	–
H20	100	–	20	–
H30	100	–	30	–
H40	100	–	40	–
H50	100	–	50	–
I10	100	–	–	10
I20	100	–	–	20
I30	100	–	–	30
I40	100	–	–	40
I50	100	–	–	50

2.3. Cure characteristics and vulcanization

The cure characteristics were studied by means of an oscillating disc rheometer (Monsanto Rheometer MDR-2000, USA) as per ASTM standard D-5289 (2001). The samples were vulcanized at 160°C using a hydraulic press, having electrically heated platens, under a pressure of 689.4 kPa (mould dimension:150 × 150 × 2 mm^3) to their respective optimum cure time as obtained from the rheographs. Moulds were cooled quickly in water after the curing process. The moulded samples were stored in a cool and dark place for 24 hours.

2.4. Bound rubber content estimation

The bound rubber content was estimated according to the procedure suggested by Leblanc and Hardy [20], using benzene as the solvent. About 1 g of filler loaded non cured EVA sample was cut into small pieces and kept immersed in 150 ml benzene for 72 hours at room temperature. The solvent was filtered off, and the remaining sample was dried for a few hours at room temperature and then for 24 hours under vacuum at 40°C. Complete drying was checked by a constant final weight. Similar methodology has been adopted in many works before [21–24].

The amount of BR (in percentage of initial rubber content of the compound) has been calculated from the Equation (1):

$$\mathrm{BR}\,[\%] = \frac{(M_0 - M_b) - [\mathrm{CPD}/100(M_0 - M_e)]}{(M_0 - M_b)} \cdot 100 \qquad (1)$$

where CPD is the total formulation (in phr); M_0 is the initial weight (bottle + unextracted sample), M_b is the empty bottle weight and M_e is the final weight (bottle + extracted sample) when dried.

2.5. Sorption experiments

The samples for sorption experiments (ASTM D-471) were punched out in circular shape of diameter 1.9 cm and thickness 0.2 cm were dried in a vacuum desiccator over anhydrous $CaCl_2$ at room temperature for about 24 h. The original weights and thicknesses of the samples were measured before sorption experiments. They were then immersed in solvents (15–20 ml) taken in closed diffusion bottles, which were kept at constant temperature in an oven. The samples were removed from the bottles at periodic intervals, dried between filter papers to remove the excess solvent on their surfaces and weighed immediately using an electronic balance (Shimadzu, Libror AEU-210, Japan) that measured reproducibly within ±0.0001 g. They were then placed back into the test bottles. The process was continued until equilibrium swelling was achieved. Since the weighing was done within 40 seconds, the error associated with the evaporation of solvents is negligible. Similar methodology has been adopted by several researchers [25–27]. The experiments were duplicated or triplicated in most cases. The results of the sorption experiments have been expressed as moles of solvent sorbed by 0.1 kg of the sample, Q_t mol%, given by Equation (2). The Q_t values obtained thereby have been plotted as a function of square root of time, to construct the sorption curves.

The thickness and diameter of the samples before and after swelling were determined by using gauge micrometer and vernier calipers respectively.

$$Q_t[\%] = \frac{\left[\dfrac{\text{Weight of solvent sorbed by the sample at a given time}}{\text{Molecular weight of the solvent}}\right]}{\text{Initial weight of the solvent}} \cdot 100 \qquad (2)$$

3. Results and discussion

3.1. Cure characteristics

Figure 1 shows the rheographs of EVA filled with three different types of carbon black at 10 phr filler loading. For all the mixes, the torque increases with time and levels off later. The increase in torque with time is due to the crosslinking of the mixes while the leveling off is an indication of the completion of curing. The maximum torque (M_H) gives an idea about the crosslink density and degree of reinforcement of the filler in the matrix. M_H has been found to be higher for the filled samples compared to pure EVA. The increase in M_H value is due to the increased restriction to polymer chain mobility and viscosity of the mixes caused by filler reinforcement.

Figure 2 shows the M_H values of the mixes at different filler loading. Among the black filled EVA

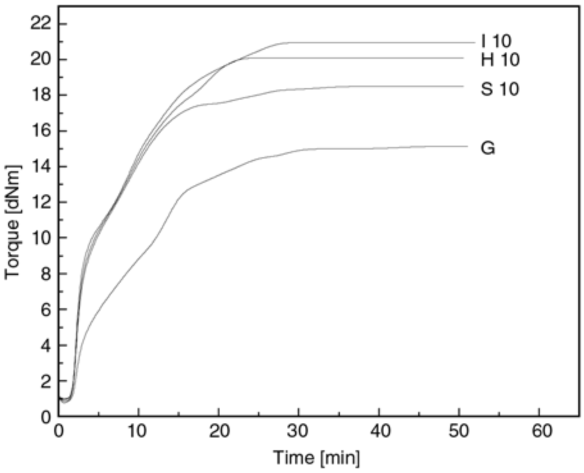

Figure 1. Rheographs of EVA filled with different types of carbon blacks at 10 phr filler loading

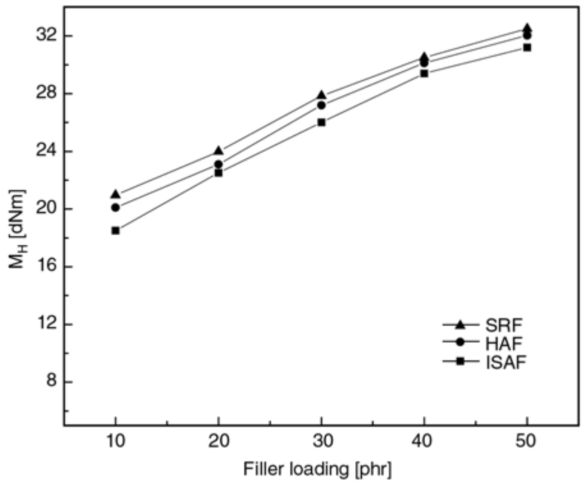

Figure 2. M_H values of EVA/carbon black mixes at different filler content

samples, the ISAF filled sample shows the highest M_H value followed by HAF and then SRF filled mixes for a given loading. This has been attributed to the difference in particle size of the fillers used. For a given loading of the filler, the effective surface area increases with decreasing particle size. As the surface area of the filler increases, the filler-polymer interaction increases resulting in higher degree of reinforcement. Therefore ISAF, having the lowest particle size among the fillers used, shows the maximum reinforcement in the matrix and hence the highest M_H value. SRF having the highest particle size gives the minimum value of M_H, while that of HAF filled samples lies in between.

From Figure 2, it is also clear that the torque value increases with increased filler loading. The increment in torque values with increase in filler content indicates that as more and more fillers get reinforced into the matrix, the mobility of macromolecular chains of EVA gets reduced resulting in more rigid vulcanizates.

3.2. Bound rubber content (BR)

Bound rubber is the rubber portion that can no longer be separated from the filler when a rubber batch is extracted in a good solvent over a specific period of time, usually at room temperature. It is a measure of the interaction between the polymer and the filler [12]. During the milling process, polymer chain molecules become attached to reinforcing fillers. Therefore they are no longer soluble in usual solvents. This process is the basis for the formation of bound rubber. It continues after mixing and eventually a system of interconnecting chains and particles results, which appears as an insoluble fragile gel containing filler and part of the bound rubber.

Table 4. Bound rubber content [%]

Type of filler	Bound rubber content [%]
SRF	42.84
HAF	45.21
ISAF	47.26

Table 4 shows the bound rubber (BR) content of EVA loaded with different carbon blacks. The bound rubber content has been found to be in the order: ISAF > HAF > SRF filled EVA. Bound rubber results in the formation of gel like structures and enhances the bonding between individual polymeric chains. Therefore polymer chain mobility within the matrix is minimum for ISAF loaded samples and maximum for SRF loaded samples.

3.3. Sorption properties

3.3.1. Effect of filler loading

Figures 3 and 4 show the sorption curves of unfilled and carbon black filled EVA at 28°C in benzene and toluene respectively. It can be seen from the figures that the loading of EVA with carbon black reduces the mol% solvent uptake. Vulcanization restrains the long-range movements of the polymer molecules but leaves their local segmental mobility high [28]. Reinforcement restricts these local freedoms of movement and thereby improves the sol-

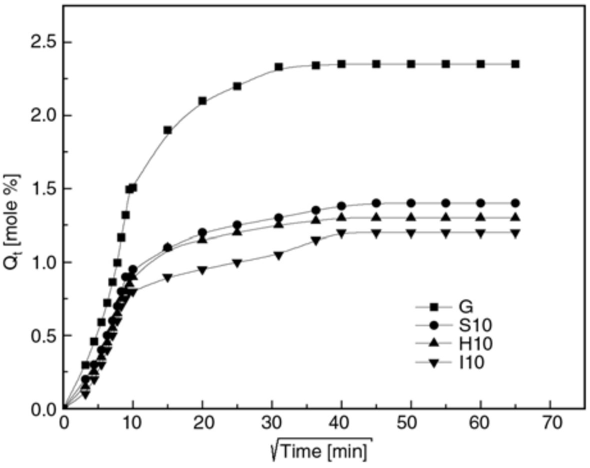

Figure 3. Mol% benzene uptakes by gum EVA and EVA/carbon black composites at 10 phr filler loading

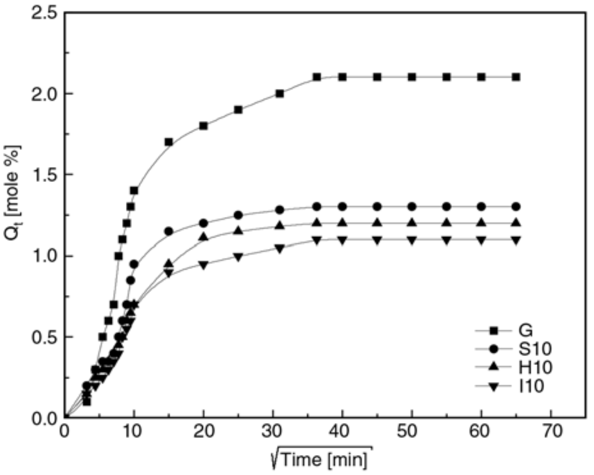

Figure 4. Mol% toluene uptake by EVA and EVA/carbon black composites at 10 phr filler loading

vent resistance. The fillers form chemical as well as physical crosslinks with the polymer chains, because of which the polymer segments in a certain zone around the filler experiences certain immobilization. This complex crosslink clusters prevent the rearrangement of the polymer chains during solvent ingression and reduces the free volume in the composite, thereby causing resistance to the path of penetrants. Figure 5 gives a schematic representation of the filler reinforced polymer matrix.

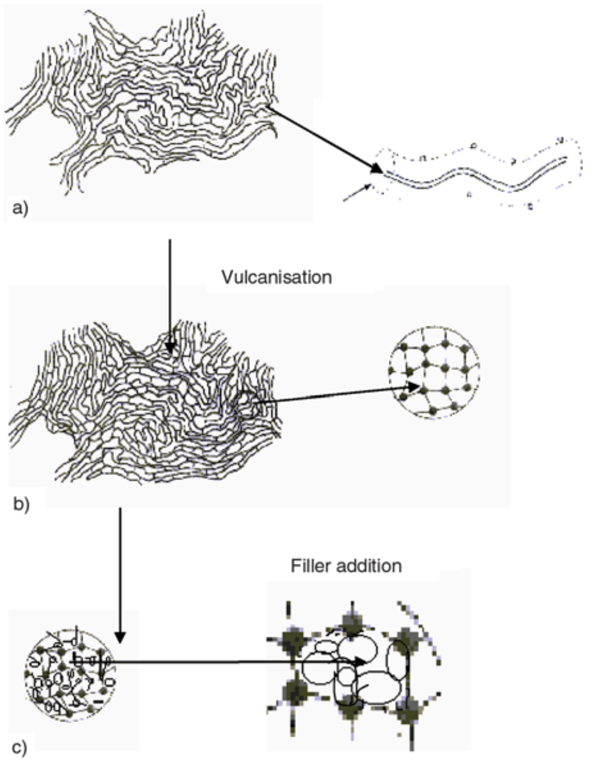

Figure 5. Pictorial representation of (a) unvulcanized polymer, (b) vulcanized polymer, (c) filled polymer

It is also clear from Figures 3 and 4 that EVA loaded with ISAF absorbs the lowest amount of solvents and that with SRF takes up the highest. The samples loaded with HAF take an intermediate position. For a given void, fillers with lower particle size make a more compatible filling than those with higher particle size. The reinforcement of EVA by ISAF black, having the lowest particle size and the highest bound rubber content among the fillers used, causes reduced polymer chain mobility and free volume in the matrix. The SRF black filled composite shows a higher level of solvent uptake because of their high particle size and lower bound rubber content. The reinforcement by HAF lies in between these two. Figure 6 shows a pictorial representation of reinforcement of different types of fillers in EVA matrix. Another reason for the higher reinforcement of ISAF black might be the large number of oxidative groups in their surfaces such as quinone (> =O), phenol (> –OH), carboxylic acid (> –COOH) and lactone (> –COO–) [29] which result in a higher polarity.

Figure 7 shows the mol% benzene uptake by SRF filled samples at different filler loadings. Solvent

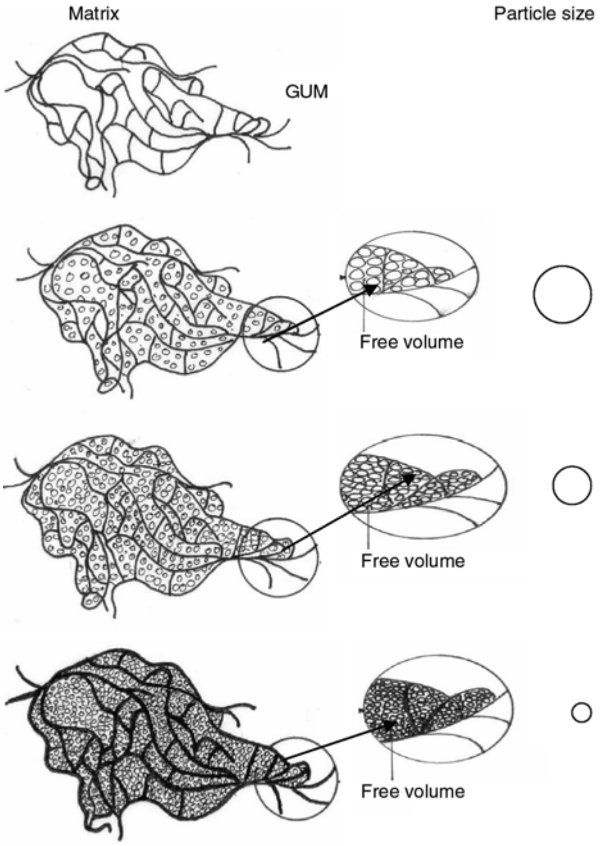

Figure 6. Pictorial representation of reinforcement of EVA with fillers of different particle size

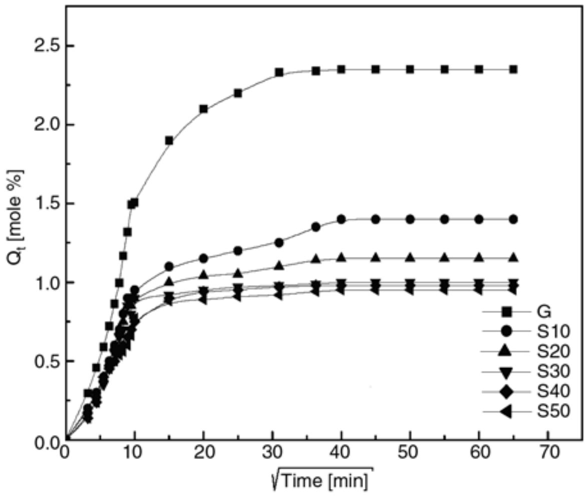

Figure 7. Mol% benzene uptake by EVA and EVA/SRF composite at different filler loading

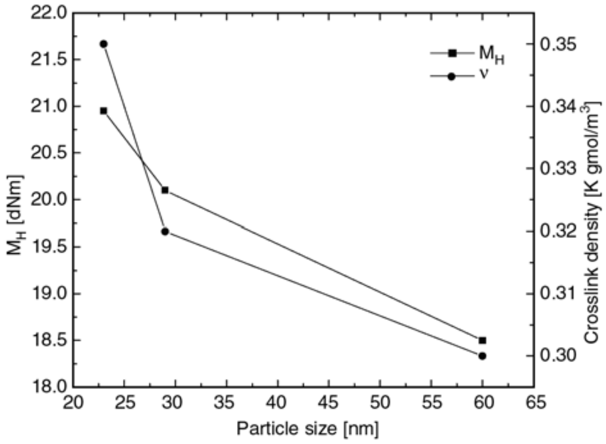

Figure 8. Crosslink density (ν) and maximum torque (M_H) of EVA/black composites as a function of particle size of filler

uptake has been found to be reduced further with increased filler content. This is due to the decreased free volume and polymer chain mobility in the composite with increased filler concentration.

3.3.2. Crosslink density

The crosslink density (ν) of the present systems has been estimated by using the Equation (3) [30]:

$$\nu = \frac{1}{2M_c} \qquad (3)$$

where M_c is the molar mass between crosslinks in the composites, given by the Equation (4) [31]:

$$M_c = \frac{-\rho_p V_s V_{rf}^{1/3}}{[\ln(1-V_{rf}) + V_{rf} + \chi V_{rf}^2]} \qquad (4)$$

where V_s is the molar volume of the solvent used, ρ_p is the density of the polymer and χ is the polymer-solvent interaction parameter. V_{rf}, the volume fraction of polymer in the solvent swollen filled composite sample, is given by the Equation (5) [32]:

$$V_{rf} = \frac{(d - fw)\rho_p^{-1}}{(d - fw)\rho_p^{-1} + A_s\rho_s^{-1}} \qquad (5)$$

where d is the deswollen weight of the sample, f is the volume fraction of filler in the dry composite sample, w the initial weight of the composite sample, ρ_s is the density of the solvent and A_s, the weight of solvent in the swollen sample.

Figure 8 shows the ν and M_H of EVA/carbon black composites as a function of the particle size of the filler used. The solvent used was benzene. Both ν and M_H of the composite have been found to be increasing with decreased particle size of the fillers.

3.3.3. Diffusion coefficient

Diffusion coefficient is a kinetic parameter related to the polymer segmental mobility, penetrant nature and to the different crosslinks present in a polymer matrix. The diffusion coefficient of a polymeric material immersed in a solvent can be calculated using the Equation (6) [33]:

$$\frac{Q_t}{Q_\infty} = 1 - \frac{8}{\pi^2}\sum_{m=0}^{m=\infty}\left(\frac{1}{(2m+1)^2}\right)e^{-(2m+1)^2\pi^2\frac{D\cdot t}{h^2}} \qquad (6)$$

where Q_t and Q_∞ are the mol% uptake at time t and at equilibrium respectively and m is an integer. D is the diffusion coefficient and h is the initial thickness of the sample. The above Equation (7) can be solved for short time limiting as:

$$\frac{Q_t}{Q_\infty} = 4\left[\frac{D\cdot t}{\pi h}\right]^{1/2} \qquad (7)$$

A plot of Q_t versus $\sqrt{t}$ is linear at short times. By rearranging Equation (7), the overall diffusion

Table 5. Values of diffusion coefficient at 28°C

Sample	$D\cdot10^8$ [m²/s]		
	Benzene	Toluene	Xylene
G	1.50	1.40	1.28
S10	1.12	1.01	0.95
H10	0.94	0.88	0.81
I10	0.93	0.83	0.75

coefficient can be calculated using the Equation (8) [34]:

$$D = 4\left[\frac{h\cdot\theta_D}{4Q_\infty}\right]^2 \qquad (8)$$

where θ_D is the slope of the initial portion of the plots of Q_t versus $\sqrt{t}$. A correction for swelling is made by incorporating V_{rf}, thus giving intrinsic diffusion coefficient D^* as Equation (9) [35]:

$$D^* = \frac{D}{V_{rf}} \qquad (9)$$

The values of D^* at 28°C for 10 phr filler loaded EVA composites are given Table 5. It can be seen from the table that for a given solvent, the diffusion coefficient values are in the order: SRF > HAF > ISAF filled composites. The diffusion coefficient for gum sample is higher than that of the composites.

3.3.4. Mode of transport

The mechanism of transport can be computed from the swelling data using the Equation (10) [36]:

$$\frac{Q_t}{Q_\infty} = k\cdot t^n \qquad (10)$$

where k indicates the interaction between the penetrant and the polymer and n represents the mode of transport. Taking log on both the sides, Equation (10) becomes Equation (11):

$$\log\frac{Q_t}{Q_\infty} = \log k + n\log t \qquad (11)$$

The value of n suggests the mode of transport. For the normal Fickian mode of transport, where the rate of polymer chain relaxation is higher compared to the diffusion rate of the penetrant, the value of n is 0.5. When $n = 1$, the transport approaches non-Fickian behaviour, where chain relaxation is slower than the liquid diffusion. If the value of n is in between 0.5 and 1, the mode of transport is classified as anomalous. k is a constant depending on the interaction between the rubber and solvent. The estimated values of n and k for different systems are given in Table 6. It can be seen that the diffusion process in the present case deviates from the regular Fickian trend, observed with conventional rubbers, and can be classified as anomalous. Deviations from the Fickian sorption are associated with the time taken by rubber segments to respond to swelling stress and rearrange themselves to accommodate the solvent molecules. The reinforcement with the filler particle imparts a high degree of restriction to the rearrangement of rubber chains. Thus the observed anomalous diffusion involves the counteraction between the ability of the rubber segments to rearrange in the presence of solvents and the restriction imparted to this by the reinforced filler particles. The k values decrease with increase in the molecular size of the penetrants from benzene to xylene, indicating decreased polymer-solvent interaction.

3.3.5. Sorption-desorption-resorption (S-D-RS) experiments

A S-D-RS experiment was carried out to study the physical changes in the matrix with solvent transport [37]. The solvent saturated samples were desorbed completely, and then allowed to sorb the solvent again. The S-D-RS curves of sample S10 in

Table 6. Values of n and k

Sample	n			$k\cdot10^2$ [min⁻¹]		
	Benzene	Toluene	Xylene	Benzene	Toluene	Xylene
G	0.64	0.68	0.69	2.14	2.10	1.98
S10	0.71	0.74	0.75	2.21	1.90	1.89
H10	0.72	0.75	0.76	1.90	1.89	1.78
I10	0.74	0.76	0.77	2.11	1.99	1.89

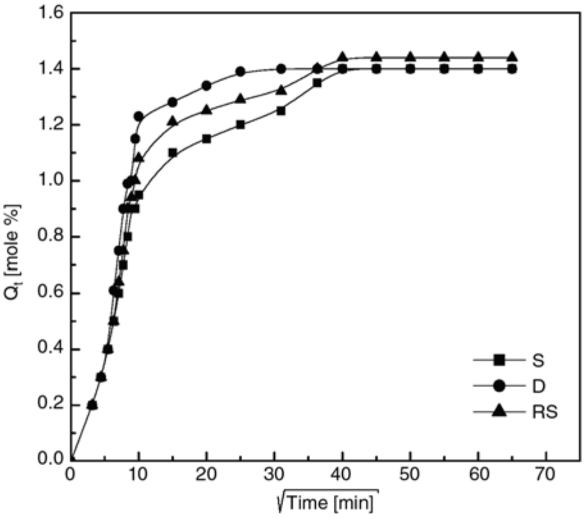

Figure 9. S-D-RS curves of S10 in benzene

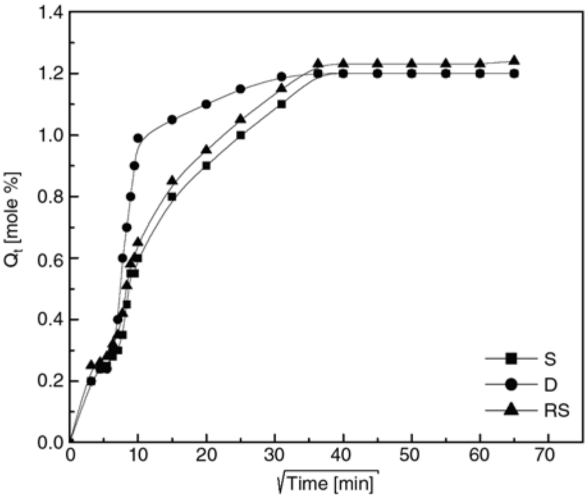

Figure 10. S-D-RS curves of H10 in toluene

benzene and H10 in toluene are given in Figures 9 and 10 respectively. The mol% equilibrium solvent uptake for the resorption curve is found to be slightly higher than that of sorption curve. After a sorption-desorption cycle, the available free volume within the polymer matrix and the polymer segmental mobility increases and hence, the subsequent resorption process is different from that of the sorption process. Figures 9 and 10 also reveal that the rate of desorption is higher than that of sorption. In the sorption process, the solvent molecules have to penetrate into the tightly packed network and hence the rate of penetration process is low. In the desorption process, the escape of solvent molecule from the relaxed polymer chain takes place more easily.

4. Conclusions

The cure characteristics and solvent transport behaviour of black filled EVA have been studied. The M_H of the composites exhibited a decreasing trend with increasing particle size and an increasing behaviour with content of filler. The solvent uptake trend of EVA has been observed to be reduced by carbon black incorporation. Among the filled samples the ISAF filled sample showed the lowest solvent uptake followed by HAF and then SRF filled samples. The mode o transport in all the cases has been observed to be anomalous. The S-D-RS experiment carried out showed that the composites accommodate more solvent after a sorption-desorption cycle.

References

[1] Landois-Garza J., Hotchkiss J. H.: Food and packaging interactions. American Chemical Society Symposium Series, Washington (1988).
[2] Seymour R. B.: Engineering polymer source book. McGraw-Hill Publishing, New York (1990).
[3] Huang R. Y. M.: Pervaporation membrane separation processes. Elsevier, New York (1991).
[4] Kulkarni P. V., Rajur S. B., Antich P., Aminabhavi T. M., Aralaguppi M. I.: Transport studies on macromolecules used as drug carriers. Journal of Macromolecular Science, Reviews in Macromolecular Chemistry and Physics, **30,** 441–470 (1990).
[5] Peppas N. A.: Hydrogels in medicine and pharmacy. CRC Press, Boca Raton (1987).
[6] Guth E.: Theory of filler reinforcement. Journal of Applied Physics, **16**, 20–25 (1945).
[7] Porter M.: Structural characterization of filled vulcanisates, 1. Determination of the concentration of chemical crosslinks in natural rubber vulcanisates containing high abration furnace black. Rubber Chemistry and Technology, **40**, 866–882 (1967).
[8] De Candia F., Gargani L., Renzulli A.: Transport properties of filled elastomeric networks. Journal of Applied Polymer Science, **41**, 955–964 (1990).
[9] Kwei T. K., Kunins C. A.: Polymer-filler interaction: Vapour sorption studies. Journal of Applied Polymer Science, **8**, 1483–1490 (1964).
[10] Anfimova E. A., Lykin A. S., Anfimov B. N.: Equilibrium swelling of filled vulcanizate of natural rubber (in Russian). Polymer Science U.S.S.R., **24**, 455–461 (1982).
[11] Rutherford S. W., Kurtz R. E., Smith M. G., Honnell K. G., Coons J. E.: Measurement and correlation of sorption and transport properties of ethylene-propylene-diene monomer (EPDM) elastomers. Journal of Membrane Science, **263**, 57–65 (2005).

[12] Choi S-S.: Difference in bound rubber formation of silica and carbon black with styrene butadiene rubber. Polymers for Advanced Technologies, **13**, 466–474 (2002).

[13] Leblanc J. L.: Rubber-filler interactions and rheological properties in filled compounds. Progress in Polymer Science, **27**, 627–687 (2002).

[14] Ismail H., Poh B. T., Tan K. S., Moorthy M.: Effect of filler loading on cure time and swelling behaviour of SMRL/ENR and SMRL/SBR blends. Polymer International, **52**, 685–691 (2003).

[15] Sujith A., Unnikrishnan G., Radhakrishnan C. K., Padmini M.: Interaction of silica and carbon black fillers with natural rubber/ethylene-co-vinyl acetate matrix by swelling studies. Polymer Composites, **28**, 705–712 (2007).

[16] Unnikrishnan G., Thomas S.: Molecular transport of benzene and methyl substituted benzenes into filled natural rubbers. Journal of Applied Polymer Science, **60**, 963–970 (1996).

[17] Unnikrishanan G., Thomas S., Varghese S.: Sorption and diffusion of aromatic hydrocarbons through filled natural rubbers. Polymer, **37**, 2687–2693 (1996).

[18] Dasan K. P., Haseena A. P., Unnikrishnan G., Alex R., Purushothaman E.: Transport characteristics of filled poly(ethylene-co-vinyl acetate) membranes. Polymers and Polymer Composites, **12**, 599–617 (2004).

[19] Sujith A., Unnikrishnan G.: Barrier properties of natural rubber/ethylene vinyl acetate/carbon black composites. Journal of Materials Science, **40**, 4625–4640 (2005).

[20] Leblanc J. L., Hardy P.: Evolution of bound rubber during the storage of uncured compounds. Kautschuk und Gummi, Kunststoffe, **44**, 1119–1124 (1991).

[21] George S. C., Thomas S.: Carbon black filled SBR composites: The effect of rubber-filler interaction on transport. Journal of Macromolecular Science: Physics, **39**, 175–195 (2000).

[22] Karasek L., Sumita M.: Characterization of dispersion state of filler and filler polymer interactions in rubber-carbon black composites. Journal of Materials Science, **31**, 281–289 (1996).

[23] Wee Y-P., Wang Y-Q., Zhang H-F., Wang Y-Z., Yee D-S., Zhang A-Q., Yang J.: Rubber pristine clay nanocomposites prepared by co-coagulating rubber latex and clay aqueous suspensions. Composites Science and Technology, **65**, 1195–1202 (2005).

[24] Sandrine B-C., Christian C.: Interaction of active carbon black with low- and high- molecular weight polyethylene glycol and polyethylene oxide. Journal of Applied Polymer Science, **100**, 3490–3497 (2006).

[25] Moon Y. D., Lee Y. M.: Dynamics of solvent diffusion in an aromatic polyimide. Journal of Applied Polymer Science, **51**, 945–954 (1994).

[26] Elwy A., Badawy M. M., Nasr G. M.: Electrical properties and penetration rate of solvent into irradiated LDPE/SBR conductive blends. Polymer Degradation and Stability, **53**, 289–294 (1996).

[27] Haseena A. P., Priya Dasan K., Namitha R., Unnikrishnan G., Thomas S.: Investigation on interfacial adhesion of short sisal/coir hybrid fibre reinforced natural rubber composites by restricted equilibrium swelling technique. Composite Interfaces, **11**, 489–513 (2004).

[28] Billmeyer F. W.: Text book of polymer science. Wiley Interscience, Singapore (1994).

[29] Bicerano J.: Prediction of polymer properties. Marcel Dekker, New York (1993).

[30] Mark J. E., Erman B.: Rubberlike elasticity- A molecular primer. Wiley Inter Science, New York (1988).

[31] Flory P. J.: Principles of polymer chemistry. Cornell University Press, Ithaca (1953).

[32] Ellis B., Welding G. N.: Techniques in polymer science. Society of the Chemical Industry, London (1964).

[33] Crank J.: The mathematics of diffusion. Oxford University Press, Oxford (1975).

[34] Lucht L. M., Peppas N. A.: Transport of penetrants in the macromolecular structure of coals, V. Anomalous transport in pretreated coal particles. Journal of Applied Polymer Science, **33**, 1557–1566 (1987).

[35] Varghese H., Bhagwan S. S., Thomas S.: Transport properties of crosslinked acrylonitrile butadiene rubber/poly(ethylene-co-vinyl acetate) blends. Journal of Polymer Science, Part B: Polymer Physics, **37**, 1815–1831 (1999).

[36] Aminabhavi T. M., Phayde H. T. S.: Molecular transport of alkanes through thermoplastic miscible blends of ethylene-propylene random copolymer and isotactic polypropylene. Journal of Applied Polymer Science, **55**, 1335–1352 (1995).

[37] Nair S. V., Sreekala M. S., Unnikrishnan G., Johnson T., Thomas S., Groeninckx G.: The role of crosslinking and crystallization on the transport characteristics of ethylene-propylene rubber membranes. Journal of Membrane Science, **177**, 1–7 (2000).